The Effect of Boundary Layer Blowing in the Corner Region of a Linear Compressor Cascade Wind Tunnel

by

Ralph William James, Jr.

Thesis submitted to the Faculty of the

Virginia Polytechnic Institute and State University

in partial fulfillment of the requirements for the degree of

Master of Science

in

Mechanical Engineering

APPROVED:

W. F. O'Brien, Chairman

C. L. Dancey

J. Moore

June, 1995

Blacksburg, Virginia

.2

The Effect of Boundary Layer Blowing in the Corner Region of a Linear Compressor Cascade Wind Tunnel

by

Ralph William James, Jr.

W. F. O'Brien, Chairman

Mechanical Engineering

(ABSTRACT)

A fundamental investigation of the flow in the endwall corner region of a linear compressor cascade wind tunnel and the effect of boundary layer blowing in this region was conducted using blade surface pressure tap measurements and five - hole prism probe measurements taken downstream of the cascade. The results are presented as a series of velocity vector plots, loss contour plots, and pitchwise mass - averaged loss coefficient plots. The angle of attack test range was from 5 to 29 degrees.

For the corner region boundary layer blowing investigations, two slots were machined into the ends of a set of cascade blades, and an external air source was used as the blade slot jet air source. Tests were done for 19, 21, and 23 degrees angle of attack. The main effect of corner boundary layer blowing was a significant reduction in total pressure losses in the region along the blade span between the exterior portion of the corner boundary layer flow and the blade profile boundary layer flow.

Acknowledgements

The author would like to thank his advisory committee members consisting of W. F. O' Brien, chairman, C. L. Dancey, and J. Moore for their guidance in completing this research effort.

Special thanks are extended to Dr. O' Brien for his many helpful comments and suggestions throughout the course of this investigation.

Additional thanks are in order for all past and present turbolab members who have provided advice and assistance to the author during his graduate school stay.

Finally, the author would like to thank his parents for providing their support and encouragement throughout his graduate school studies. Their patience and understanding will always be appreciated.

Table of Contents

List of Figures

List of Tables

List of Symbols

A_j	Blade slot jet air exit area
c	Blade chord length
Cp_b	Blade surface pressure coefficient
Cp_{pitch}	Probe pitch angle calibration coefficient
Cp_{static}	Probe static pressure calibration coefficient
Cp_{total}	Probe total pressure calibration coefficient
Cp_{yaw}	Probe yaw angle calibration coefficient
$P_{1,2,3,4,5}$	Five - hole prism probe measured pressures
Pamb	Ambient pressure
Ps_1	Upstream static pressure
Psb	Blade surface pressure
Pt_1	Upstream total pressure
Pt_2	Downstream total pressure
Qpsg	Blade passage volumetric flow rate based on the blade slot length
Qsa	Actual rotameter volumetric flow rate

Qsb	Actual blade slot volumetric flow rate, $\frac{Qsa}{2}$
Qsr	Rotameter volumetric flow rate reading
Re_c	Reynolds number based on blade chord length, $\frac{\rho \cdot V_1 \cdot c}{\mu}$
Re_p	Reynolds number based on probe head diameter, $\frac{\rho \cdot V_1 \cdot D_p}{\mu}$
s	Pitch
Tamb	Ambient temperature
V_1	Cascade inlet velocity
V_2	Cascade outlet velocity
V_{2x}	Axial component of the cascade outlet velocity
Vj	Blade slot jet air velocity
i	Incidence angle
α	Five - hole probe pitch angle
β	Five - hole probe yaw angle
ξ	Stagger angle
ω	Total pressure loss coefficient
α^*	Angle of attack
θ^*	Blade camber angle
α_1	Air inlet angle
α_2	Air outlet angle
ϖ_2	Overall mass - averaged loss coefficient
$\varpi_2(z)$	Pitchwise mass - averaged loss coefficient
ρ_a	Air density at cascade flow conditions

ρ_j Blade slot jet air density

1.0 Introduction and Literature Review

For a linear compressor cascade wind tunnel, the mixing of the sidewall and blade profile boundary layers results in large areas of three - dimensional flow in the region bounded by the blade suction surface and the cascade sidewall, known as the corner region. The fluid flow in this region results in large total pressure losses which make up a significant part of the overall cascade aerodynamic losses. Boundary layer control methods involving suction and blowing techniques have been successfully applied to airfoils for the purposes of lift augmentation, delaying boundary layer separation at increased angles of attack, and drag reduction through maintaining laminar flow over the surface of an airfoil[1]. The current study was undertaken in order to investigate a cascade corner flow region and the effects of localized boundary layer blowing on its aerodynamic performance.

Figure 1 shows a general view of the present cascade test section, and Fig. 2 illustrates the cascade coordinate system. The cascade blade geometry

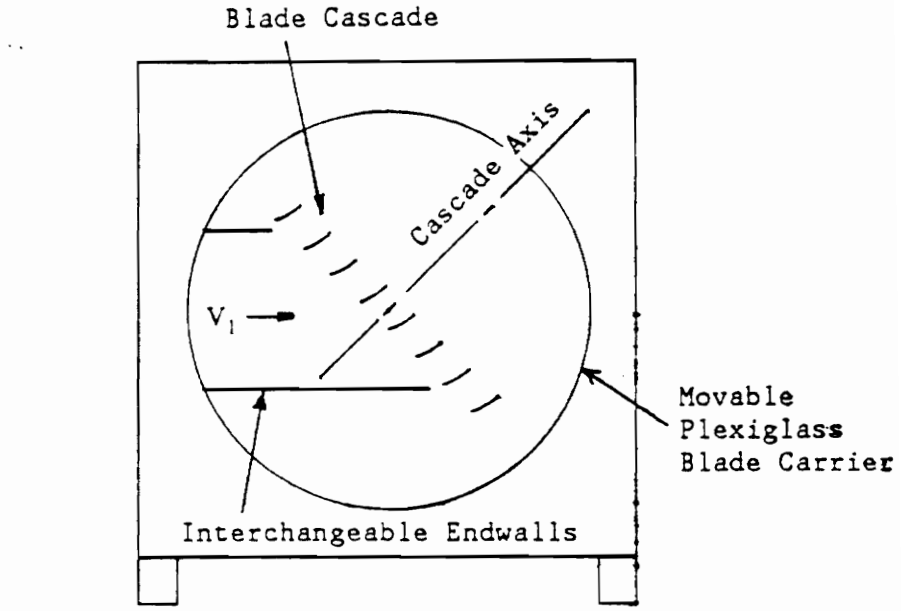

SIDE VIEW

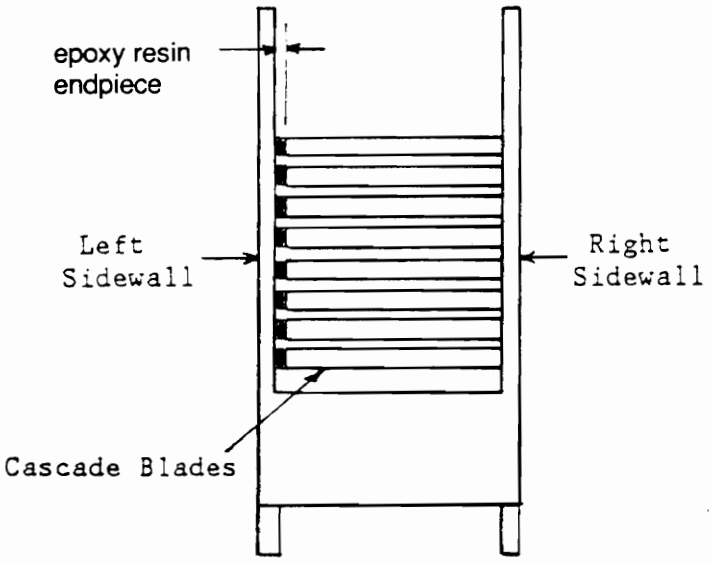

FRONT VIEW

Figure 1. Principal Components of Cascade Test Section[ref. 8]

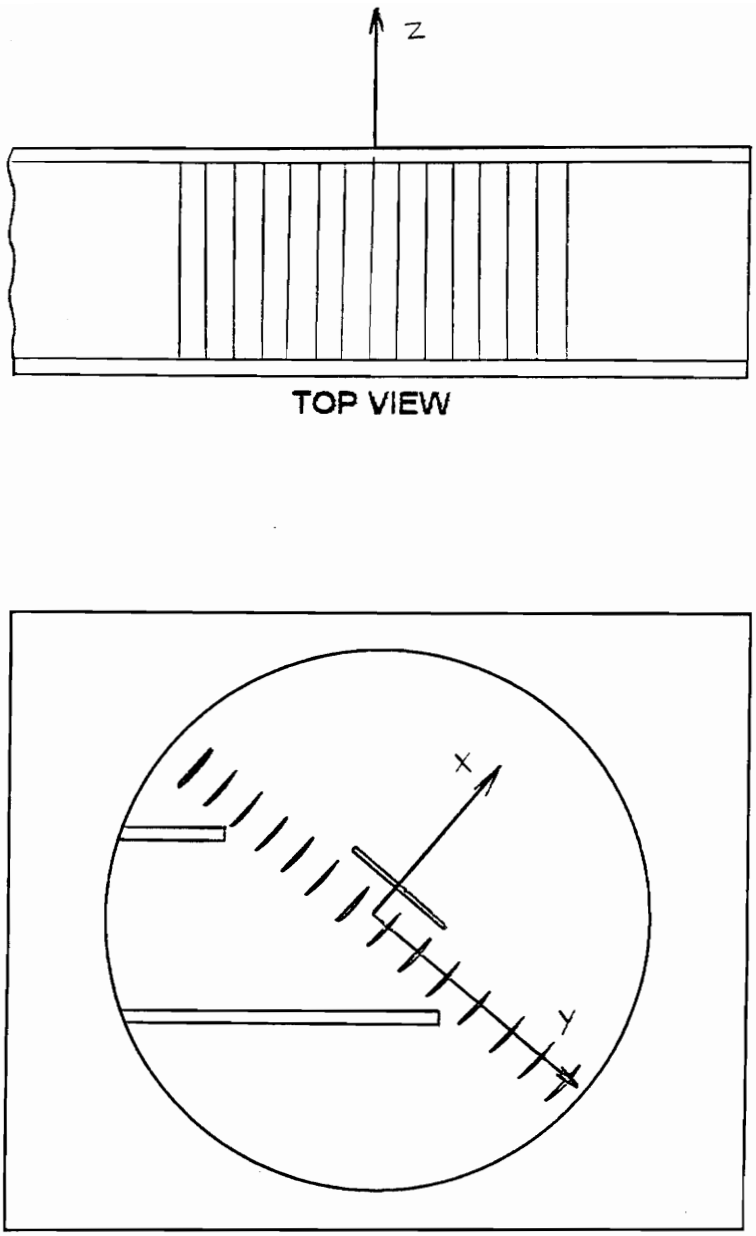

Figure 2. Cascade Coordinate System

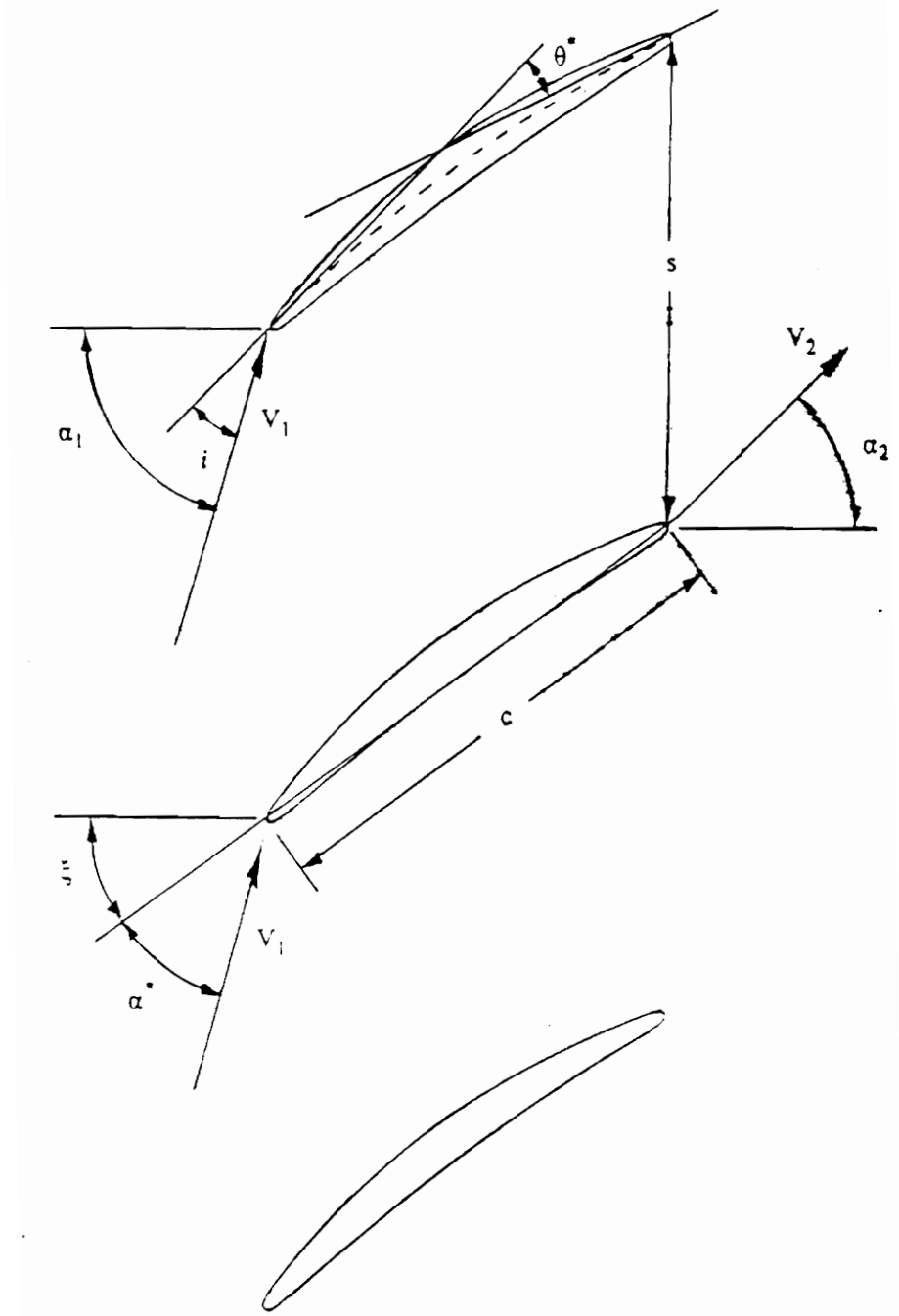

Figure 3. Cascade Geometry and Flow Angle Notation [ref. 8]

and flow angles appear in Fig.3. To encourage periodicity and allow high angles of attack, the cascade uses a number of high aspect ratio blades. For the present investigation, no attempt was made to control the periodicity of the test section through sidewall suction or other means. The initial experimental investigation for this study involved corner region pressure tap readings of the blade suction and pressure surfaces. This was followed by downstream, five - hole pitot probe measurements from which total pressure loss contours and velocity vector plots showing secondary flow effects were obtained. Using these initial results, a set of cascade blades were designed in order to manipulate the corner region boundary layer. At this point, past research in the area of interest will be discussed.

Maestrello [2] did an investigation into active transition fixing of the boundary layer of an airfoil surface flow through the use of sound and heat. He demonstrated that heating of the airfoil surface resulted in boundary layer transition from laminar to turbulent, mainly under the influence of a favorable pressure gradient. Through the use of feedback sound control, a reduction in velocity perturbations at near - normal incidence of sound waves to fluid flow resulted. The effects were seen mainly in the transitional regions of fluid flow along the airfoil surface, demonstrating the relationship between blade surface velocity perturbations and sound waves.

Using real - time velocity fluctuation measurements from hot wire and hot film probes, Gallus, et al. [3] did an investigation into the profile and sidewall boundary layers in the region of an axial - flow compressor stage bounded by the stator blade suction surface and the hub casing. Their focus was to learn more about the flow separation and stall characteristics of a compressor stage in order to increase the maximum diffusion allowable in a blade row. They were able to show that the boundary layers were permanently separated between the first relative maxima of turbulent energy recorded and the stator blade suction surface.

Mikolajczak, et al. [4] did a study of the performance of slotted blades in comparison to solid blades in a compressor cascade wind tunnel. They were attempting to increase the operable range of blade incidence angle, in order to achieve higher blade loading capabilities, by using slotted blades. Their first step was an investigation into the fluid flow regime of the compressor cascade using incompressible flow theory. Experimental investigations utilizing slotted airfoils and stator blades followed. Through their experiments, they were able to show that slotted blades offered a somewhat increased range of operable incidence angle. However, an increase of the cascade minimum loss value, in comparison to that of a cascade with solid blades, occurred. They also indicated that the slot effectiveness was highly dependent on its chordwise location. The data presented was representative of two - dimensional flow over a blade with an

infinite slot. The jet air flow through the slot was produced by the pressure difference between the two sides of the blade. Sidewall effects were not taken into account during their investigations.

Erwin, et al. [5] were able to achieve nearly two - dimensional flow conditions in a linear compressor cascade by using porous sidewalls. They were attempting to demonstrate the effects of various cascade testing conditions, involving different values for Reynolds number and aspect ratio, on the performance of airfoils in a compressor cascade. The main focus of their work was in varying the test airfoil aspect ratio, and employing either porous or solid cascade sidewalls during the individual test runs.

Dirlik, et al. [6] applied boundary layer blowing and suction techniques to an airfoil to investigate whether a performance improvement would result. The main focus of their work was to try to delay the onset of blade profile separation and stall outside of the airfoil corner region. From their results, control of the boundary layer through suction was found to be of little value, but they were able to show that boundary layer blowing caused a delay in airfoil profile stall as the angle of attack was increased. This resulted in larger lift coefficients at higher angles of attack than was obtainable when profile boundary layer blowing was not applied to the airfoil suction surface.

Tang, et al. [7] carried out an investigation into the corner vortex structure of a linear compressor cascade. From their work, a process of three -

dimensional flow separation in the corner region was observed in which a corner vortex was generated on the suction surface of the blades. From their results, it was found that the secondary flow in the sidewall area played an important role in corner boundary layer separation. Their idea was that the corner flow consisted of a corner vortex and a series of secondary vortices, with the passage vortex being a different structure from the corner vortex. They believed that the complex flow pattern in the corner region was a result of the interactions between this set of vortices and the main flow. It was suggested that the corner vortex transferred low momentum fluid in the spanwise direction along the blade suction surface, and that the mixing of high and low momentum fluid expanded the region affected by the corner stall. Additionally, they believed that the corner vortex received its initial vorticity from an incoming horseshoe vortex, and deteriorated at high blade incidence angles. This conclusion was arrived at from their observation of reversed flow migrating into the corner stall region.

From Russ [8], an idea of the flow pattern over cascade blades at moderate angles of attack was gained through his flow visualization work with a cascade having a solidity of one. From his results, a general view of the physical nature of the corner flow could be seen for different stagger angles and angle of attack combinations. He determined that the blade suction surface flow was largely two - dimensional before and after full blade stall. The corner flow

structure was observed prior to full blade stall, as well as for fully - stalled conditions, at all angles of attack.

The explanation of Gostelow[9] for secondary flow was that the static pressure distribution outside the sidewall region tends to dominate up to the wall. The same degree of loading present in the midspan region of the cascade is also present in the corner region, with a much reduced incoming velocity, u. The static pressure gradient normal to the streamline, given by the equation $dp/dn = \rho u^2/r$, must be the same in the corner region as it is at midspan. Since the corner region velocity is less than the velocity at midspan, the flow radius of curvature, r, must also be less. The result is a velocity component that is perpendicular to the free stream flow in the corner region. This causes the development of a passage vortex which results in overturning at the sidewall and underturning some distance from the sidewall. Gostelow suggested that the initiation of stall in an axial flow compressor began in the corner as a result of this effect.

Horlock, et al. [10] did an investigation of the sidewall boundary layer of a linear compressor cascade. They observed the presence of conventional secondary flow effects, such as overturning at the sidewall and underturning at midspan. However, simple secondary flow analysis methods proved not to be accurate in the corner region due to the interaction of the sidewall and blade suction side boundary layers. The influences of the wall alone on the sidewall losses were examined. This led to the suggestion that sidewall losses were a

primary function of separation of the wall boundary layer in the corner formed by the cascade sidewall and blade suction surface. In addition, from their results they demonstrated that an optimum tip clearance gap existed by which the sidewall losses could be reduced to a minimum value.

2.0 Experimental Facilities and Methods

The initial experimental program consisted of obtaining blade pressure tap measurements in the corner and midspan regions of the cascade. This was followed by a series of downstream five - hole pitot probe measurements, taken in the non - nulling mode, in order to examine the downstream total pressure loss coefficients and velocity vector patterns. After an examination of the initial experimental results, a set of slotted cascade blades were made. The slots were located at the ends of the blades in order to manipulate the corner boundary layer by blowing a jet of air over the blade suction surface. An external air source was utilized as the jet air source. With the slotted blades in the test section, additional downstream measurements were taken to observe the cascade aerodynamic performance under the influence of corner boundary layer blowing. The equipment and methods used to perform the experiments are described in the following sections.

2.1 Wind Tunnel and Compressor Cascade

The experimental work was conducted in the subsonic cascade wind tunnel of the Mechanical Engineering Department of the Virginia Polytechnic Institute and State University (VPI&SU). A schematic view of the facility can be seen in Fig. 4. A 15 - horsepower, Aerovent Model 630 BIA, centrifugal blower is used to force atmospheric air through the tunnel. The cascade test section velocity, along with the blade chord Reynolds number, can be controlled by manipulating a valve located on the inlet flow area of the blower housing. The flow initially passes through a diffuser and then is directed into a 1.22 m^2 settling section where straightening and smoothing of the flow is produced by an 8,000 cell 76.2 mm thick honeycomb section and a series of three screens. Following this, a section with a 16:1 contraction ratio accelerates the flow and prevents excessive boundary layer development from occurring at the entrance to the cascade test section. A horizontal duct with a span of 308 mm and a height of 305 mm connects the cascade test section to the rest of the tunnel. The blades are mounted between two large disks that allow the angle of attack to be varied. The stagger angle can also be changed by rotating each blade about its mounting axis. The solidity (c/s) of the cascade is 1.5, and the blades are set at a stagger angle of 25 degrees. The top portions of the horizontal inflow duct are interchangeable to accommodate various blade row angle of attack settings.

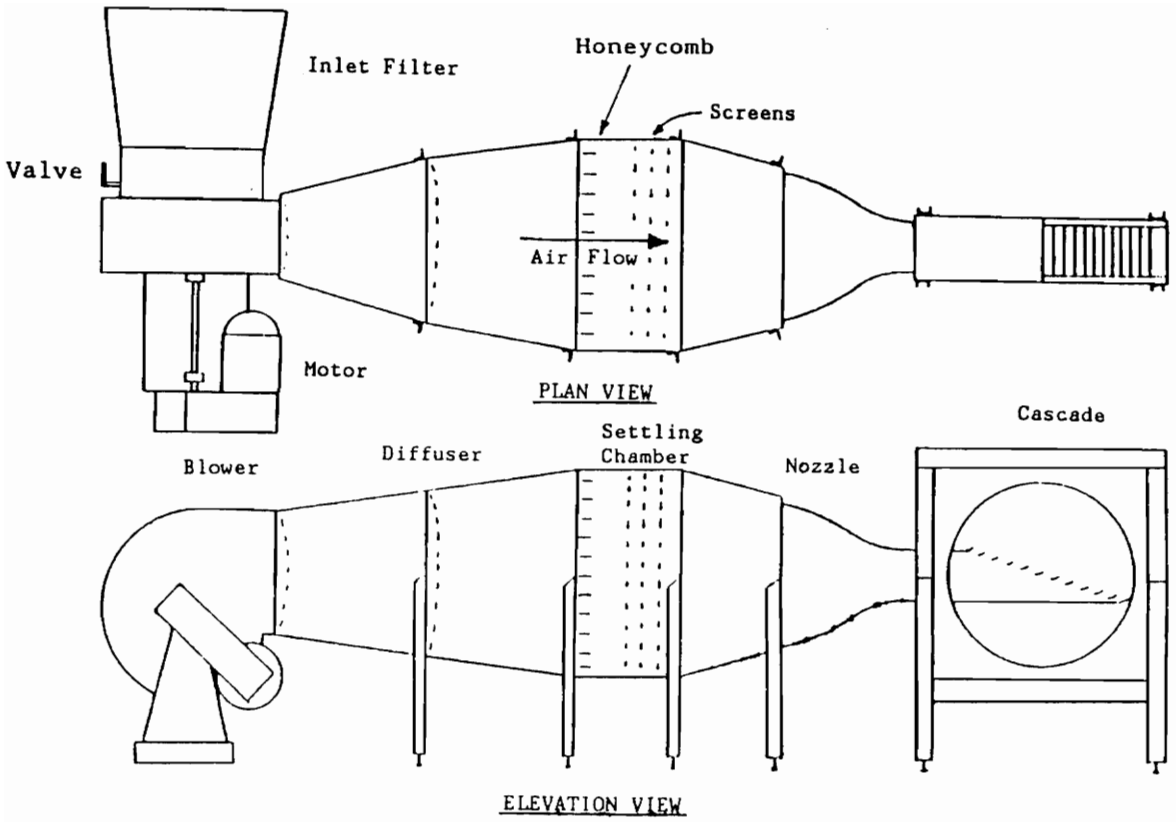

Figure 4. Cascade Wind Tunnel [ref. 8]

The maximum air inflow rate to the test section is 50 m/s. This corresponds to a blade chord Reynolds number of $2.08X10^5$ and a Mach number of 0.145.This allows incompressible flow to be assumed. An average inflow turbulence intensity level of 1.1 percent has been measured by Yocum[11] for the range of achievable tunnel speeds.

The cascade blades are made of aluminum and have no twist. The blade profile shape is shown in Fig. 5. The blades have a camber angle of 18 degrees, chord length of 65.53 mm, and height of 304.8 mm. The aspect ratio of the blades is 4.65. Since the blades are 3.2 mm shorter than the test section span, an epoxy resin endpiece is fitted into the resulting gap. A series of bolts and screws secure the blades in the test section.

For corner boundary layer blowing, slotted blades were used which directed a jet of air over the blade suction surface. The blades were placed in the center of the cascade test section. Each blade had two slots which had their exits on the blade suction surface. Each slot within the two blades was inclined at two different angles. A description of the slotted blades is shown in Fig. 6, and a detailed view of the slotted blade ends appears in Fig. 7. The blades were designed to be supplied with air from an external source in order to generate the jet of air through the slots. This was achieved through the use of two metal tubes which were embedded within the blades (Fig. 6). These tubes were then connected to the external jet air source through the nozzle / rotameter device

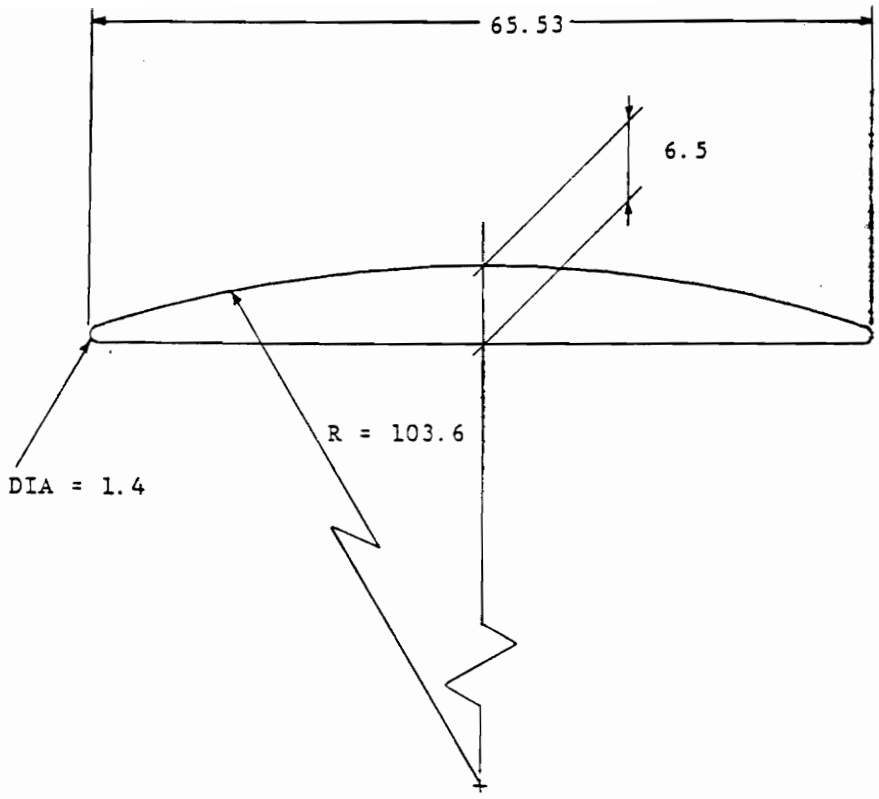

Figure 5. Blade Profile [ref. 8]

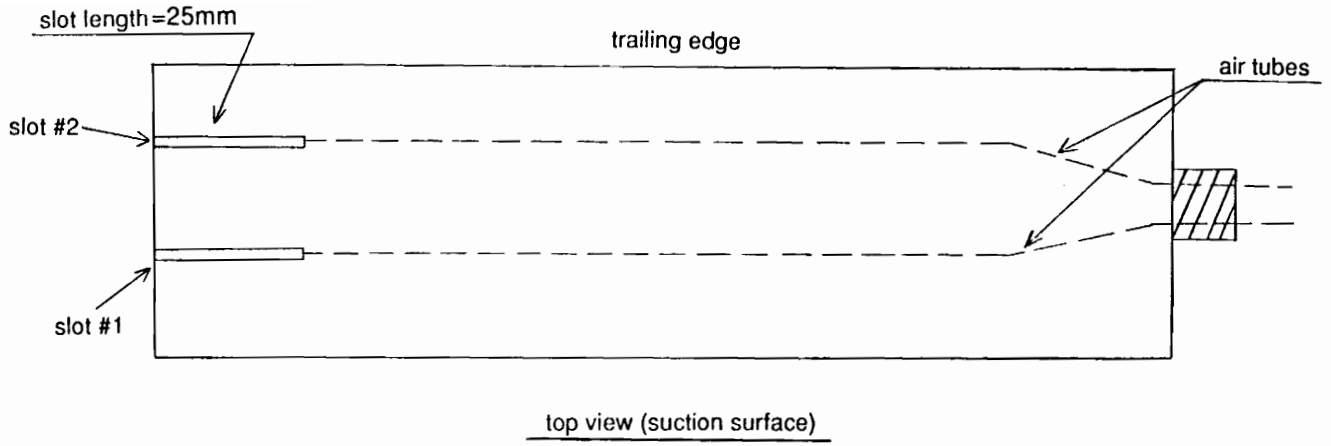

Figure 6. Slotted Cascade Blade

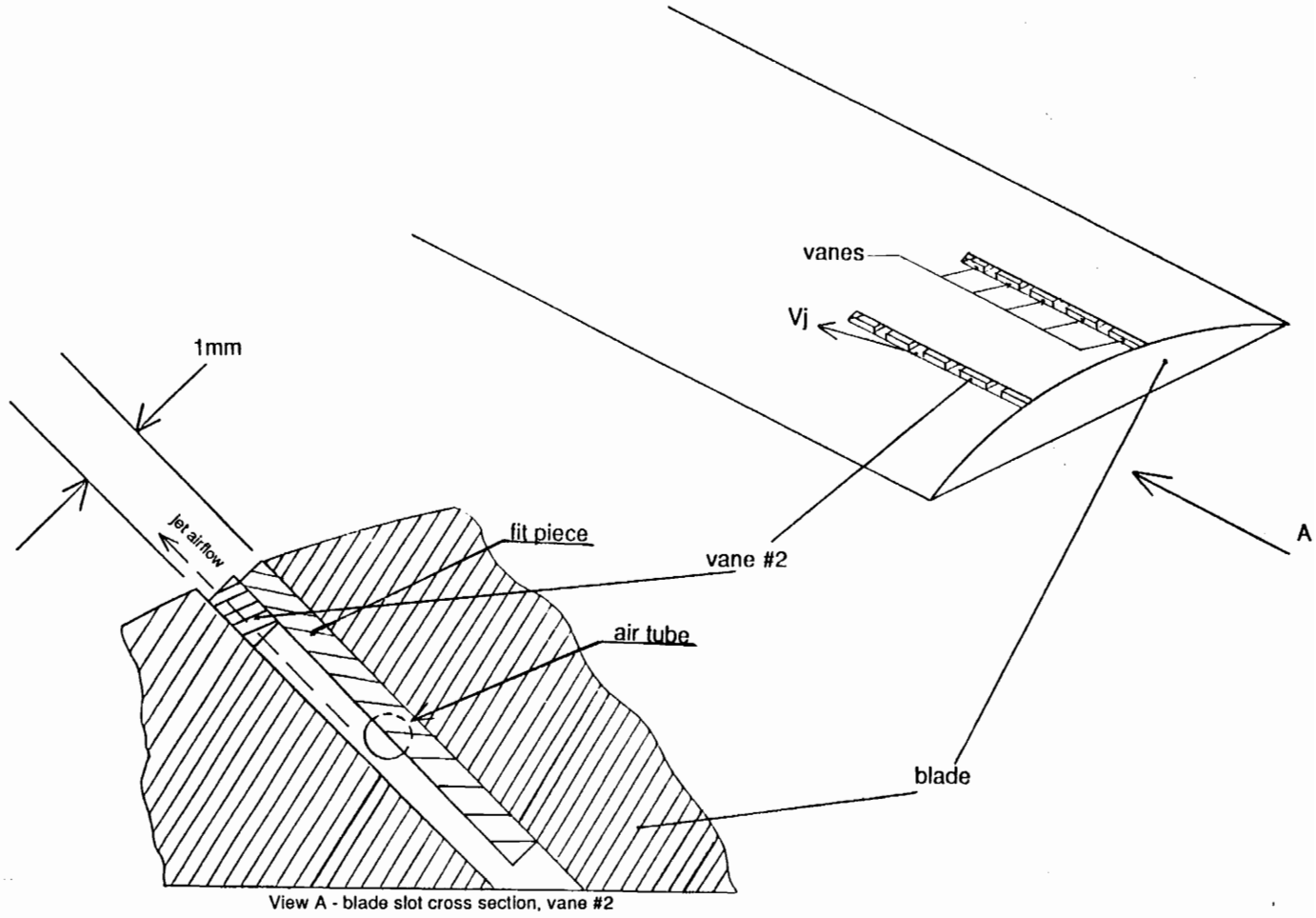

Figure 7. Detailed View of Cascade Blade Slotted End

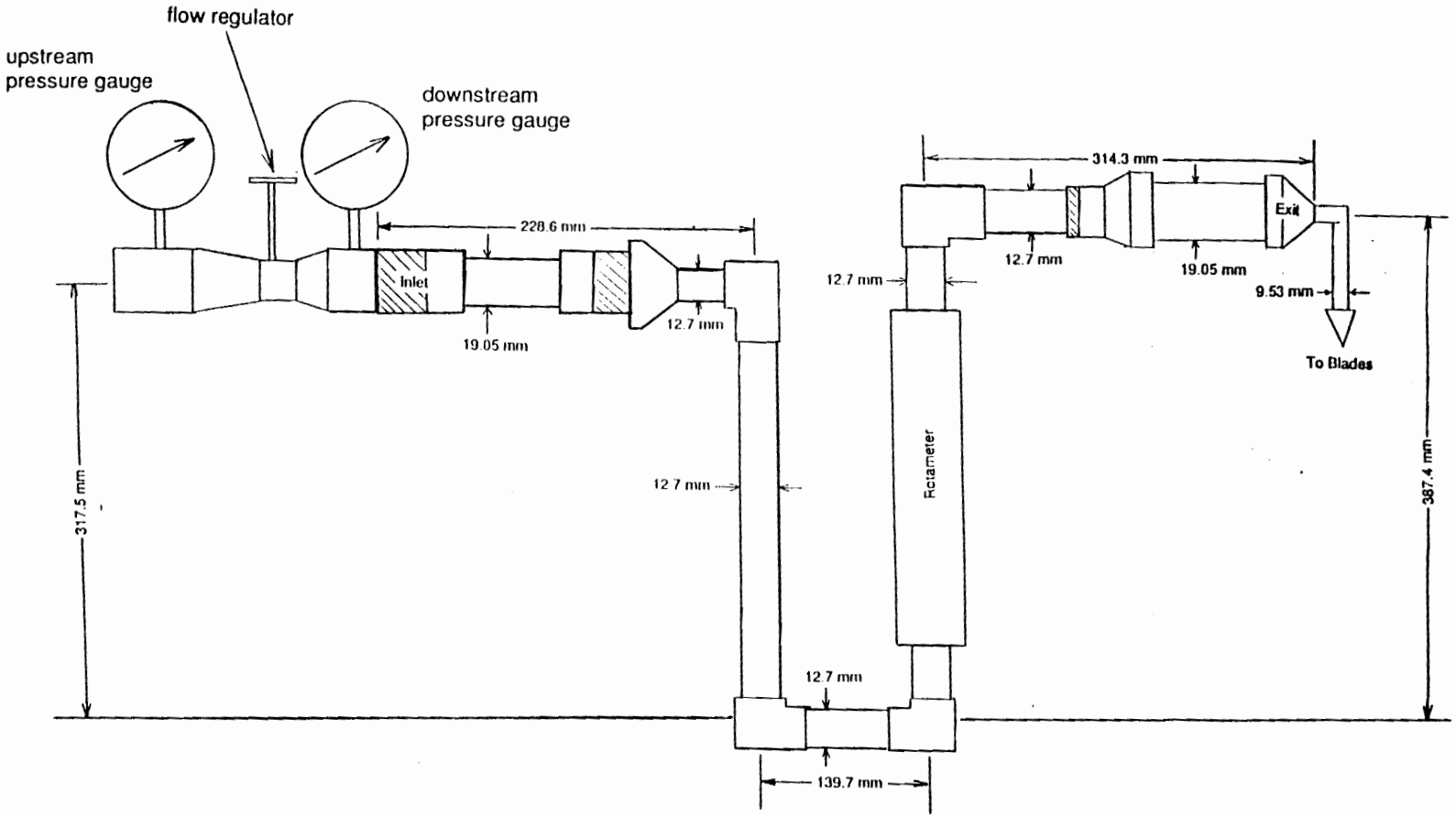

Figure 8. Nozzle / Rotameter Device

shown in Fig. 8. This device was used to regulate and measure the mass flow rate of air which was sent to the blade slots. The external air source was a line of air at a pressure of 80 psig.

The mass flow rate was obtained by using an Omega FL - 214 rotameter which could measure volumetric flow rates ranging from 1 to 36 Li/min, utilizing a glass ball float, or 1 to 64 Li/min, utilizing a stainless steel ball float. For the present investigation, the stainless steel ball float was used in the rotameter. The rotameter had a maximum working pressure of 300 psig and a readability of ± 5%. Since the probe was initially calibrated, by the manufacturer, at standard conditions (1 ATM and 70°F), a correlation equation was used to take into account the operating pressure and temperature in determining the actual rotameter volumetric flow rate. This equation appears as part of the blade slot jet air velocity calculation procedure, which is shown in Appendix A.

2.2 Instrumentation

A model DA -125 United Sensor five - hole prism probe was used to obtain downstream blade row exit velocities and total pressure loss values. The probe was calibrated for use in the non - nulling mode. An illustration of the probe is shown in Fig. 9. The distance from the prism probe head to the blade trailing edge was 5 mm. The resulting set of five measured pressures enabled the calculation of the magnitude and direction of the exit flow relative to the

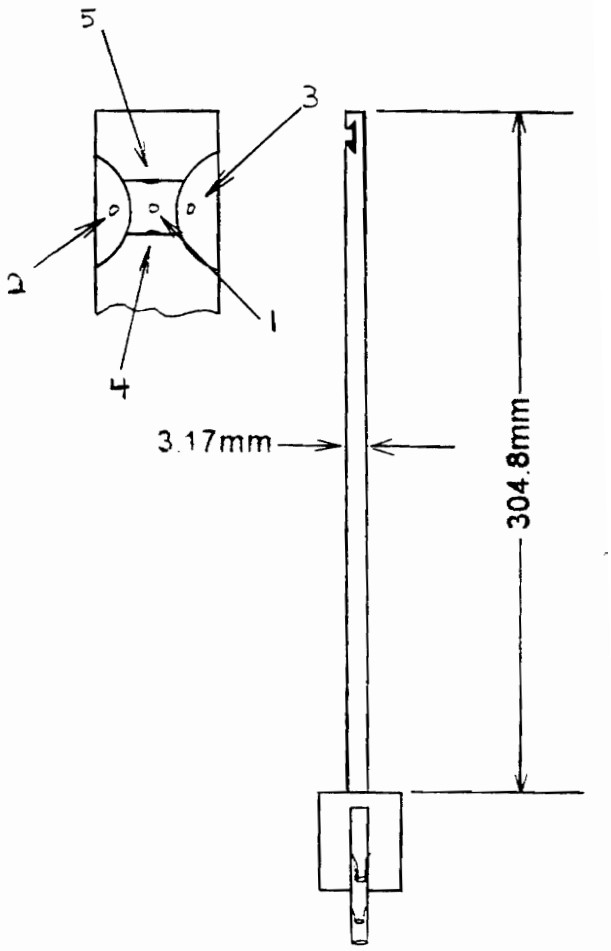

Figure 9. Five - Hole Prism Probe

prism probe head. From these measurements, total pressure loss contours and velocity vector plots were made to illustrate the cascade wake secondary flow characteristics. The calibration and data evaluation procedures for the probe appear in Appendix B.

The five - hole probe was mounted on a traversing mechanism which could move in both rectilinear and rotational directions with an accuracy of ± 0.8degrees and ± 0.03 mm, respectively. Foam weather - stripping material was placed in the probe traverse slot to prevent airflow leakage. The traverse mechanism was a model DI - 3R unit, manufactured by the L. C. Smith Company. It is a closed loop device and is controlled by an IBM - PC compatible computer.

For corner region static pressure measurements, a series of eleven pressure taps were arranged on both the pressure and suction surfaces of two cascade blades. The pressure taps were arranged in two rows, located at different spanwise positions, at the blade ends. Figure 10 shows the placement of the blade corner region pressure taps. Static pressure measurements were also taken at the midspan position of the blades utilizing additional static pressure taps. Figure 11 shows the placement of these blade taps. The pressure taps had a diameter of .51mm.

All pressure measurements were obtained using one pressure transducer, a Scanivalve model SCSG/D + / -5V/VG signal conditioner, and a set of five

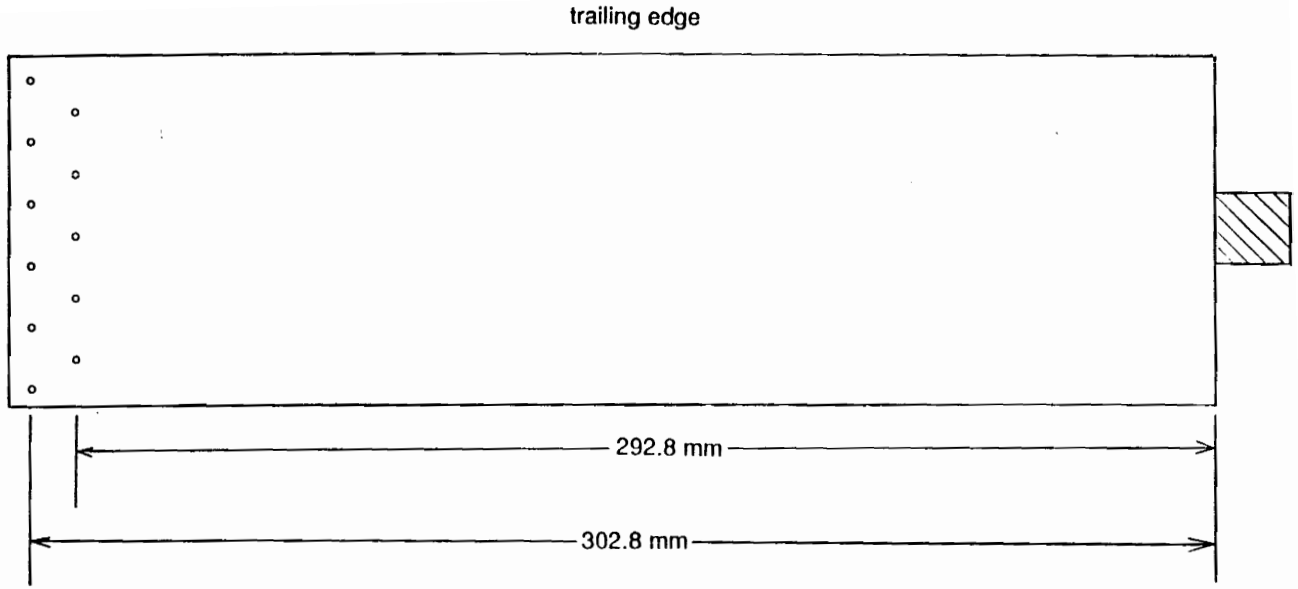

blade span = 304.8mm, chord length = 65.53mm
chordwise distance between pressure taps = 11.794mm
spanwise distance between the two rows of pressure taps = 10mm
distance of first pressure tap from leading edge = 3.268 mm

Figure 10. Corner Region Blade Pressure Tap Locations (Suction Surface)

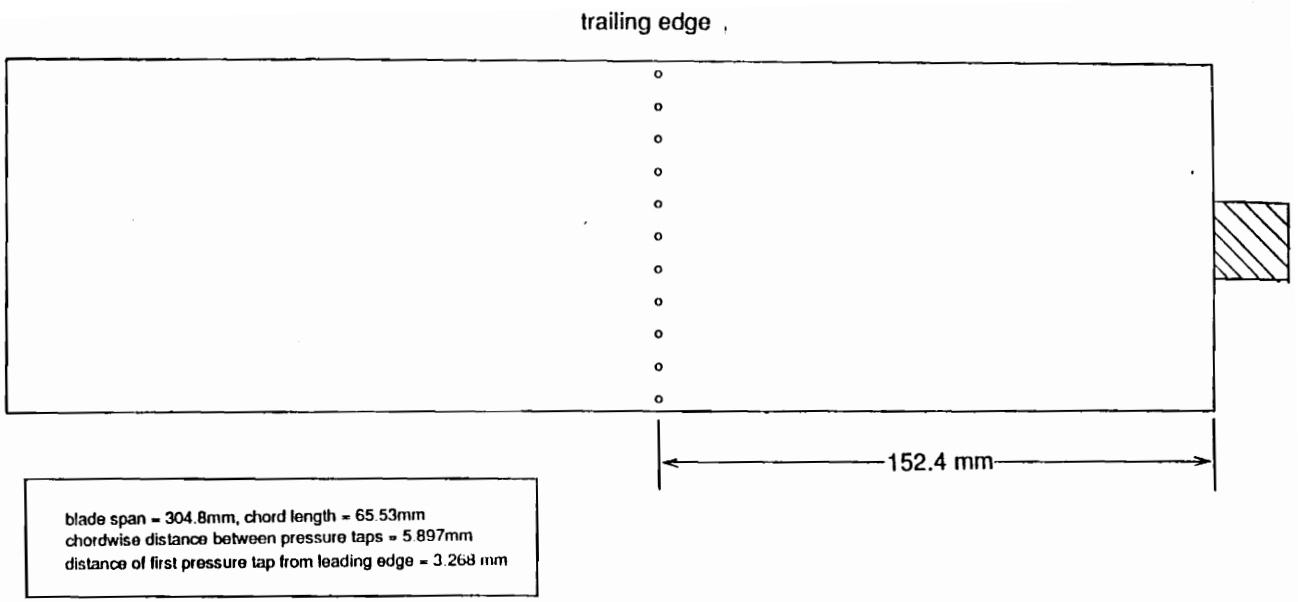

Figure 11. Midspan Blade Pressure Tap Locations (Suction Surface)

Scanivalve model W1260/12P-12T fluid switches. Forty - eight pressure tubes were connected to twelve ports of four of the fluid switches. The outputs from these four fluid switches were connected to the remaining fluid switch, which was connected to the pressure transducer. The transducer output was linearized by the signal conditioner. Calibration of the pressure transducer was done at the beginning of each test run through the use of a 60 degree inclined manometer, which was filled with red gauge oil having a specific gravity of 0.86. An IBM - PC compatible computer, equipped with a Data Translation DT - 2811 data acquisition card, was used to acquire outputs from the pressure transducer. The card had 8 differential analog to digital inputs and two digital outputs. The 12 bit analog to digital input has a range of 0 to 5 volts, resulting in a resolution of 1.22 mv. The computer ran a data acquisition program which controlled the DT - 2811 card and also processed and stored the experimental data.

2.3 Testing Methods and Procedures

2.3.1 Wind Tunnel Setup and Calibration

The cascade was rotated to the desired angle of attack, and then the two horizontal sections of the inlet duct were clamped into place to prevent the cascade from moving. The control lever on the centrifugal blower was set so that the wind tunnel would operate at its maximum velocity. To calibrate the data

acquisition system, the Scanivalve was set to the desired port position. A copper tube was inserted into a column of water to provide a steady pressure for transducer calibration. The water was at room temperature, and the tube was connected to a 60 degree inclined manometer bank and the pressure transducer, through the Scanivalve. After the fluid in the manometer stabilized, readings were taken of the fluid level and the voltage produced by the pressure transducer, in order to complete the calibration process.

2.3.2 Corner Region Pressure Tap Investigation

Pressure tap readings were taken in the cascade corner region for angles of attack from 5 to 29 degrees. The test procedure involved setting the cascade test section at the desired angle of attack and taking pressure readings with the tunnel data acquisition system. In addition to the corner region pressure tap measurements, a series of measurements were taken for the cascade blade midspan region. The resulting data are presented as a series of pressure coefficient profiles.

2.3.3 Downstream Measurements

An initial set of measurements were taken in the cascade wake utilizing the five - hole prism probe. The test procedure involved setting the probe at specified positions along the blade span (along the cascade Z axis) and allowing

the data acquisition system to move the probe in the pitchwise direction (along the cascade Y axis) in order to cover a full blade passage. Measurements were taken at angles of attack ranging from 5 to 29 degrees. The experiments performed for this part of the investigation are shown in Table 1. The results are presented as a series of velocity vector and loss contour plots.

Table 1. Experiments Performed / Initial Downstream Measurements

α^*	V_1(m/s)	Re_c	Re_o	ϖ_2	Yaxis range (mm)	Z axis range (mm)	#Y points	#Z points
5	44.65	183,287	8,866	.0835	58 to -29	-308 to -248	40	18
15	46.00	178,287	8,644	.0504	58 to -29	-308 to -248	40	18
17	48.74	171,977	8,319	.0518	58 to -29	-308 to -248	40	18
19	48.39	175,841	8,506	.0677	58 to -29	-308 to -191	40	20
21	41.75	177,619	8,592	.0728	58 to -29	-308 to -191	40	20
23	49.53	181,177	8,764	.0824	58 to -29	-308 to -191	40	20
25	49.56	179,452	8,681	.1127	58 to -29	-308 to -191	40	20
27	48.13	174,144	8,424	.1660	58 to -29	-308 to -191	40	20
29	48.85	177,808	8,601	.2091	58 to -29	-308 to -191	40	20

After performing the initial downstream measurements, two additional sets of measurements were done which utilized the slotted cascade blades in order to investigate the effects of corner boundary layer blowing. One set of measurements involved modified blade slot exits, and the other involved unmodified blade slot exits. The modification made to the blade slots exit involved the positioning of a thin metal flap over the exit in order to induce the jet air flow to follow the suction surface blade contour more closely (Fig. 6). The flap had a thickness of .05mm. Only one blade slot was used on each of the two blades during the individual data runs. Utilizing the unmodified blade slot exits, an initial set of measurements were taken at 19 and 21 degrees angle of attack. A second set of measurements, involving the modified blade slot exits, were taken for 19, 21, and 23 degrees angles of attack. At each angle of attack setting, the jet air velocity was varied by regulating the rotameter volumetric flow rate. The resulting set of measurements were used to generate pitchwise mass - averaged loss coefficient and loss contour plots. The experiments performed for this phase of the investigation are shown in Table 2.

Table 2. Experiments Performed with Slotted Blades

α^*	Qsb (Li / min)	P gauge down-stream (psi)	V_1 (m/s)	Vj / V_1	Re_c	Re_p	Y axis range (mm)	Z axis range (mm)	# Z Points
19	0	0	46.58	0	168,308	8,141	58 to -29	-304 to -197	10
21	0	0	47.65	0	170,070	8,227	58 to -29	-304 to -197	10
23	0	0	48.47	0	175,815	8,505	58 to -29	-304 to -197	10

a.) slotted blades with external flap

Slot #2									
19	9.62	---	46.74	.69	169,916	8,219	58 to -29	-304 to -197	10
19	21.36	12	47.49	1.56	168,971	8,173	58 to -29	-304 to -197	10
19	26.67	26	47.24	1.98	169,547	8,436	58 to -29	-304 to -197	10
21	9.33	---	47.49	.68	168,987	8,174	58 to -29	-304 to -197	10
21	21.59	12	47.89	1.57	173,006	8,369	58 to -29	-304 to -197	16
21	27.00	26	47.52	1.97	169,349	8,192	58 to -29	-304 to -197	10
23	9.26	---	47.72	.67	173,068	8,372	58 to -29	-304 to -197	10
23	21.38	12	47.69	1.56	172,973	8,367	58 to -29	-304 to -197	10
23	26.76	26	48.15	1.92	174,303	8,431	58 to -29	-304 to -221	15
Slot #1									
19	9.33	---	47.47	.68	169,988	8,223	58 to -29	-304 to -197	10
19	21.45	12	47.02	1.58	168,340	8,143	58 to -29	-304 to -197	10
21	9.21	---	47.98	.67	173,766	8,405	58 to -29	-304 to -197	10
21	21.20	12	47.69	1.54	171,784	8,310	58 to -29	-304 to -197	10
21	26.63	26	47.69	1.94	171,861	8,313	58 to -29	-304 to -197	10
23	9.27	---	47.51	.68	170,690	8,257	58 to -29	-304 to -197	10
23	21.28	12	47.62	1.56	171,523	8,215	58 to -29	-304 to -197	10
23	26.73	26	47.55	1.95	171,823	8,567	58 to -29	-304 to -197	10

b) slotted blades without external flap

Slot #2									
19	21.50	12	47.01	1.59	167,163	8,086	58 to -29	-304 to -197	10
19	26.71	26	46.73	1.99	166,146	8,037	58 to -29	-304 to -197	10
21	21.50	12	47.05	1.59	168,312	8,142	58 to -29	-304 to -197	10
21	27.01	26	47.46	1.97	168,754	8,163	58 to -29	-304 to -197	10
Slot #1									
19	21.36	12	47.38	1.57	170,837	8,264	58 to -29	-304 to -197	10
19	26.83	26	47.59	1.99	169,514	8,200	58 to -29	-304 to -197	10
21	21.35	12	47.11	1.57	170,146	8,230	58 to -29	-304 to -197	10
21	26.92	26	47.53	1.98	172,223	8,332	58 to -29	-304 to -197	10

- 40 data points across the central blade passage were taken for each Z axis location.
- P gauge upstream = 80 psi

3.0 Results and Discussion

In this chapter, the experimental results of the blade tap pressure measurements, initial downstream measurements, and corner region boundary layer blowing results are presented.

3.1 Pressure Tap Measurements

The midspan and corner region pressure tap measurements are presented in Figures 12 through 22 in the form of the non - dimensional quantity, Cp_b, where

$$Cp_b = \frac{P_{t1} - P_{sb}}{P_{t1} - P_{s1}}$$

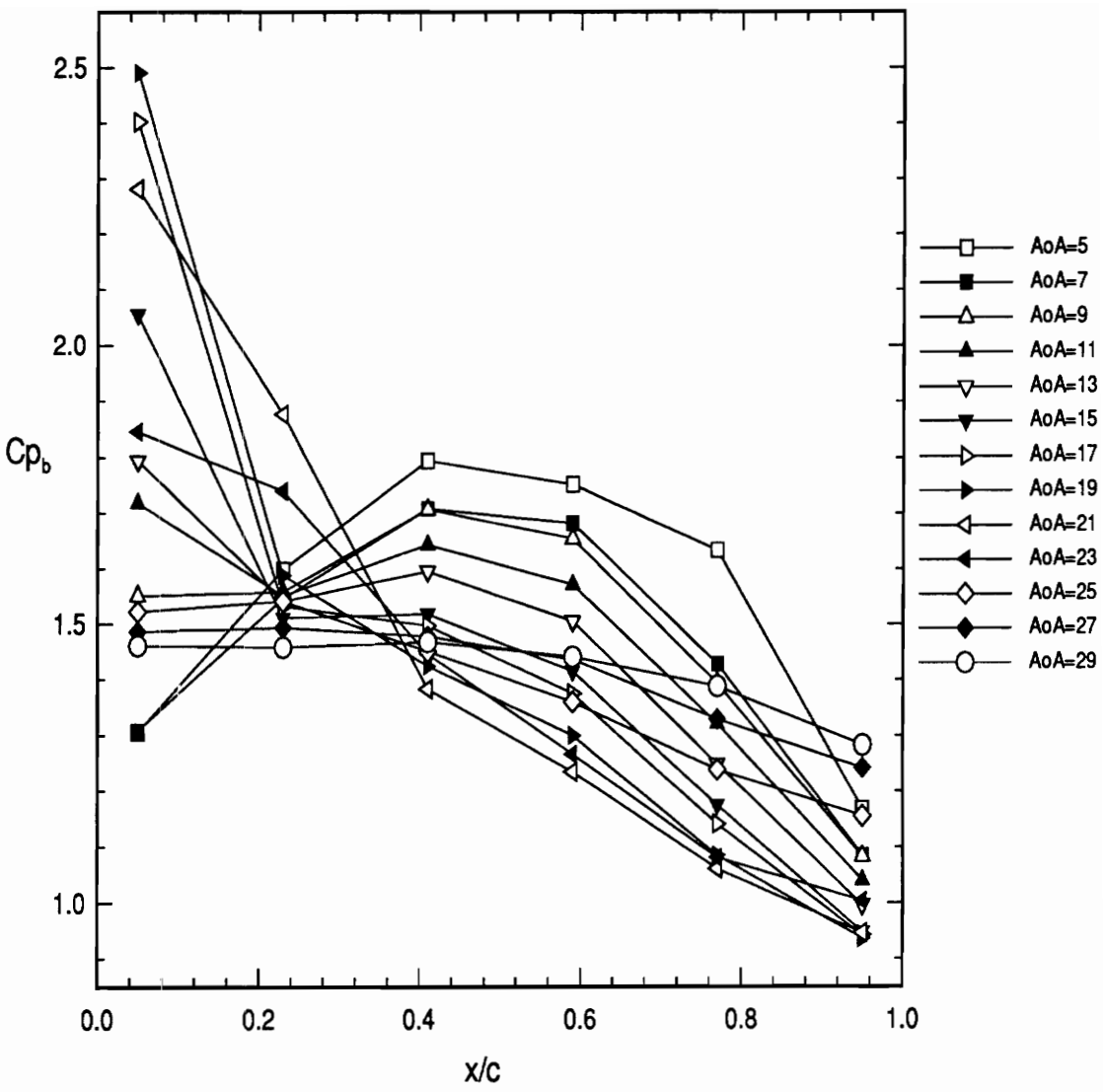

Figure 12. Collection of Blade Suction Surface Pressure Distributions at Midspan (z = -154mm)

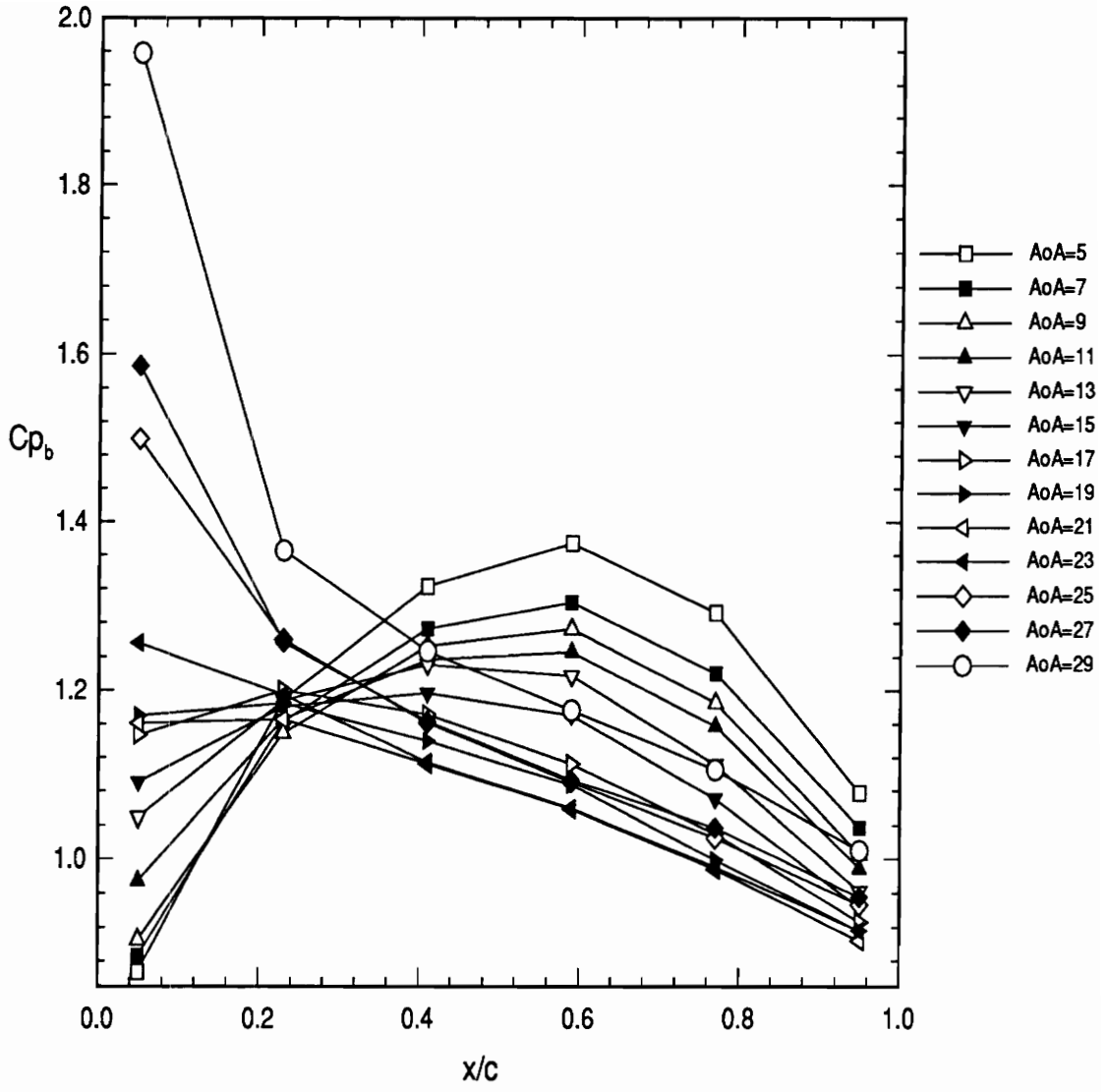

Figure 13. Collection of Blade Suction Surface, Corner Region Pressure Distributions (z = -302.8mm)

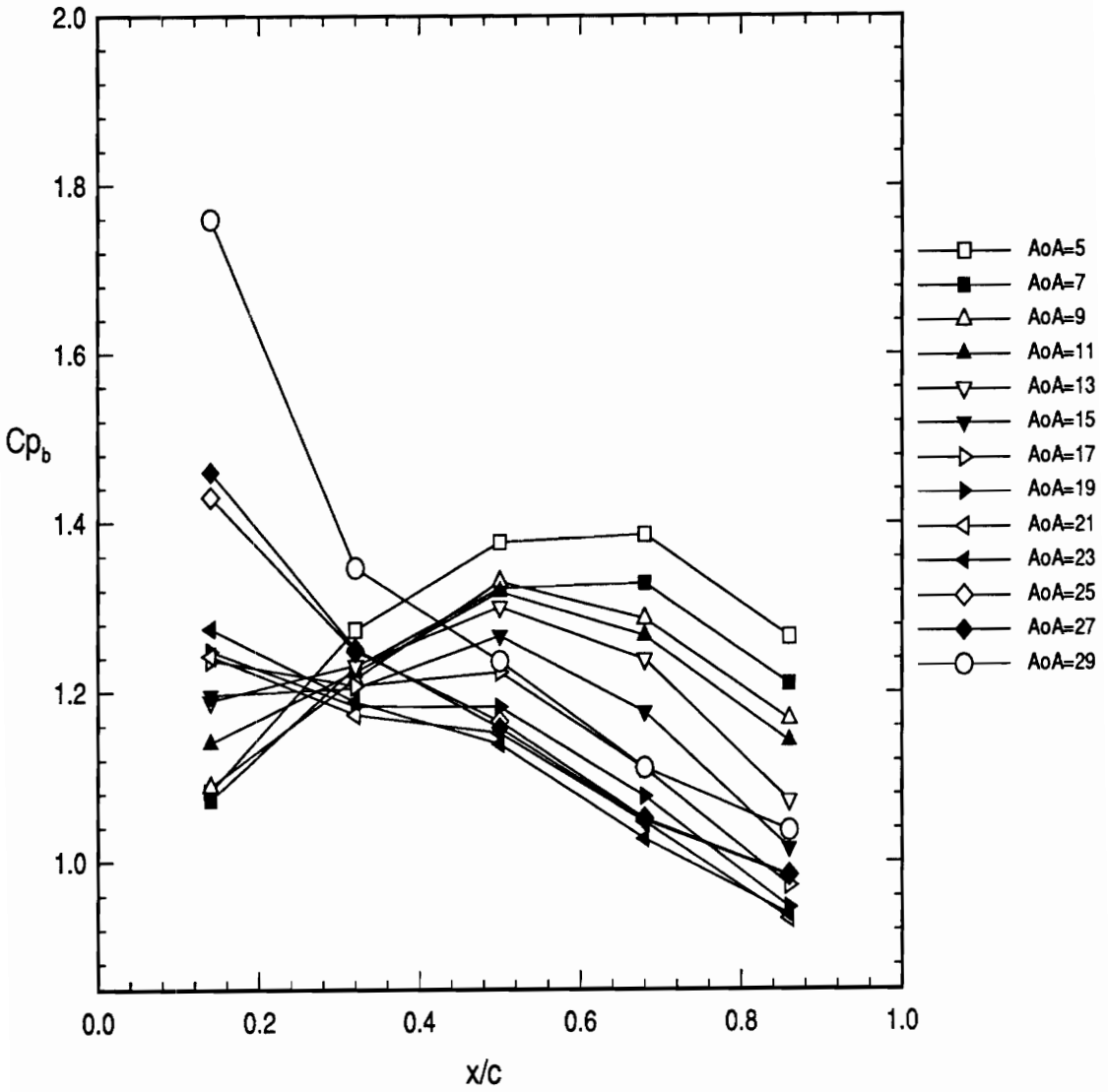

Figure 14. Collection of Blade Suction Surface, Corner Region Pressure Distributions (z = -292.8mm)

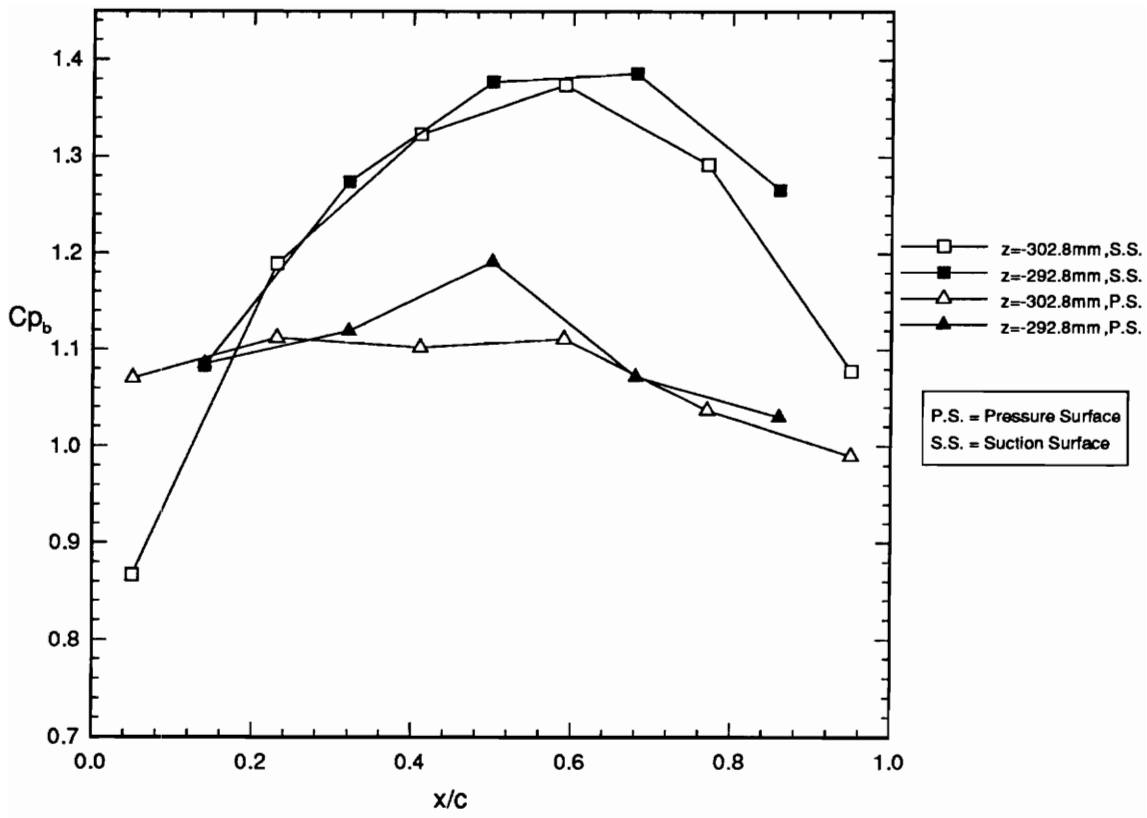

Figure 15. Blade Suction Surface and Pressure Surface Corner Region Pressure Distribution, $\alpha^* = 5°$, $V_1 = 44.65$ m/s, $Re_c = 183,287$

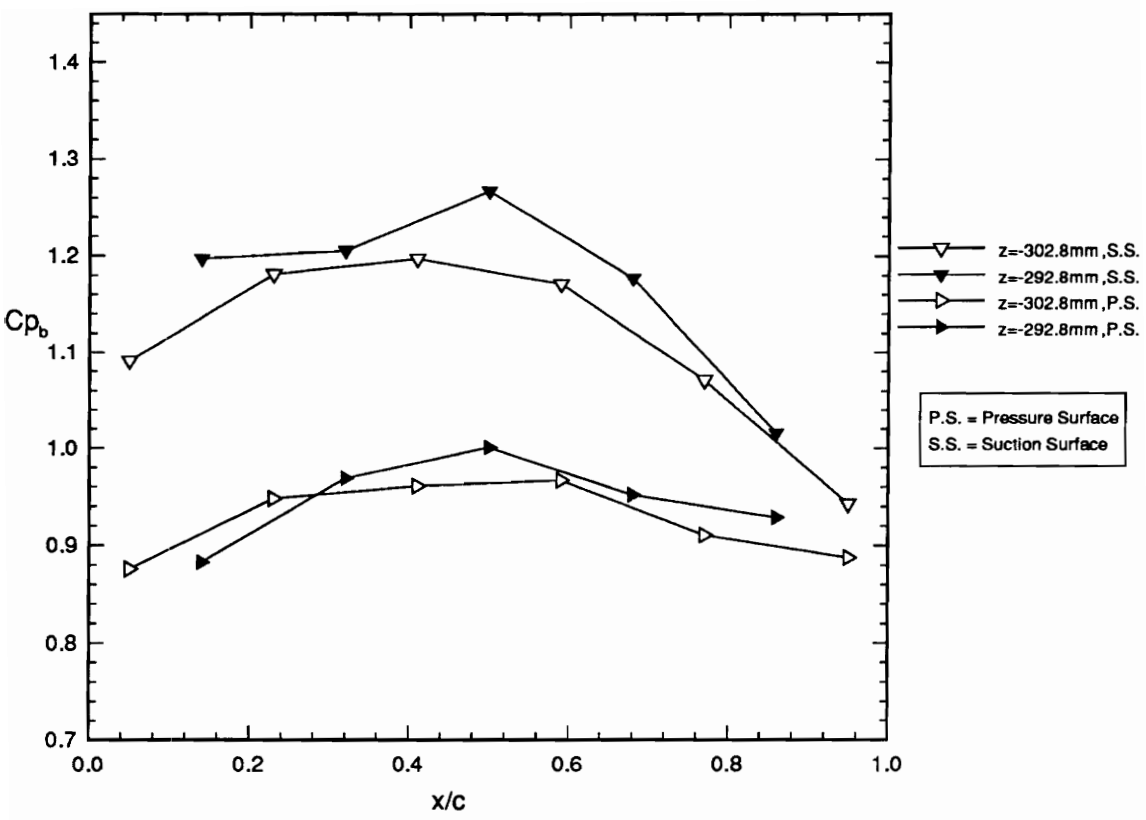

Figure 16. Blade Suction Surface and Pressure Surface Corner Region Pressure Distribution, $\alpha^* = 15°$, $V_1 = 46.00$ m/s, $Re_c = 178{,}287$

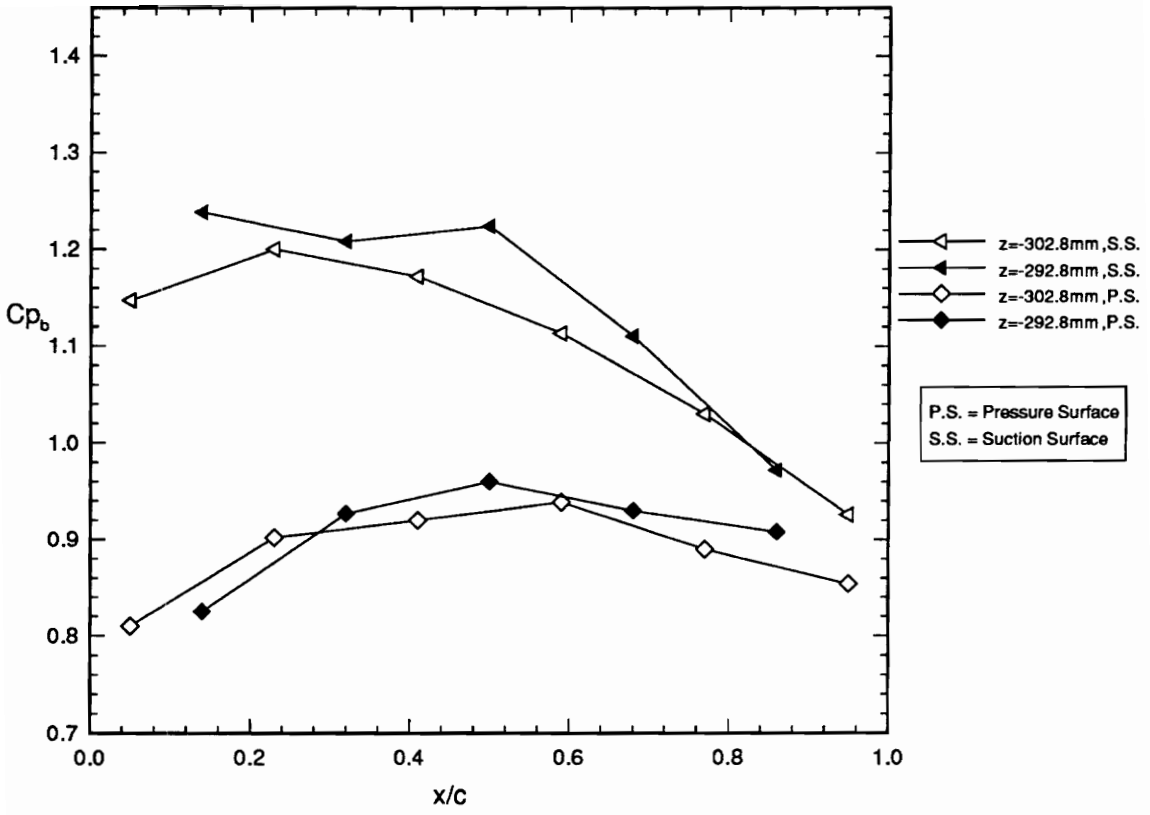

Figure 17. Blade Suction Surface and Pressure Surface Corner Region Pressure Distribution, $\alpha^* = 17°$, $V_1 = 48.74$ m/s, $Re_c = 171{,}977$

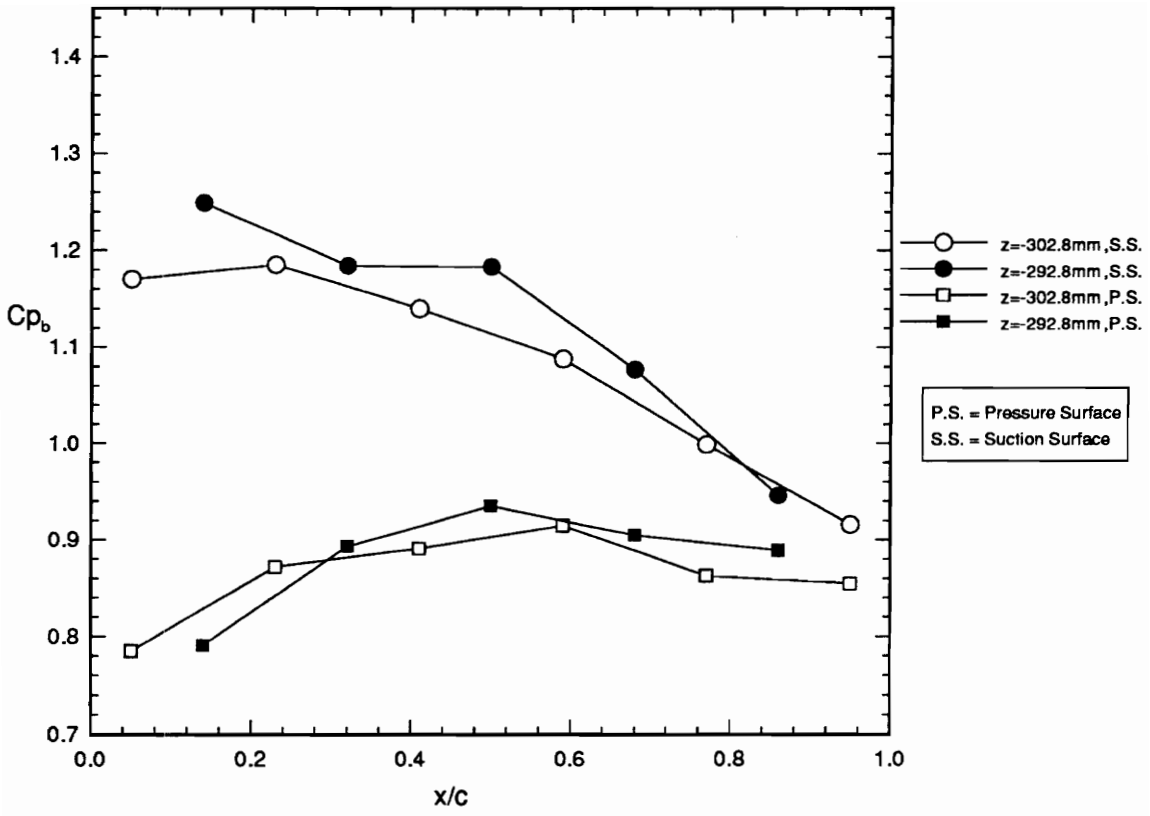

Figure 18. Blade Suction Surface and Pressure Surface Corner Region Pressure Distribution, $\alpha^* = 19°$, $V_1 = 48.39$ m/s, $Re_c = 175{,}841$

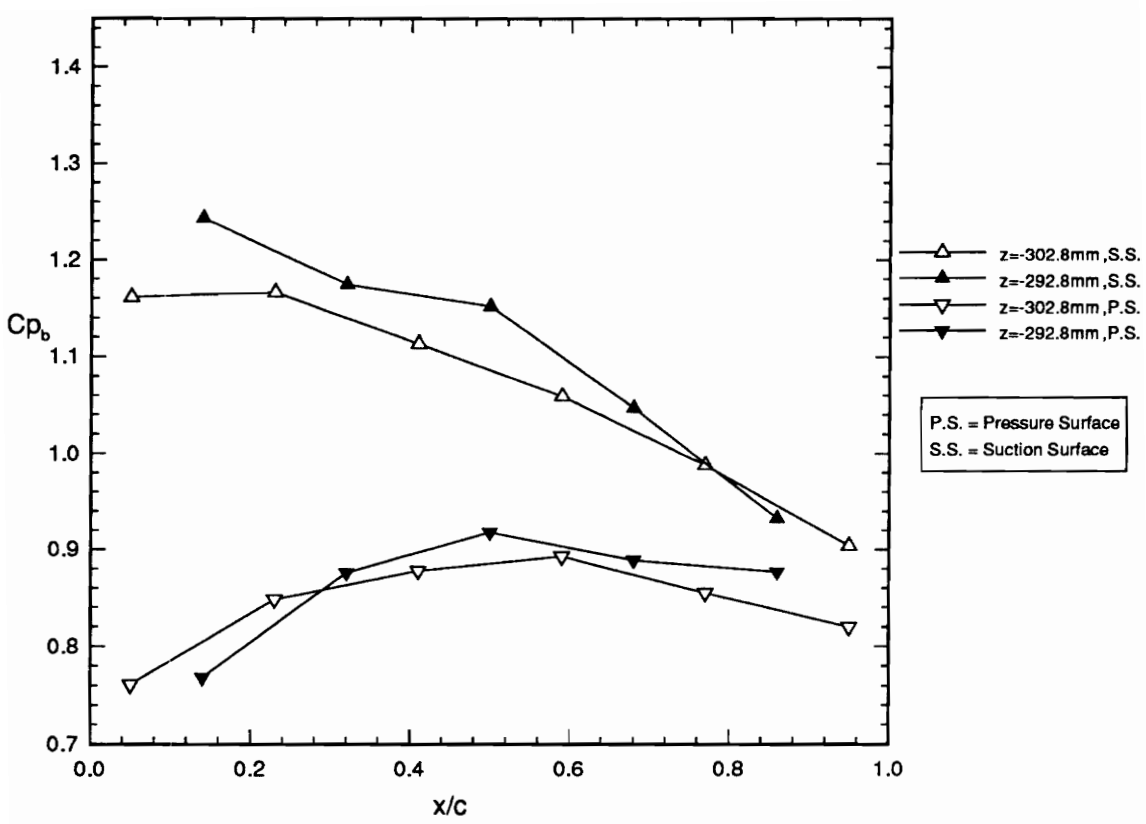

Figure 19. Blade Suction Surface and Pressure Surface Corner Region Pressure Distribution, $\alpha^* = 21°$, $V_1 = 47.75$ m/s, $Re_c = 177{,}619$

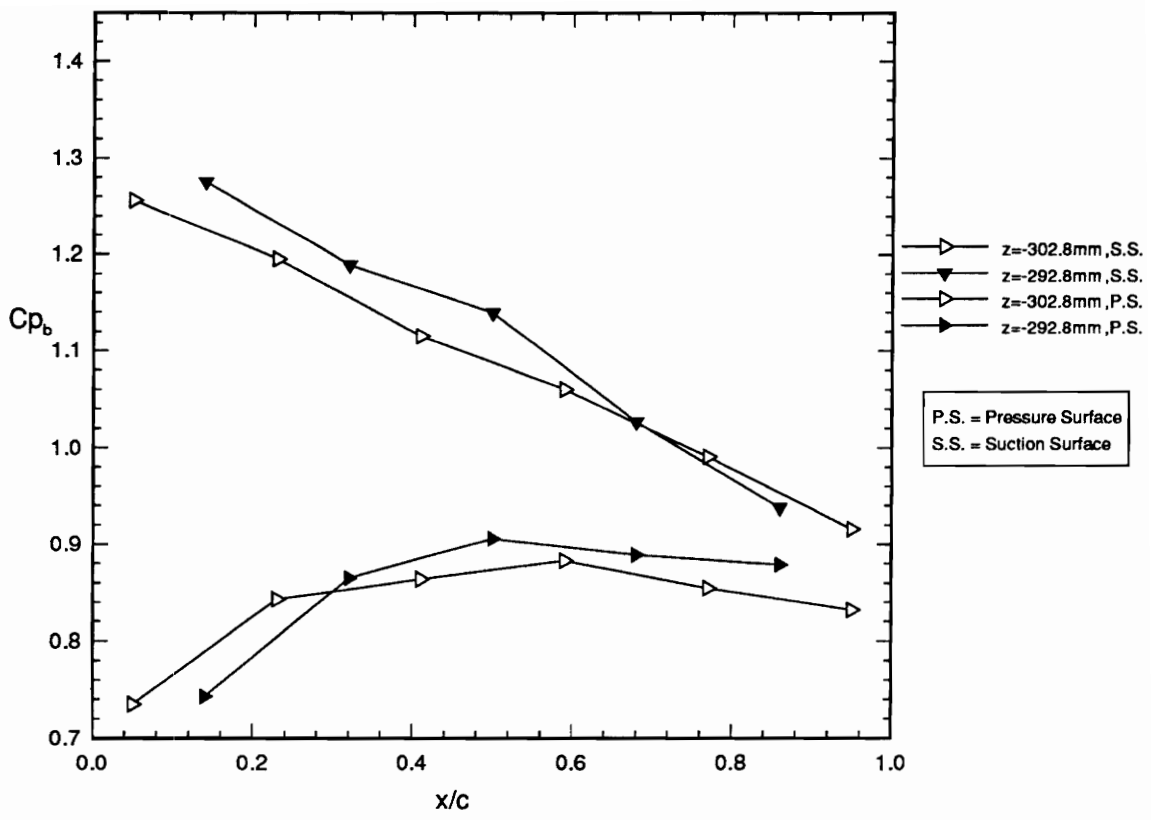

Figure 20. Blade Suction Surface and Pressure Surface Corner Region Pressure Distribution, $\alpha^* = 23°$, $V_1 = 49.53$ m/s, $Re_c = 181,177$

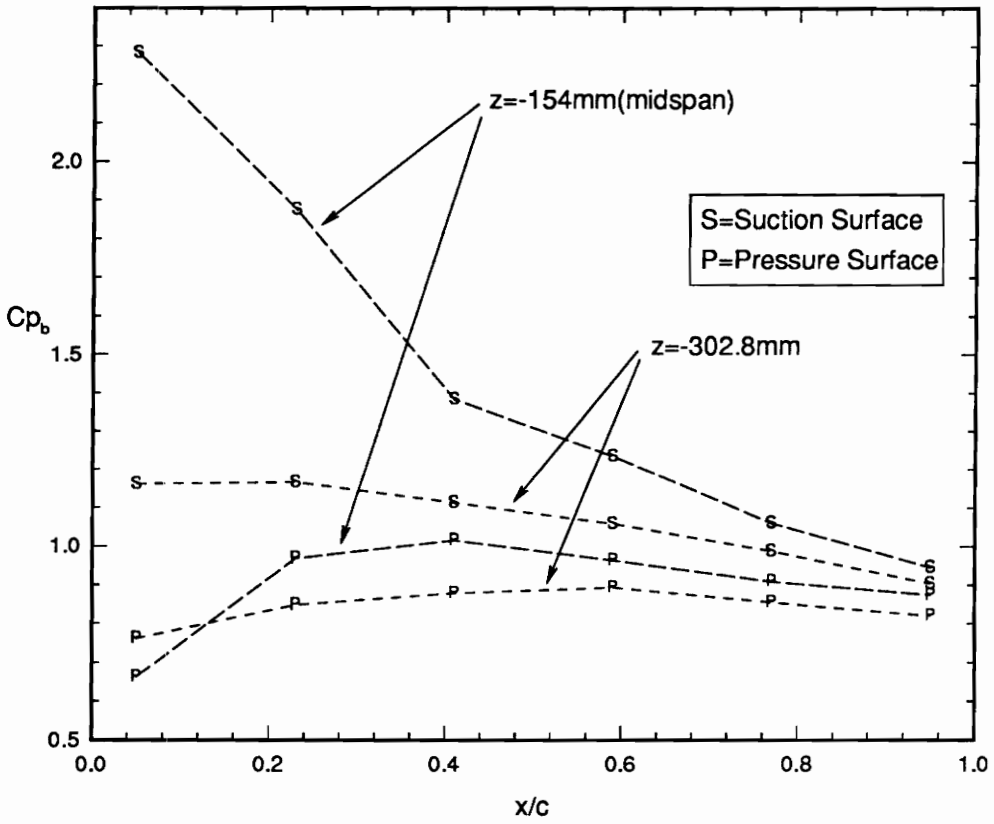

Figure 21. Comparison Between Midspan and Corner Region Blade Surface Pressure Distributions, $\alpha^*=21°$

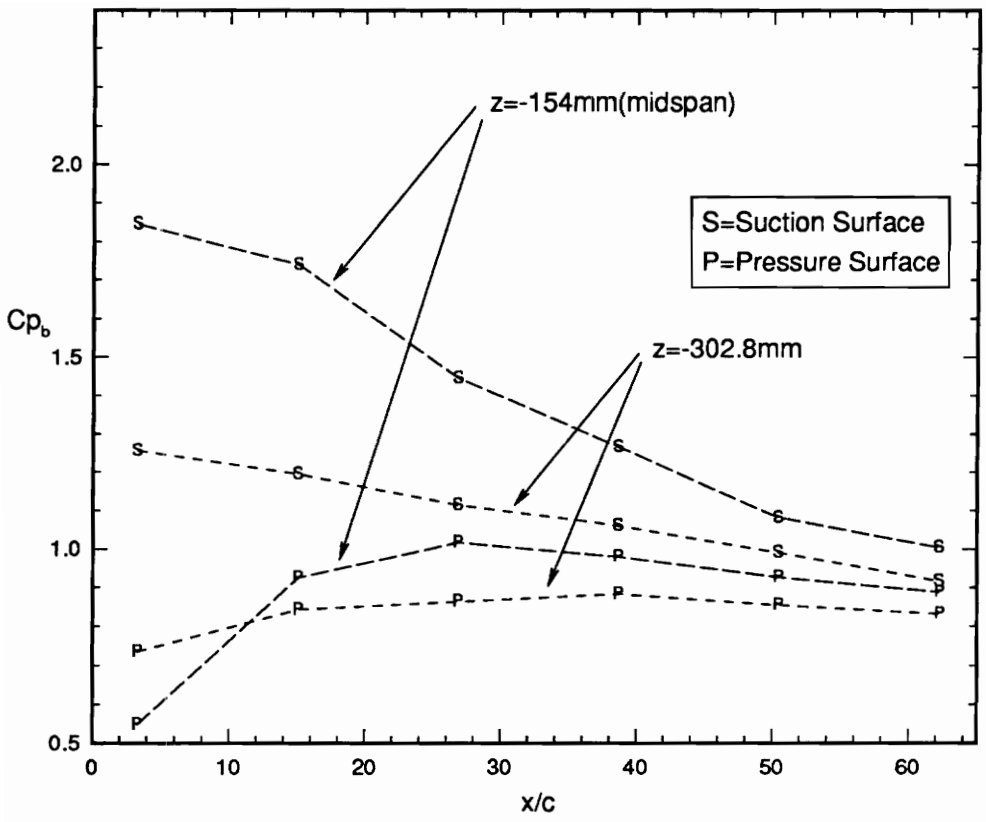

Figure 22. Comparison Between Midspan and Corner Region Blade Surface Pressure Distributions, $\alpha^*=23°$

and

P_{t1} = upstream total pressure

P_{s1} = upstream static pressure

P_{sb} = blade surface pressure

Since the present investigation is concerned with the flow in the cascade corner region, only the suction surface pressure tap measurements will be discussed. The corresponding pressure tap measurements taken along the blade pressure surface are shown in Appendix D. No useful information regarding corner stall could be determined from the pressure surface measurements. The midspan pressure tap measurements for the blade suction surface appear in Fig. 12, and they were used as a comparison basis for the corner region pressure tap measurements.

From the results of Russ[8] who did a series of inlet velocity surveys in front of the blade row for a cascade test section having a solidity of one, the entry boundary layer was found to be turbulent for a Reynolds number range of 0.62×10^5 to 2.09×10^5. The measurements were taken 0.8 chords upstream of the cascade origin (along the cascade X axis) at three different Y axis locations, centered at Y = 0mm. The resulting boundary layer measurements showed little variation with Reynolds number. The entry sidewall boundary layer thickness was shown to increase in the +Y direction, a result of the longer distance from the wind tunnel nozzle exit to the blade row in which the boundary layer could

develop. From his results, the conclusion was reached that, for an angle of attack range from 5 to 35 degrees, the entry sidewall boundary layer to the middle blade passage was no more than 19mm thick. The entry sidewall boundary layer measurements performed by Russ[8] are believed applicable to the current 1.5 solidity cascade since both where constructed using the same sidewall material, and the distances from the wind tunnel nozzle exit to the blade row for each of the cascade test sections are the same.

In general, the resulting pressure coefficient (Cp) values at midspan were greater than the corresponding Cp values in the corner region. This correspondence held true for the full angle of attack (AoA) test range. In Fig. 12, the pressure coefficient profile, corresponding to 5 degrees AoA, exhibits a maximum value near the blade midchord region. As the AoA was increased the Cp values in this region decreased, while the values close to the blade leading edge increased. A maximum Cp value of 2.5 was recorded, at 19 degrees AoA, by the pressure tap located closest to the blade leading edge. This is a result of the acceleration of the free stream tunnel flow over the blade leading edge followed by flow deceleration along the rest of its chord length. The Cp value closest to the blade leading edge decreased significantly as the cascade AoA was increased from 19 to 21 degrees. At 23 degrees AoA, the leading edge Cp value dropped to 1.85, its greatest single change in value from one cascade AoA

setting to another. The leading edge Cp value decreased to 1.54 when the cascade test section was moved to an AoA setting of 25 degrees.

The pressure coefficient results shown in Fig. 12 support the idea of boundary layer separation beginning at the blade trailing edge and eventually growing to encompass the cascade blade leading edge flow. As boundary layer separation becomes more severe along the suction surface of the blade, fluid acceleration around the airfoil leading edge decreases. This results in smaller Cp values at the blade leading edge, which serves as an indication of the onset of leading edge stall. At 29 degrees AoA, the Cp profile exhibits the characteristic flattened - out appearance for that of the suction surface of a fully stalled airfoil. This indicates that the present cascade setup undergoes full blade stall at angles of attack greater than 29 degrees.

The corner region blade pressure tap measurements, and the resulting Cp profiles, followed the same general trend described of the midspan pressure tap measurements shown in Fig. 12, for the lower AoA settings. However, from looking at Fig. 13 (z = -302.8mm), the Cp profile corresponding to 29 degrees AoA does not have the shape which corresponds to that of a fully stalled airfoil (the Cp profile of Fig. 12 for 29 degrees AoA). In Fig. 13, the leading edge pressure coefficients show a steady increase in value as the AoA is increased, with a maximum value of 1.96 recorded for 29 degrees AoA. The same trend was evident from looking at the other set of corner region pressure tap

measurements, taken at a spanwise location of z = -292.8mm (Fig. 14). In these results, the pressure tap located closest to the blade leading edge recorded a value of 1.76 at 29 degrees AoA. These results indicate that at 29 degrees AoA, classical leading edge separation does not occur in the corner region even though the rest of the blade span may be fully stalled. This is believed to be a result of the three - dimensionality of the boundary layer in the corner region. The results of the corner region pressure tap measurements are supported by the flow visualization work done by Russ[8]. He was able to show that the corner boundary layers were able to avoid fully separating from the blade suction surface, in comparison to the rest of the blade span, as the cascade angle of attack was increased.

Figures 15 through 20 show a comparison of the two sets of corner region pressure tap measurements for an AoA range of 5 to 23 degrees. The results indicate that the majority of the Cp values, notably the suction surface Cp values, are somewhat larger for the row of pressure taps located at z = -292.8mm. This is thought to be a result of the sidewall boundary layer, which is believed to be no more than 19mm thick at entry to the cascade blade row, as indicated by Russ[8]. The corner region pressure taps lie within the stated spanwise extent of the entry sidewall boundary layer thickness. If the corner boundary layer is viewed as a combination of the sidewall and blade profile boundary layers, and

the sidewall boundary layer is much more developed, the blade surface velocities would tend to increase away from the cascade sidewall. This is due to the fact that the velocity distribution within a boundary layer increases as the free - stream flow is approached. This increase in blade surface velocities, from the cascade sidewall area towards midspan, results in an increase in Cp values away from the cascade sidewall.

At 21 degrees AoA, a comparison of the pressure tap measurements for the blade midspan and corner regions are shown (Fig. 21). From the results, it is evident that the midspan Cp values, especially for the forward section of the airfoil extending from x/c = .4 to the leading edge, are larger than the corner region Cp values. The large difference in suction surface Cp values for the forward part of the blade serves as an indication of the significant differences in the surface velocities between the corner and midspan regions. This, as discussed above, is

believed to be a result of sidewall boundary layer growth. The same description is applicable to the results shown in Fig. 22, corresponding to 23 degrees AoA.

3.2 Initial Downstream Measurements

The mass - averaged loss coefficient values shown in Fig. 23 and Table 1 were found by using a numerical integration procedure to calculate:

$$\overline{\omega}_2 = \frac{\iint_{passage} \omega \cdot V_{2x} \cdot \rho \cdot dy \cdot dz}{\iint_{passage} V_{2x} \cdot \rho \cdot dy \cdot dz}$$

where the total pressure loss coefficient was defined as:

$$\omega = \frac{P_{t1} - P_{t2}}{P_{t1} - P_{s1}}$$

and the density, ρ, was assumed constant (incompressible flow assumed). From looking at Fig. 23, a minimum value of .0504 for the mass - averaged loss coefficient, ϖ_2, occurred at 15 degrees AoA. A steep increase in ϖ_2, corresponding to a significant increase in blade profile stall, begins at 23 degrees AoA and reaches a maximum of .2091 at 29 degrees AoA. The values calculated for ϖ_2 are mass - weighted values which include the total pressure losses due to the cascade sidewall boundary layer growth. This was considered appropriate for this investigation since the sidewall boundary layer is a primary component of the corner flow structure.

Figures 24 through 41 contain a series of loss contour plots and secondary flow velocity vector plots. To generate the loss contour plots, a value for the total

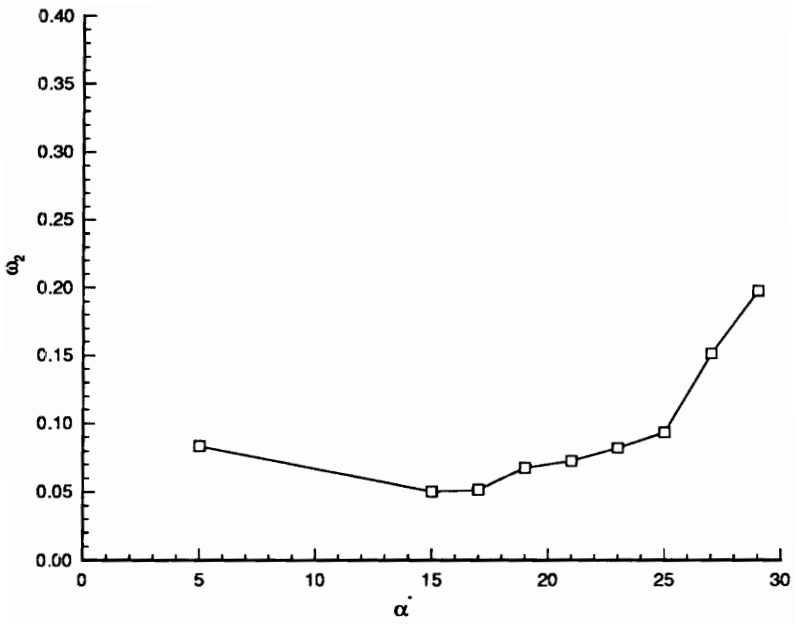

Figure 23. Mass - Averaged Loss Coefficients

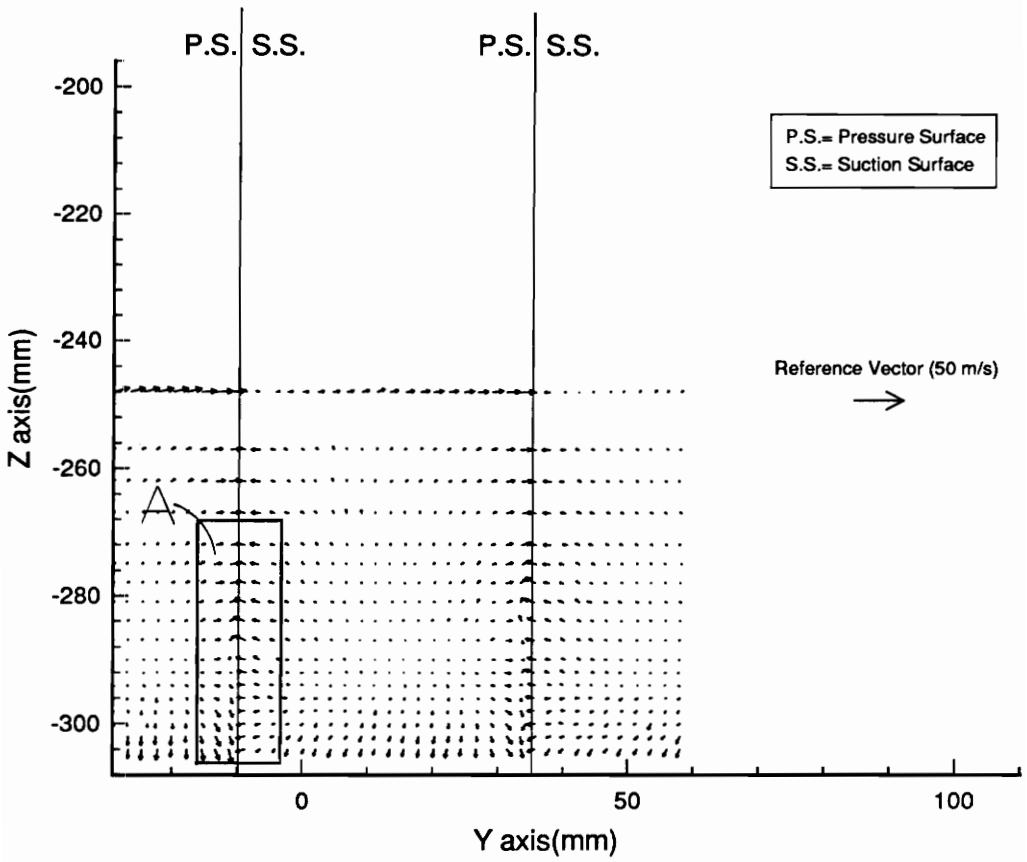

Figure 24. Downstream Secondary Flow Plot (No Blowing Condition)
$\alpha^* = 5°$, $V_1 = 44.65$ m/s, $Re_c = 183,287$

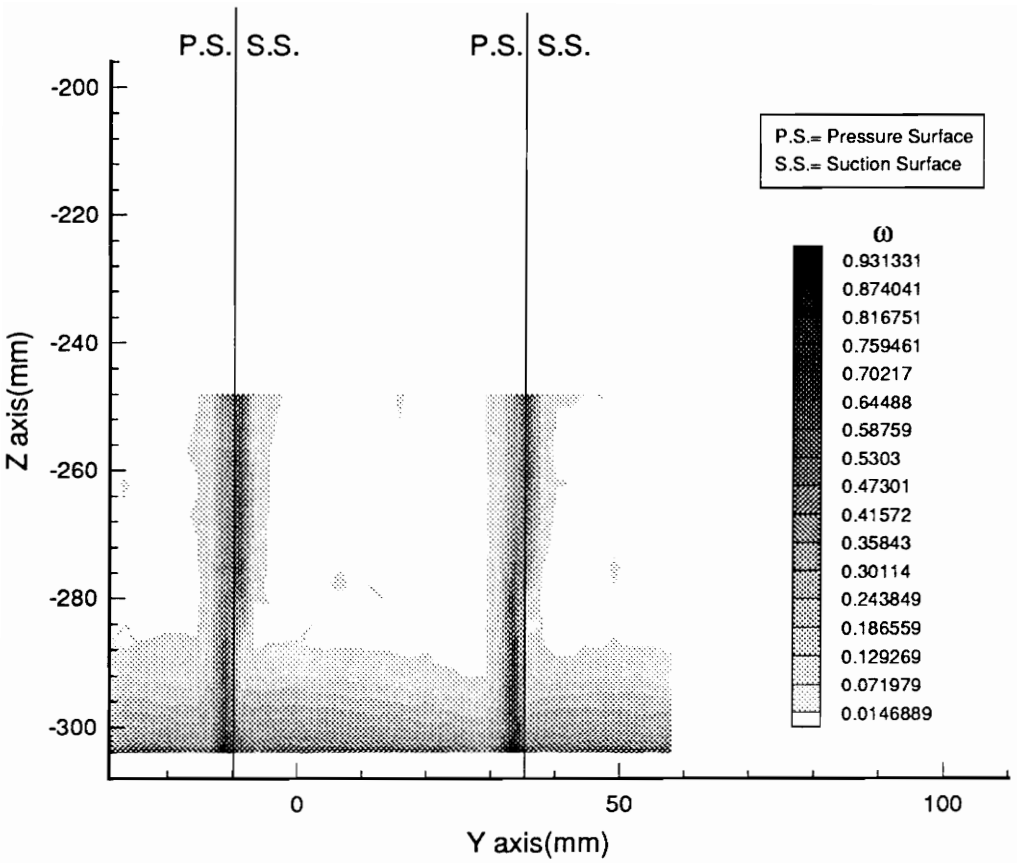

Figure 25. Downstream Loss Contour Plot (No Blowing Condition)
$\alpha^* = 5°$, $V_1 = 44.65$ m/s, $Re_c = 183{,}287$

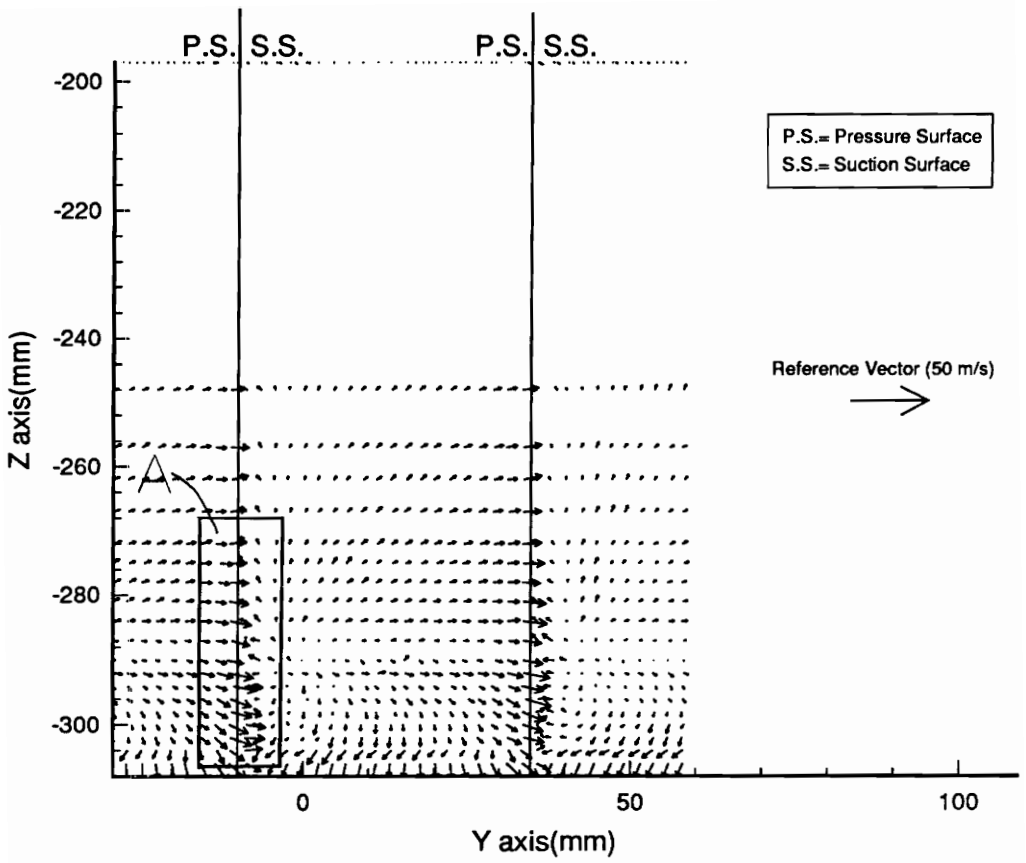

Figure 26. Downstream Secondary Flow Plot (No Blowing Condition)
$\alpha^* = 15°$, $V_1 = 46.00$ m/s, $Re_c = 178{,}287$

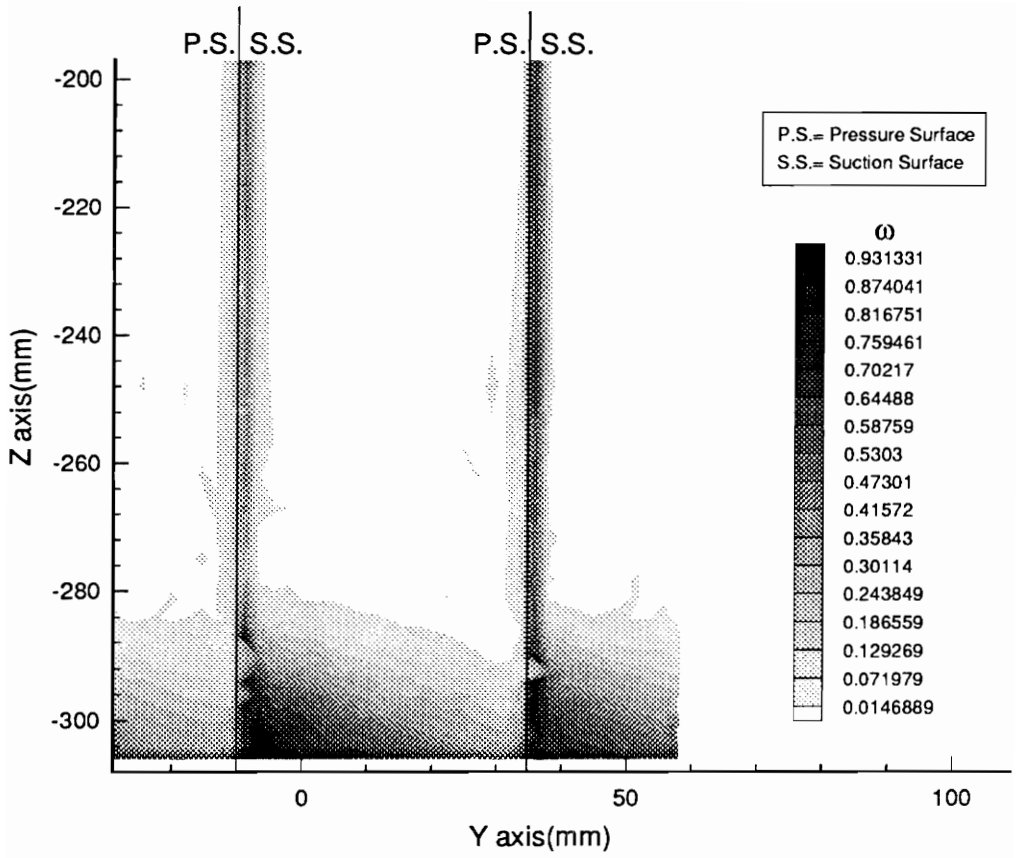

Figure 27. Downstream Loss Contour Plot (No Blowing Condition)
$\alpha^* = 15°$, $V_1 = 46.00$ m/s, $Re_c = 178{,}287$

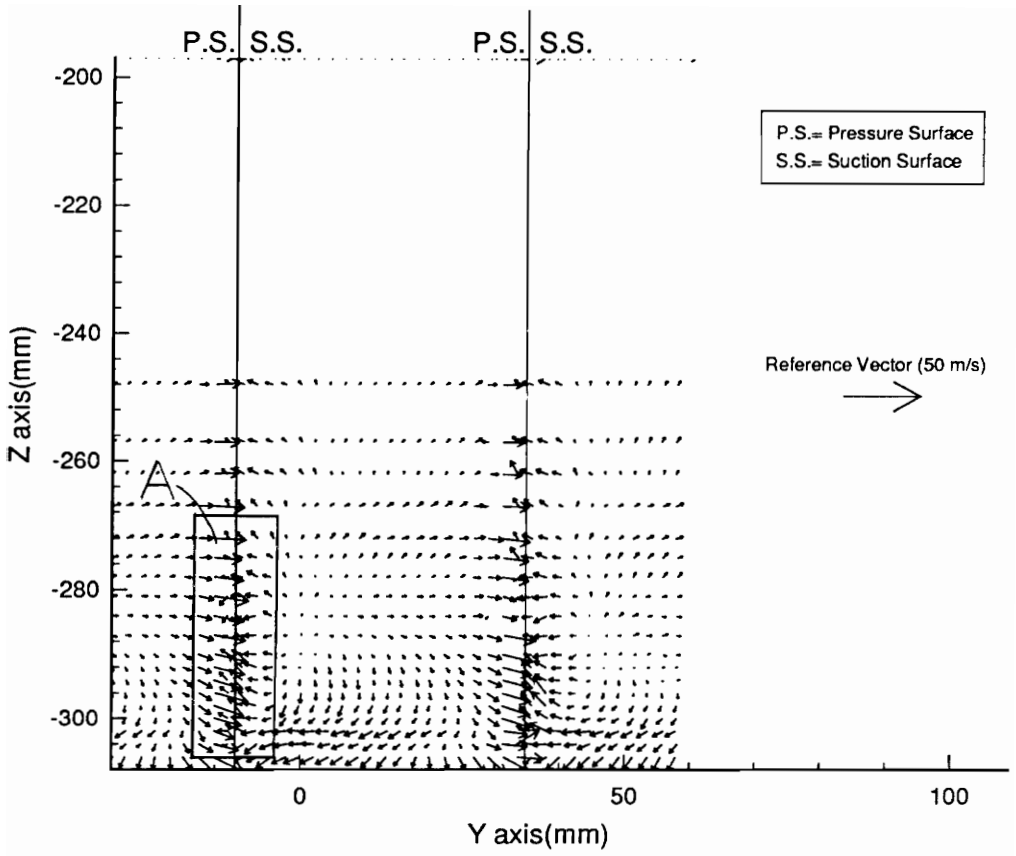

Figure 28. Downstream Secondary Flow Plot (No Blowing Condition)
$\alpha^* = 17°$, $V_1 = 48.74$ m/s, $Re_c = 171{,}977$

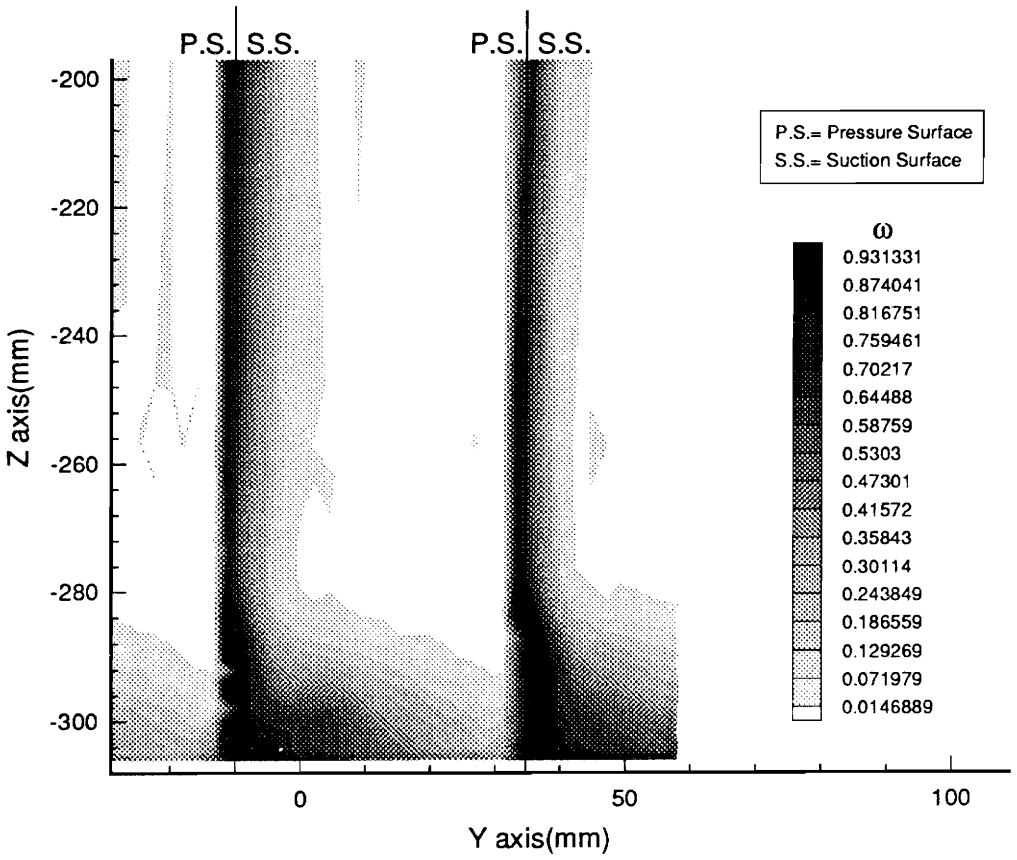

Figure 29. Downstream Loss Contour Plot (No Blowing Condition)
$\alpha^* = 17°$, $V_1 = 48.74$ m/s, $Re_c = 171{,}977$

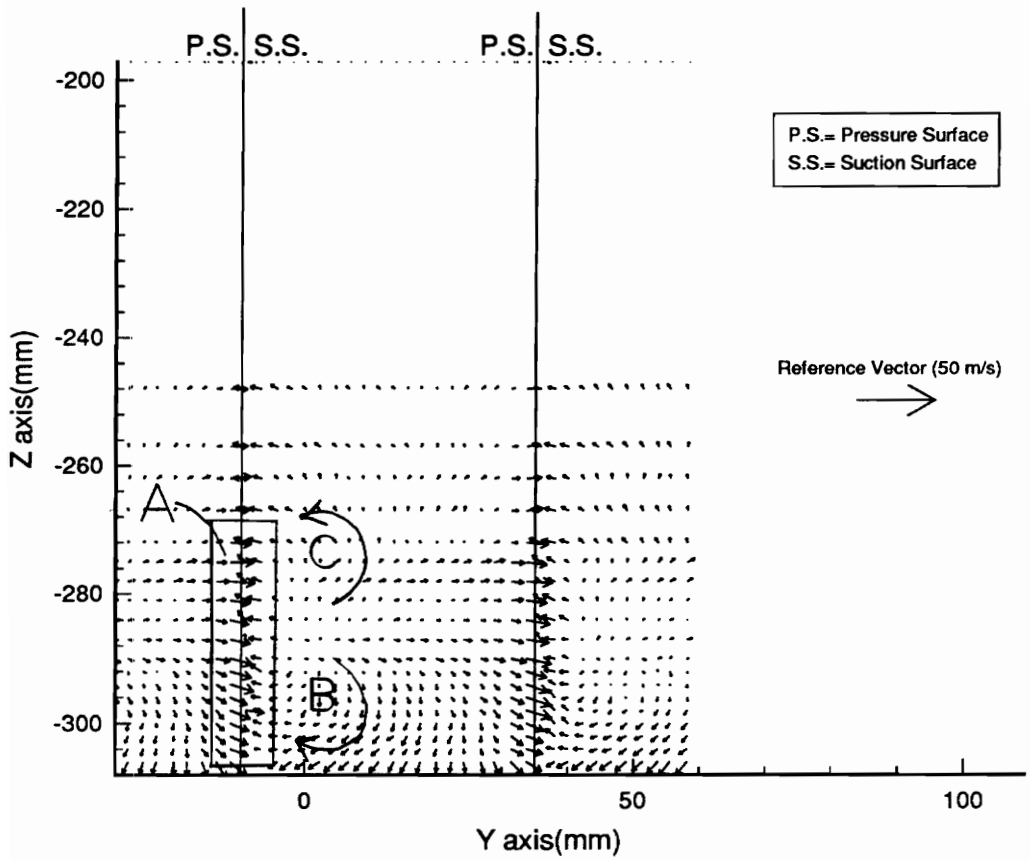

Figure 30. Downstream Secondary Flow Plot (No Blowing Condition)
$\alpha^* = 19°$, $V_1 = 48.39$ m/s, $Re_c = 175, 841$

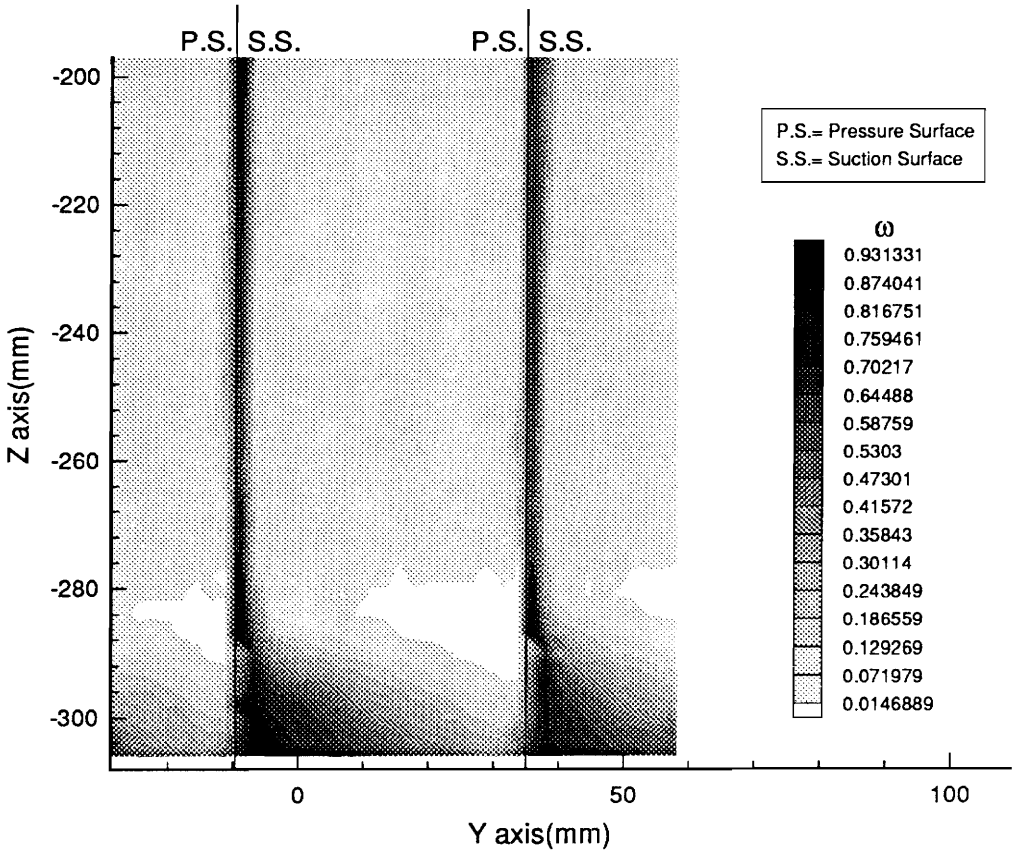

Figure 31. Downstream Loss Contour Plot (No Blowing Condition)
$\alpha^* = 19°$, $V_1 = 48.39$ m/s, $Re_c = 175{,}841$

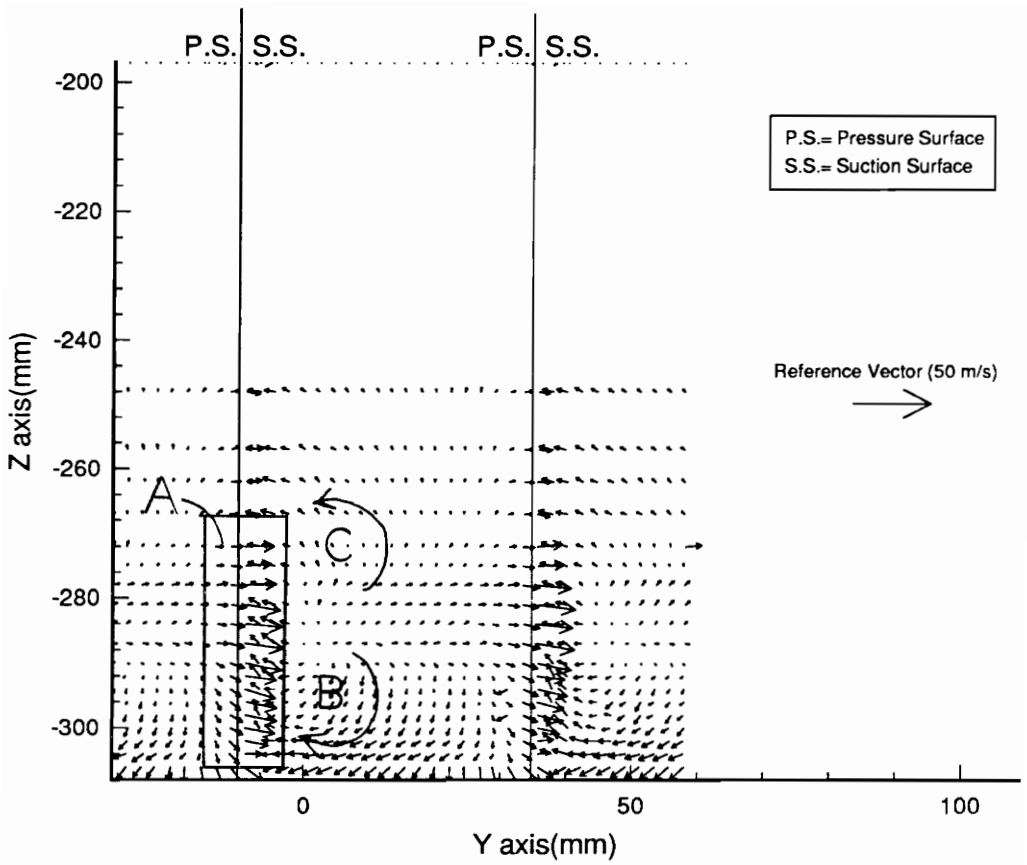

Figure 32. Downstream Secondary Flow Plot (No Blowing Condition)
$\alpha^* = 21°$, $V_1 = 41.75$ m/s, $Re_c = 177{,}619$

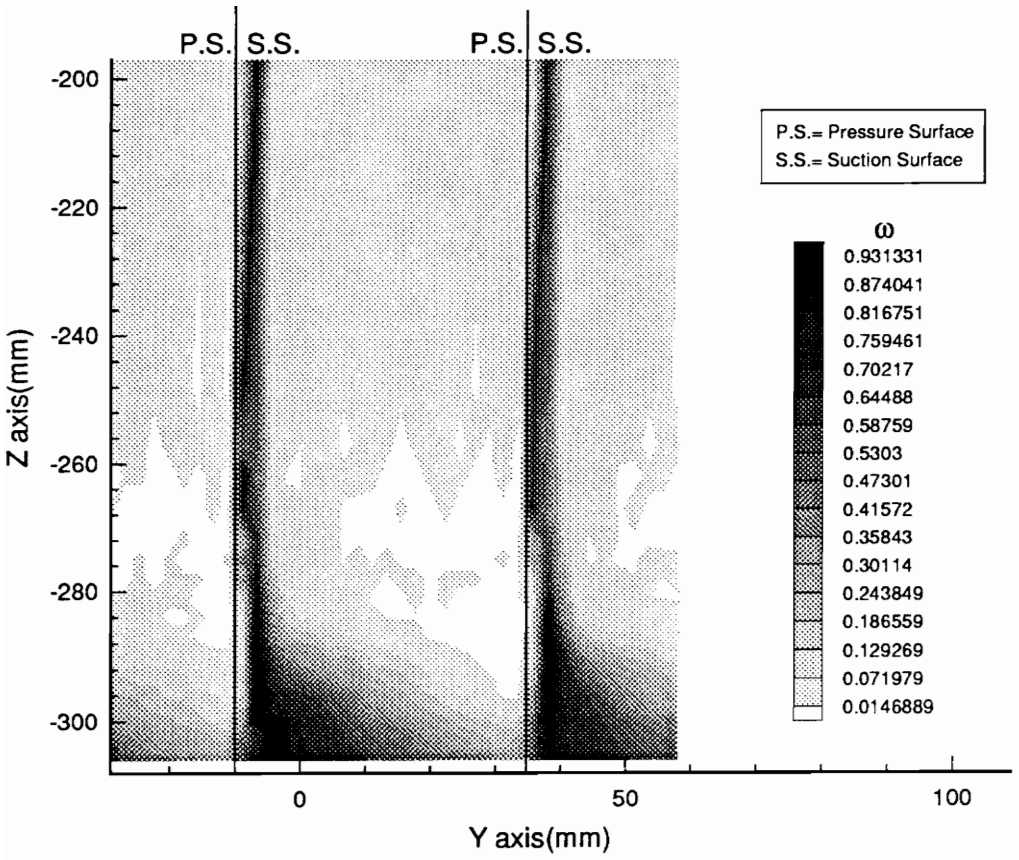

Figure 33. Downstream Loss Contour Plot (No Blowing Condition)
$\alpha^* = 21°$, $V_1 = 41.75$ m/s, $Re_c = 177{,}619$

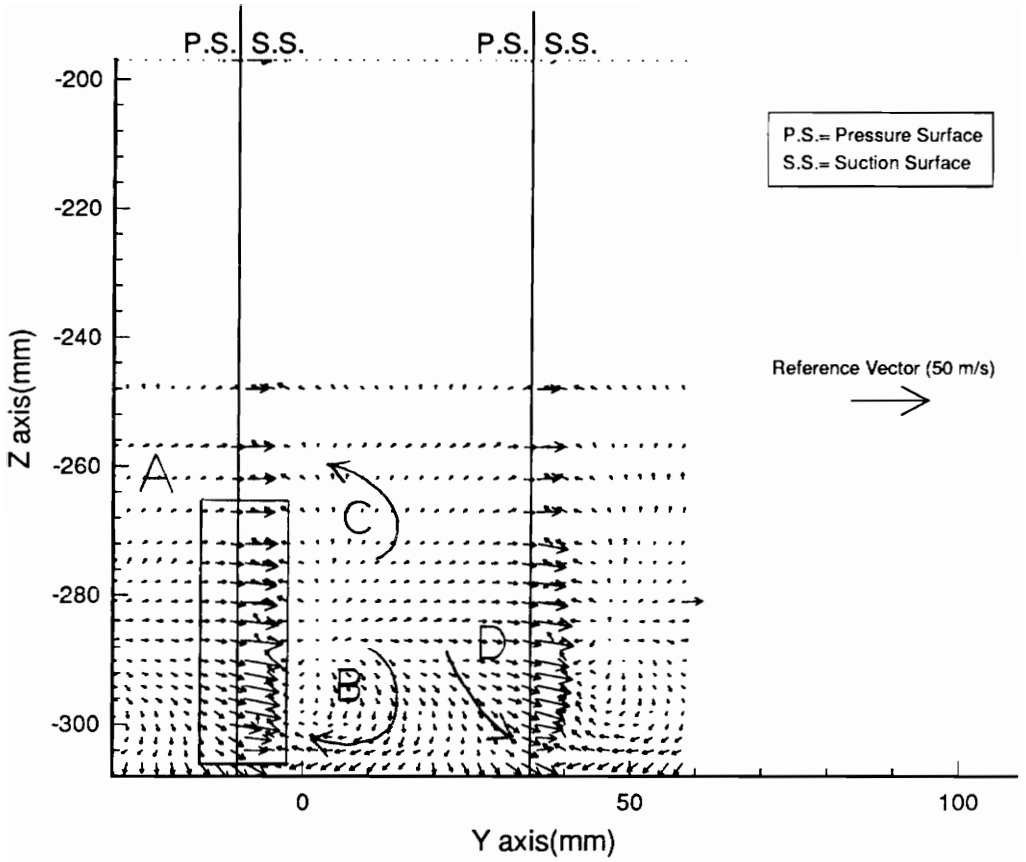

Figure 34. Downstream Secondary Flow Plot (No Blowing Condition)
$\alpha^* = 23°$, $V_1 = 49.53$ m/s, $Re_c = 181{,}177$

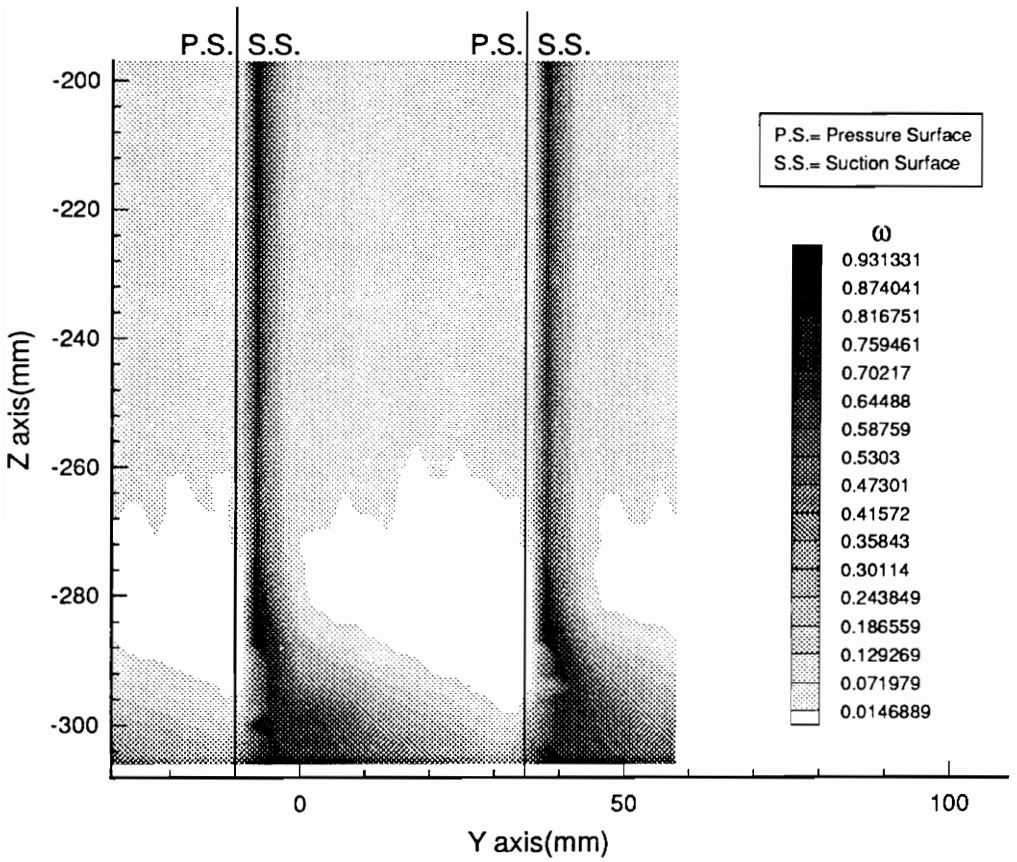

Figure 35. Downstream Loss Contour Plot (No Blowing Condition)
$\alpha^* = 23°$, $V_1 = 49.53$ m/s, $Re_c = 181{,}177$

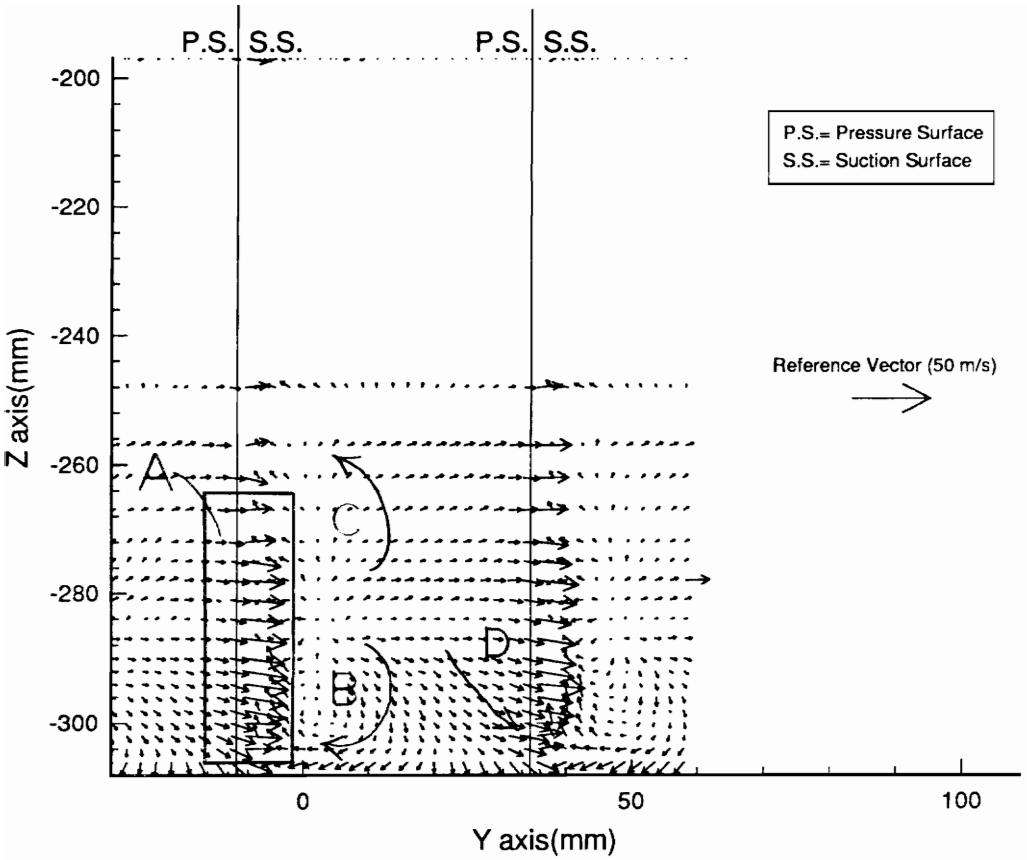

Figure 36. Downstream Secondary Flow Plot (No Blowing Condition)
$\alpha^* = 25°$, $V_1 = 49.56$ m/s, $Re_c = 179{,}452$

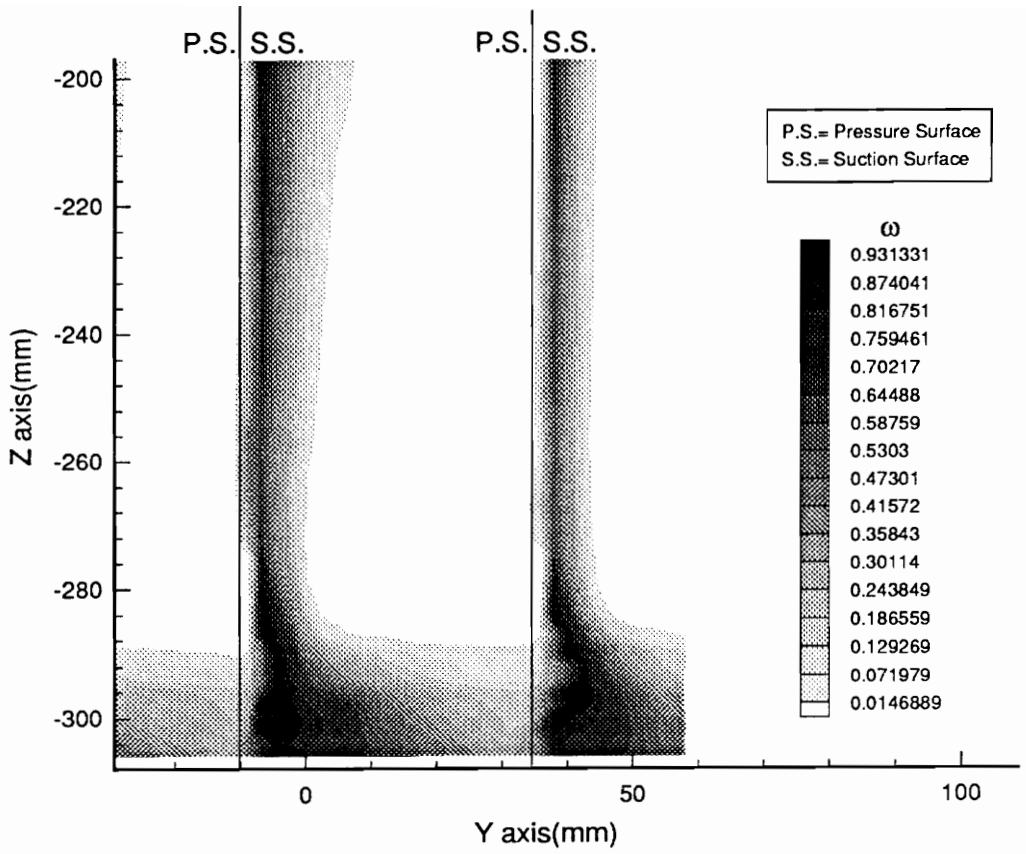

Figure 37. Downstream Loss Contour Plot (No Blowing Condition)
$\alpha^* = 25°$, $V_1 = 49.56$ m/s, $Re_c = 179{,}452$

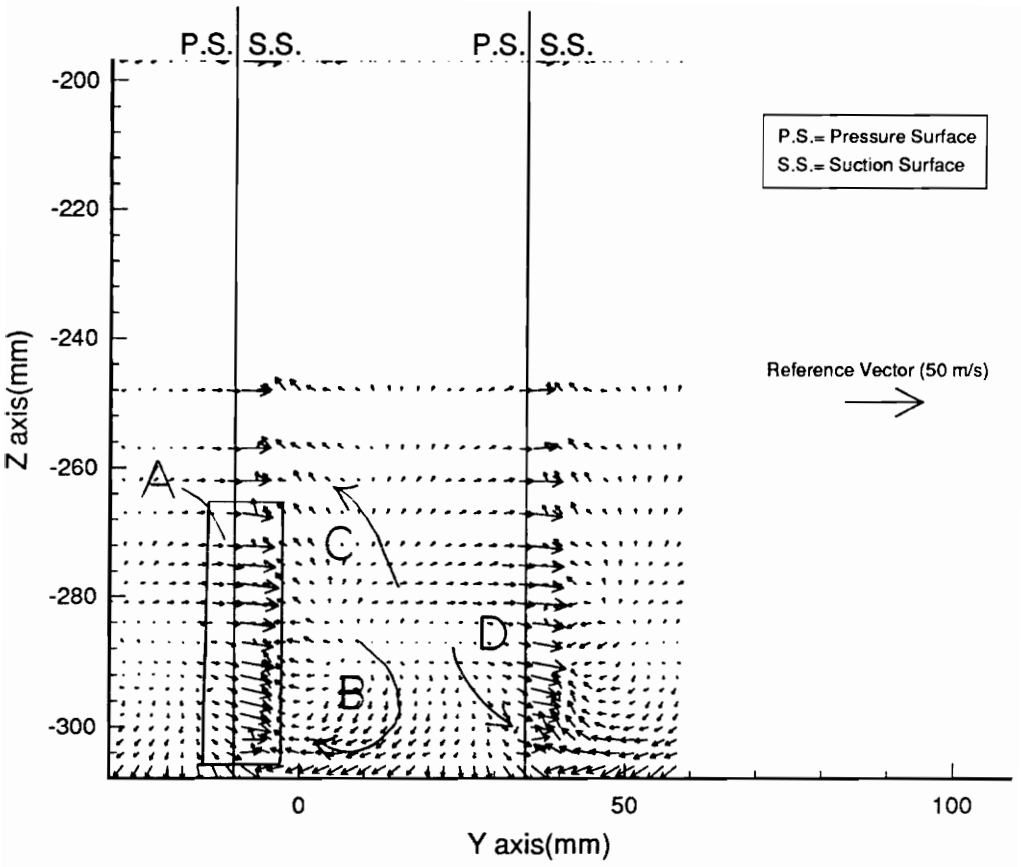

Figure 38. Downstream Secondary Flow Plot (No Blowing Condition)
$\alpha^* = 27°$, $V_1 = 48.13$ m/s, $Re_c = 174{,}144$

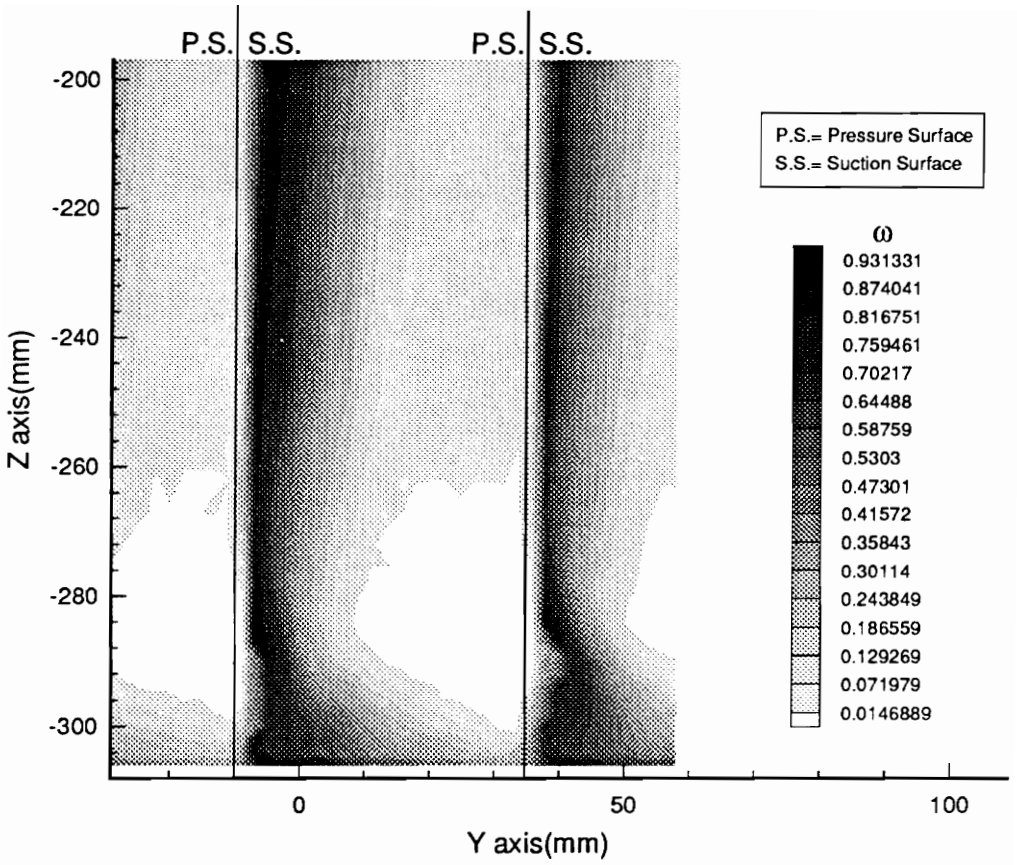

Figure 39. Downstream Loss Contour Plot (No Blowing Condition)
$\alpha^* = 27°$, $V_1 = 48.13$ m/s, $Re_c = 174{,}144$

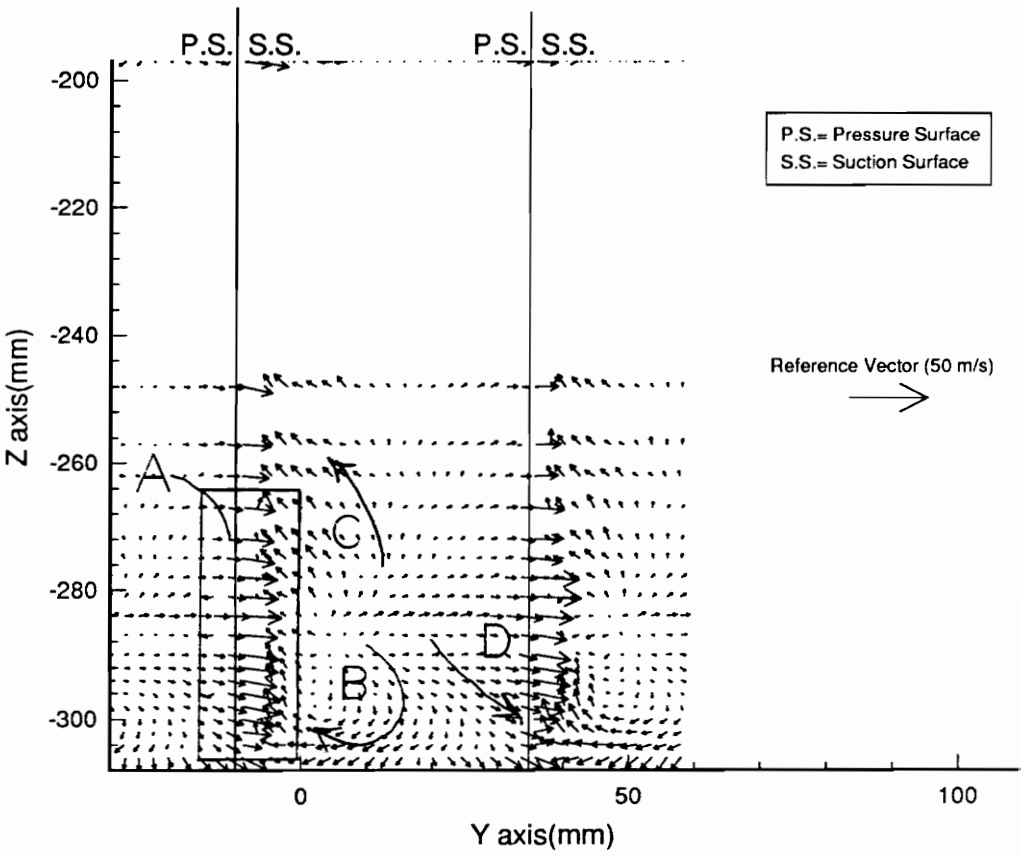

Figure 40. Downstream Secondary Flow Plot (No Blowing Condition)
$\alpha^* = 29°$, $V_1 = 48.85$ m/s, $Re_c = 177{,}808$

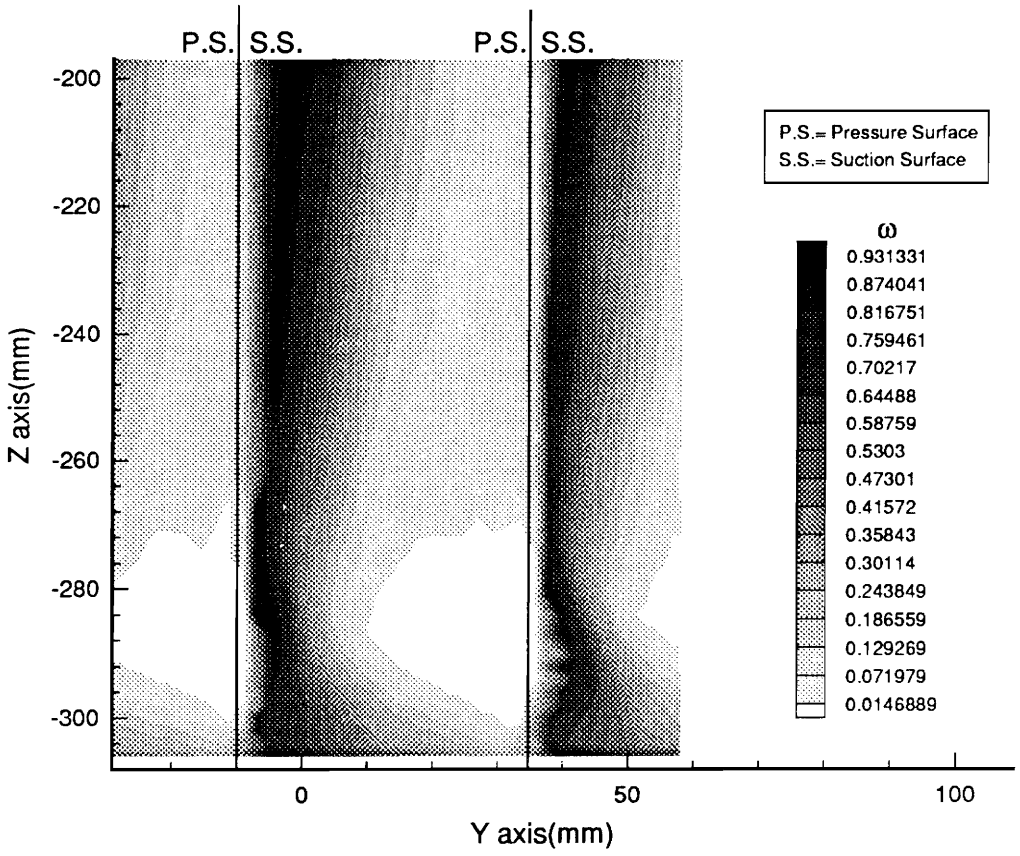

Figure 41. Downstream Loss Contour Plot (No Blowing Condition)
$\alpha^* = 29°$, $V_1 = 48.85$ m/s, $Re_c = 177{,}808$

pressure loss coefficient, ω, was calculated at each data point for the set of measurements described in Table 1. To generate the velocity vector plots, the mass averaged outlet angle defined by:

$$\overline{\alpha_2} = \frac{\iint_{passage} \alpha_2 \cdot V_{2x} \cdot \rho \cdot dy \cdot dz}{\iint_{passage} V_{2x} \cdot \rho \cdot dy \cdot dz}$$

with ρ assumed constant, was used to find a plane perpendicular to the main cascade outlet flow stream. This enabled the calculation of the secondary flow velocity components.

In region A of Fig. 24, the velocity vectors indicate fluid migration across the blade trailing edge, towards its pressure surface, and into the adjacent blade passage area. This indicates that significant corner flow separation has not begun for 5 degrees AoA. The loss contours in Fig. 25 support this conclusion since the total pressure losses in the corner region are relatively small. However, at 15 degrees AoA the velocity vectors in region A indicate the presence of fluid leakage into the corner region, indicating the onset of corner stall (Fig. 26). A significant growth of high losses in the corner region can be seen in the loss contour plot shown in Fig. 27, which supports this conclusion. In Fig. 28, at an AoA of 17 degrees the velocity vector patterns resemble those for the 15 degree AoA case. However, in region A of this figure increased fluid migration into the cascade corner region is apparent.

From the velocity vectors presented in Fig. 30, two distinct vortex structures are visible in the cascade corner region. In the junction formed by the cascade sidewall and blade suction surface (region B) a single vortex structure, rotating in a clockwise direction, is present. On the other side of region B (region C) another vortex structure, rotating in an opposite direction to that of the vortex in region B, is visible. This counter - clockwise rotating vortex structure appears to be part of the migration of fluid along the blade span into its midspan region. The loss contours for 19 degrees AoA, shown in Fig. 31, indicate higher losses due to increased corner stall, with the core of the high loss area located in the junction formed by the cascade sidewall and blade suction surface. The vortex structures appear more pronounced at 21 degrees AoA, as does the leakage flow highlighted in region A (Fig. 32).

At an AoA of 23 degrees, the core of the high loss area does not appear to have increased significantly (Fig. 35). In region D shown in Fig. 34, an additional flow structure can be seen channeling migratory fluid into the corner region of the adjacent blade passage. The same description can be applied to the fluid flow characteristics in region D of Fig. 36, which corresponds to 25 degrees AoA. Additionally, the core of the high loss area in the corner region has grown significantly, along with the losses along the rest of the blade span (Fig. 37).

In Fig. 37, a noticeable lack of high loss development between z = -276mm and z = -288mm is clearly shown for 25 degrees AoA. This is believed to be a result of fluid acceleration around the corner stall blockage causing the boundary layer flow in this area to gain momentum, thus enabling it to better avoid separating in the face of an adverse pressure gradient.

At 27 degrees AoA, the vortex structure in region C appears more as a mechanism for spanwise fluid migration (Fig. 38). This can probably be attributed to the profile boundary layer being separated for a significant portion of the blade chord length. As a result, the stalled corner flow is better able to migrate into the stalled blade midspan region. The loss contours of Figures 39 and 41, which correspond to 27 and 29 degrees AoA, respectively, indicate that the losses in the blade wake, outside of the corner region, have continued to increase, growing to encompass a larger portion of the blade passage area. From looking at these two sets of loss contour plots, the lack of significant loss development between z = -276mm and z = -288mm is still evident. Also, the losses in the corner region at these two AoA settings do not appear to have increased significantly. The velocity vectors shown in Fig. 40 indicate that the vortex structure in region B remains as the only rotating fluid flow mechanism in the corner region. The fluid in regions A, C, and D appear only as mechanisms for channeling stalled fluid into adjacent blade passage areas.

3.3 Downstream Measurements with Boundary Layer Blowing

Table 3 shows a set of values for the volumetric flow rate of air supplied at each of the blade slots as a percentage of the volumetric flow rate of the blade passage area, Q_{psg}, immediately above the slot. The results show that the required blade slot jet air volumetric flow rate, Qsb, was a very small fraction of the involved cascade volumetric flow rate. The Qsb values shown in Table 3 are average values, rounded to whole numbers, based on the Qsb values shown in Table 2, and correspond to each of the three blade slot volumetric flow rates used for the boundary layer blowing experiments. These average Qsb values are referenced during the discussion of the corner region boundary layer blowing results in sections 3.3.1 and 3.3.2.

Table 3. Blade Slot Volumetric Flow Rate Percentages

Qsb	(Qsb / Qpsg) x 100
9 Li/min	.3%
21 Li/min	.7%
26 Li/min	.9%
*Qpsg = 3,064 Li/min	

3.3.1 Pitchwise Mass - Averaged Loss Coefficient Results

A numerical integration procedure was used to find the pitchwise mass - averaged loss coefficient values along the blade span using the relation:

$$\overline{\omega}_2(z) = \frac{\int_0^1 \rho \cdot \omega \cdot V_{2x} \cdot d(\frac{y}{s})}{\int_0^1 \rho \cdot V_{2x} \cdot d(\frac{y}{s})}$$

with ρ assumed constant. This allowed the mass - averaged influence of boundary layer blowing on the cascade total pressure losses to be observed. In the resulting set of figures, boundary layer blowing with and without the external blade slot flap are represented. It is recognized that the definition of the loss coefficient, ω, does not take into account the injection of additional mass flow into the free stream flow. The upstream total pressure of the free stream flow, P_{t1}, serves as the reference by which total pressure losses downstream of the cascade are measured. Therefore, the resulting pitchwise mass - averaged loss coefficient plots were viewed more as a means of determining the success of the jet in making up the total pressure lost in the corner region, due to boundary layer separation. Since momentum was being added by the jet air slots, negative loss coefficients were calculated in some regions along the blade span.

3.3.1.1 Blade Slots Without External Flap

Figures 42 through 45 illustrate the effects of boundary layer blowing on the cascade pitchwise mass - averaged loss coefficient profiles at 19 and 21 degrees angle of attack. At each angle of attack, blade slot volumetric flow rates of 21 and 26 Li/min were used, which correspond to jet to free stream velocity ratios of roughly 1.56 and 1.94, respectively, as shown in Table 2. The main

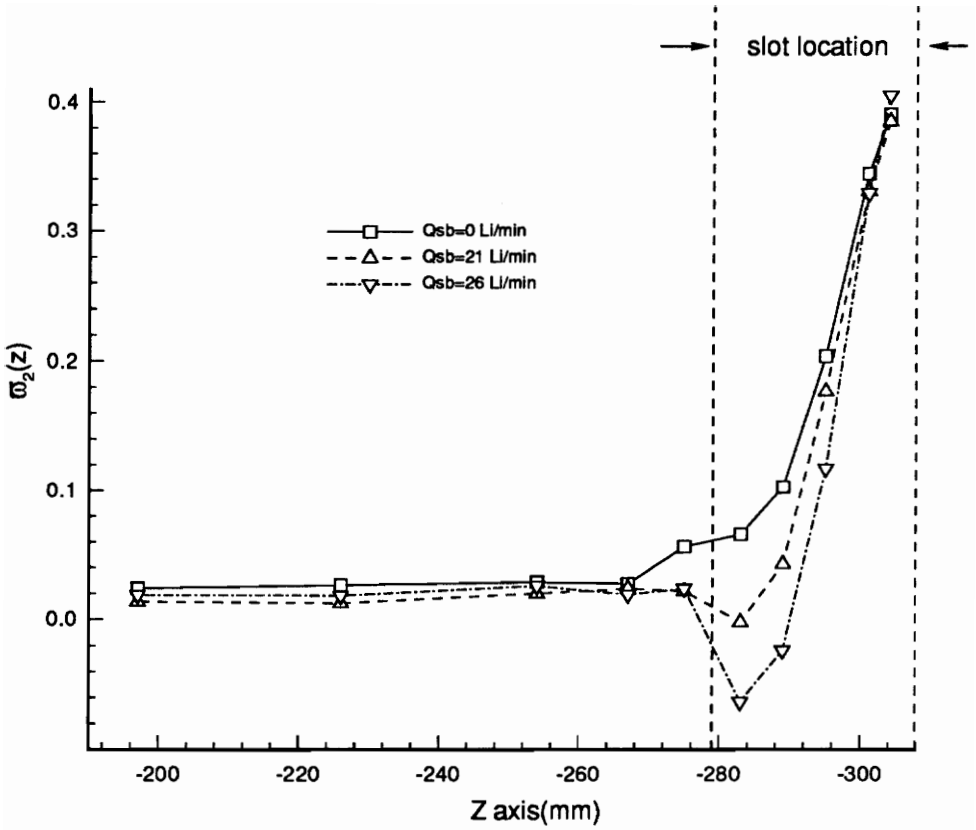

Figure 42. Pitchwise Mass - Averaged Loss Coefficient Results for Corner Boundary Layer Blowing with Blade Slot Number One (without external flap), $\alpha^* = 19°$

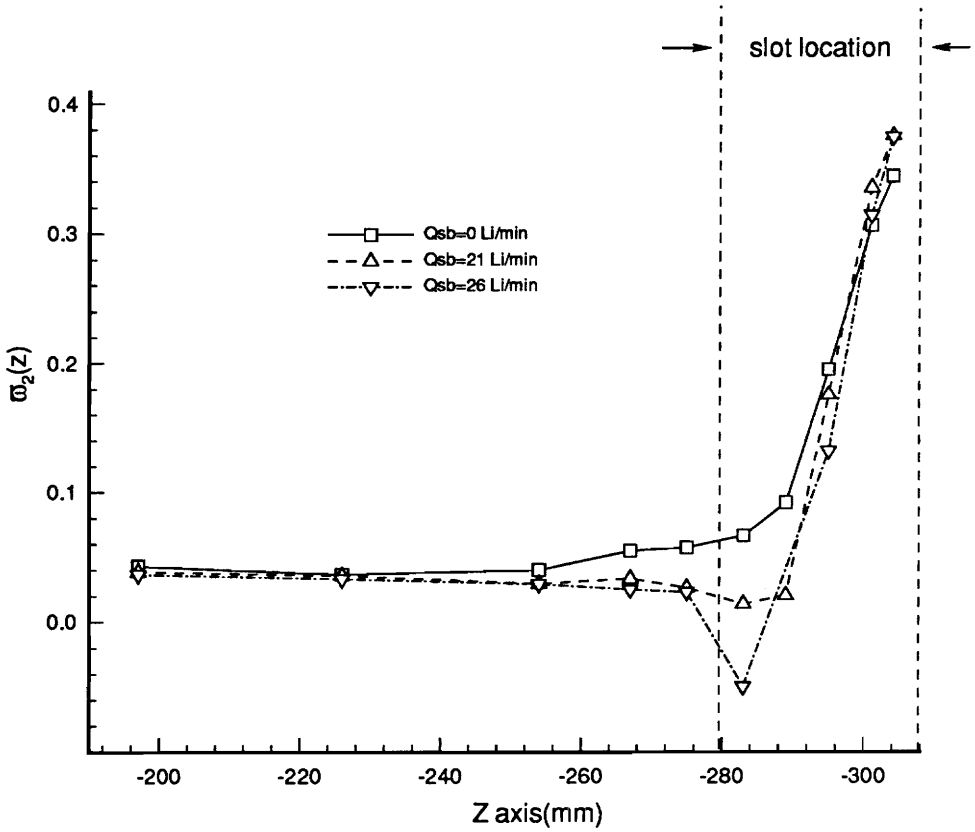

Figure 43. Pitchwise Mass - Averaged Loss Coefficient Results for Corner Boundary Layer Blowing with Blade Slot Number One (without external flap), $\alpha^* = 21°$

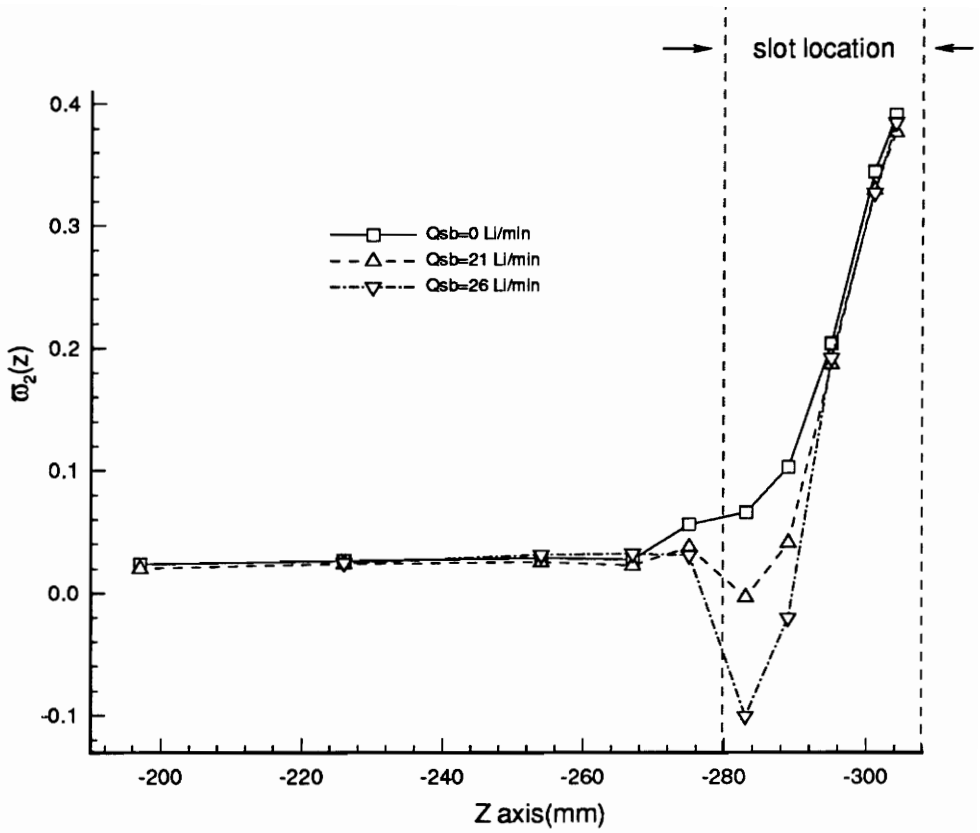

Figure 44. Pitchwise Mass - Averaged Loss Coefficient Results for Corner Boundary Layer Blowing with Blade Slot Number Two (without external flap), $\alpha^* = 19°$

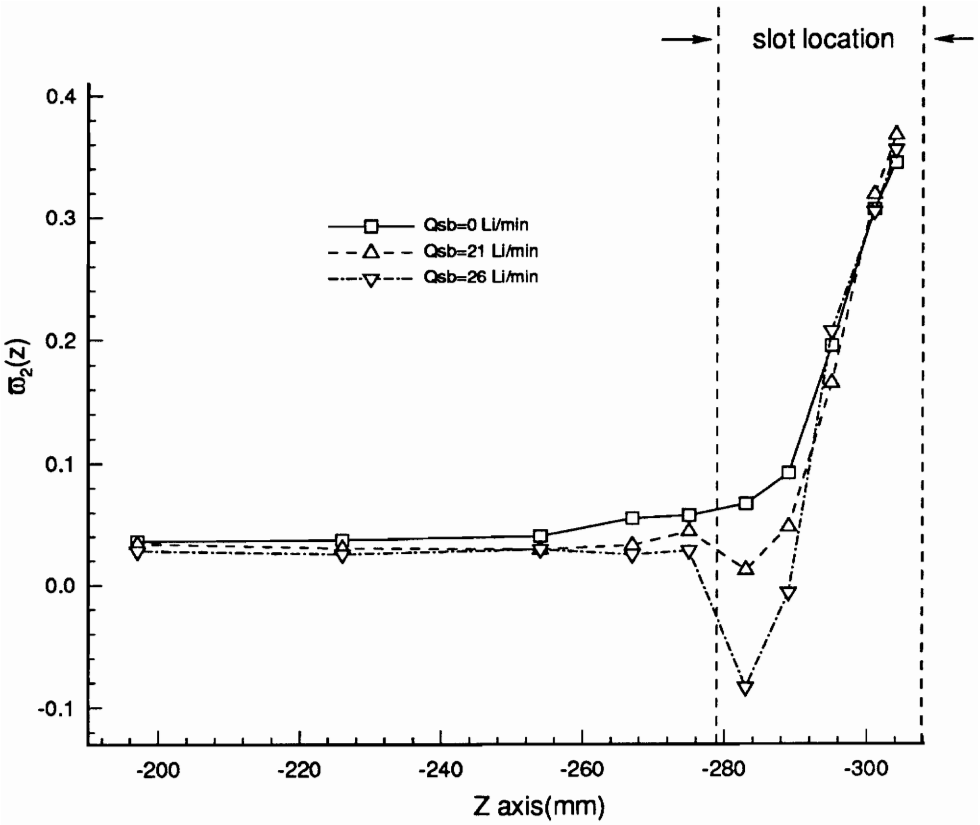

Figure 45. Pitchwise Mass - Averaged Loss Coefficient Results for Corner Boundary Layer Blowing with Blade Slot Number Two (without external flap), $\alpha^* = 21°$

result of boundary layer blowing without an external blade slot flap was a significant reduction in the magnitude of $\varpi_2(z)$ in the region between z = -274mm and z = -294mm. In this region, the largest decreases in $\varpi_2(z)$ occurred at the blade slot volumetric flow rate (Qsb) setting of 26 Li/min and was centered at a spanwise location of z = -284mm. As shown in Fig. 42 which corresponds to 19 degrees AoA, boundary layer blowing with blade slot number one caused the pitchwise mass - averaged loss coefficient profile to reach a minimum value of -0.07 at z = -283mm for the blade slot volumetric flow rate setting of 26 Li/min. When Qsb was reduced to 21 Li/min, the blade pitchwise mass - averaged loss coefficient profile reached a minimum value of -0.01 at the same location. In Fig. 43, at an AoA of 21 degrees the minimum value of each of the pitchwise mass - averaged loss coefficient profiles, for each Qsb setting, occurred at the same spanwise location as that for 19 degree AoA. The results presented in Figures 44 and 45, which correspond to boundary layer blowing with blade slot number two, closely followed the $\varpi_2(z)$ profiles for blade slot number one. Only a slight decrease (became more negative) in the minimum values of the $\varpi_2(z)$ profiles was observed for both 19 and 21 degrees AoA at each Qsb setting. From looking at the results shown in Figures 42 through 45, the appearance of negative values of $\varpi_2(z)$ between z = -274mm and z = -288mm indicates that enough total pressure is being added by the jet air flow from the blade slot to make up for the total pressure losses caused by the corner stall.

The change in the values of $\varpi_2(z)$, relative to values obtained for no corner boundary layer blowing, are presented in Figures 46 and 47 using the following relation:

$$\Delta\overline{\omega}_2(z) = \overline{\omega}_2(z)_{no\ blowing} - \overline{\omega}_2(z)_{blowing}$$

As shown in Fig. 46, the majority of the large decreases in $\varpi_2(z)$ (appearing in the figure as increased, positive values of $\Delta\varpi_2(z)$) centers around z = -284mm. In the region closest to the cascade sidewall, from z = -300mm and z = -308mm, no significant change in $\varpi_2(z)$ resulted. Outside the region between z = -274mm and z = -294mm, towards the blade midspan region, the effects of boundary layer blowing tapered off. The results presented In Fig. 47, which correspond to boundary layer blowing with blade slot two, followed the results shown in Fig. 46. In this figure, the values for $\Delta\varpi_2(z)$ centered around zero outside the region between z = -274mm and z = -294mm and increased significantly inside this region.

The results shown in Figures 42 through 47 indicate that the major zone of influence on the values of $\varpi_2(z)$ for corner boundary layer blowing without the external blade slot flap is the region between z = -274mm and z = -294mm. From viewing the loss contour plots shown in Figures 31 and 33, which correspond to 19 and 21 degrees AoA, respectively, this is the area along the blade span where transition from corner stall to two - dimensional blade stall is

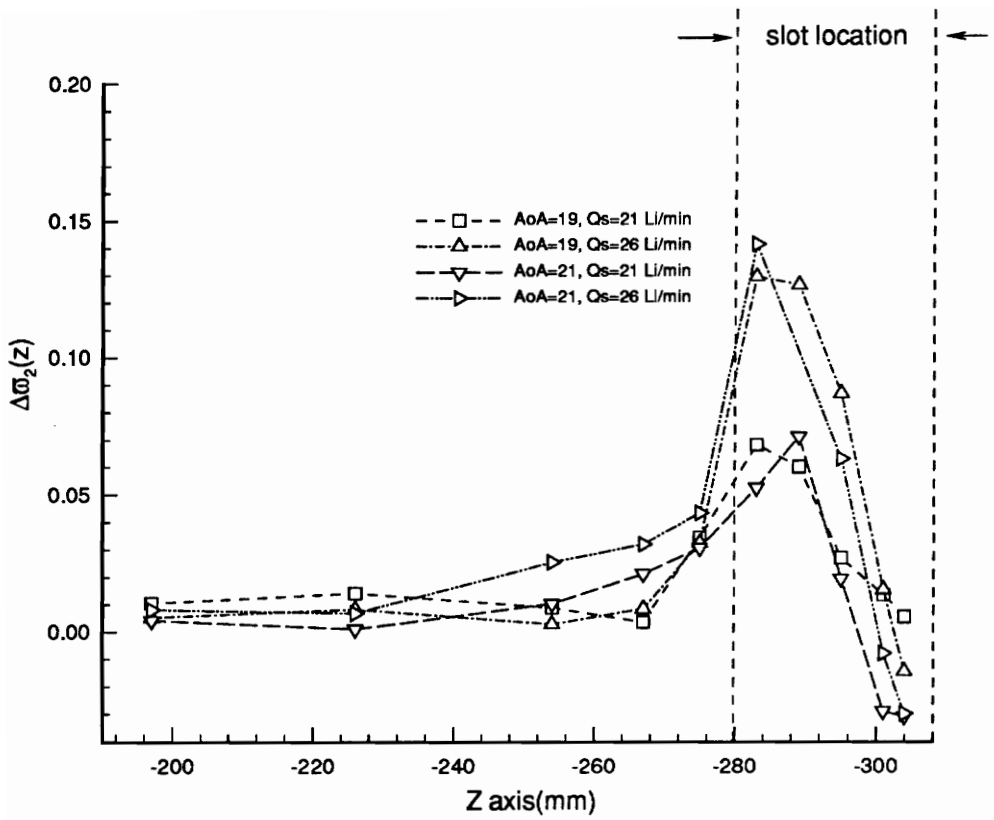

Figure 46. Relative Difference in Pitchwise Mass - Averaged Loss Coefficient Results for Corner Boundary Layer Blowing with Blade Slot Number One (without external flap)

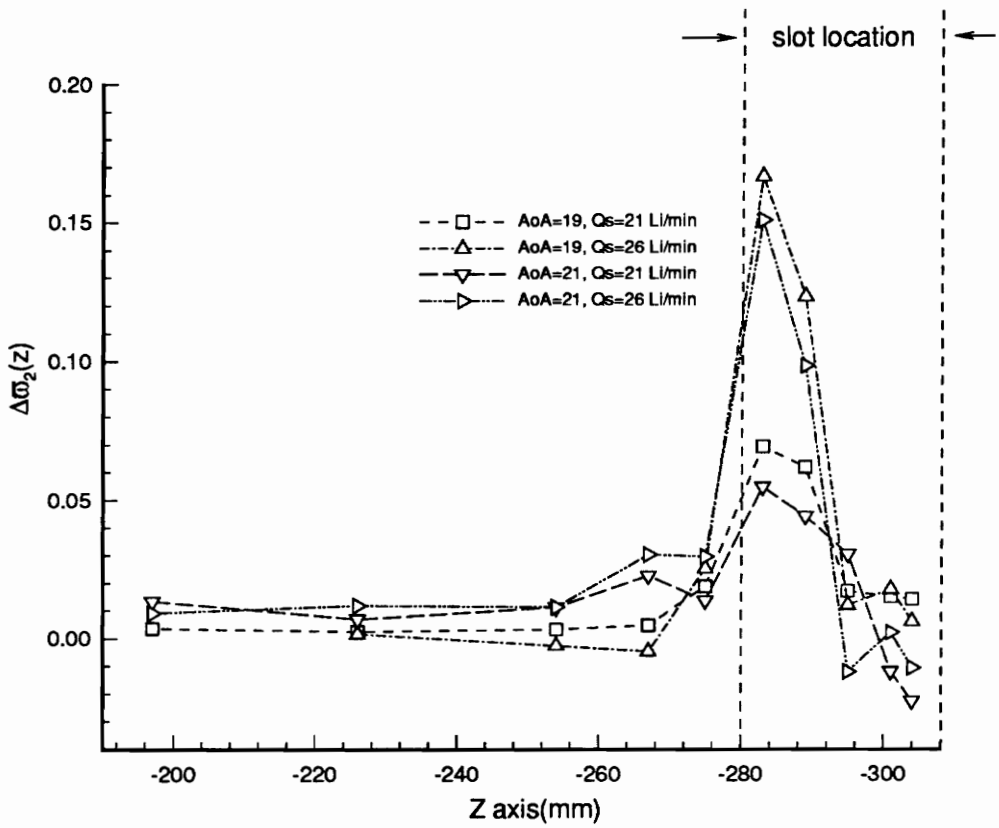

Figure 47. Relative Difference in Pitchwise Mass - Averaged Loss Coefficient Results for Corner Boundary Layer Blowing with Blade Slot Number Two (without external flap)

believed to occur. Since the effects of the corner stall appear to increase as the cascade sidewall is approached, the boundary layer in this transitional region is thinner and may be more susceptible to momentum addition by jet air flow from the blade slot. Additionally, the jet air flow may even be deflected around a large area of the unaffected corner stall, increasing the blade slot effectiveness in this region.

3.3.1.2 Blade Slots With External Flap

The results presented in Figures 48 through 53 indicate that boundary layer blowing with the blade slot flap in place results in much smaller decreases in pitchwise mass - averaged loss coefficient values, compared to the results in section 3.3.1.1. For this blade slot configuration, the greatest decrease in values of $\varpi_2(z)$ occurred in the region between z = -260mm and z = -288mm.

Figures 48 through 50 show the results of boundary layer blowing with blade slot number one on the pitchwise mass - averaged loss coefficient profiles for 19, 21, and 23 degrees AoA. At 19 degrees AoA, the only significant decrease in the value of $\varpi_2(z)$ occurred between z = -268mm and z = -284mm at a Qsb setting of 21 Li/min (Fig. 48). From looking at the $\varpi_2(z)$ profiles shown in Figures 49 and 50, all three Qsb settings used at each AoA were somewhat effective in decreasing the total pressure losses in this region. However, a pattern of increased values of the blade slot volumetric flow rate resulting in proportionally decreasing $\varpi_2(z)$ values could not be established from viewing the

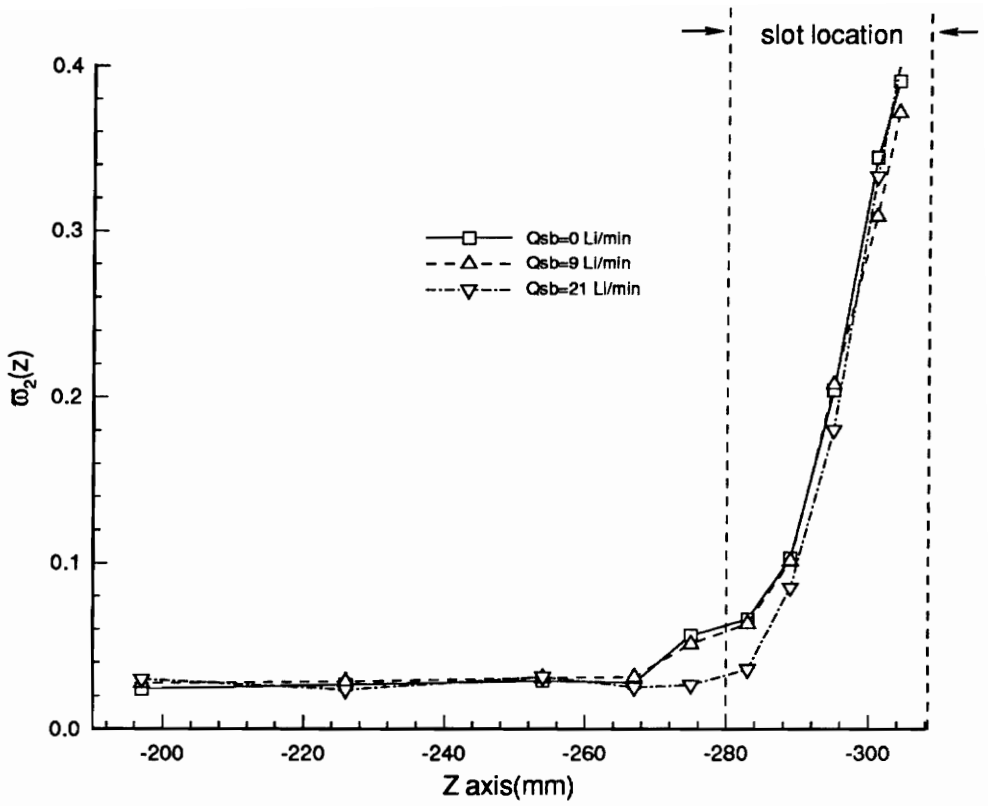

Figure 48. Pitchwise Mass - Averaged Loss Coefficient Results for Corner Boundary Layer Blowing with Blade Slot Number One (with external flap), $\alpha^* = 19°$

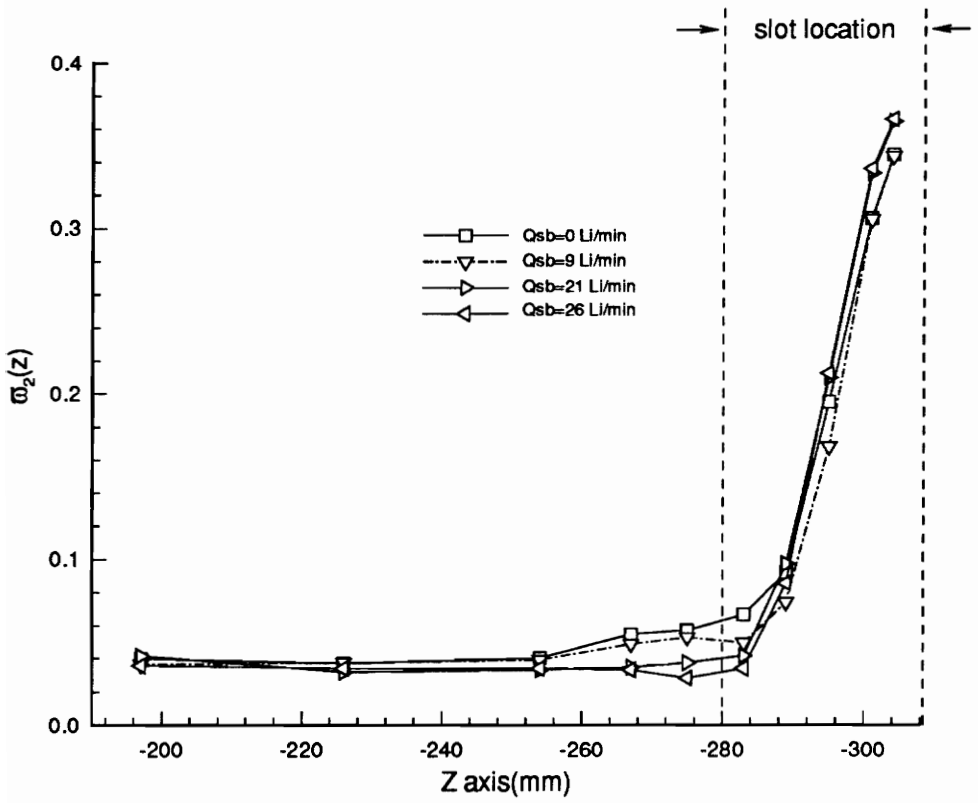

Figure 49. Pitchwise Mass - Averaged Loss Coefficient Results for Corner Boundary Layer Blowing with Blade Slot Number One (with external flap), $\alpha^* = 21°$

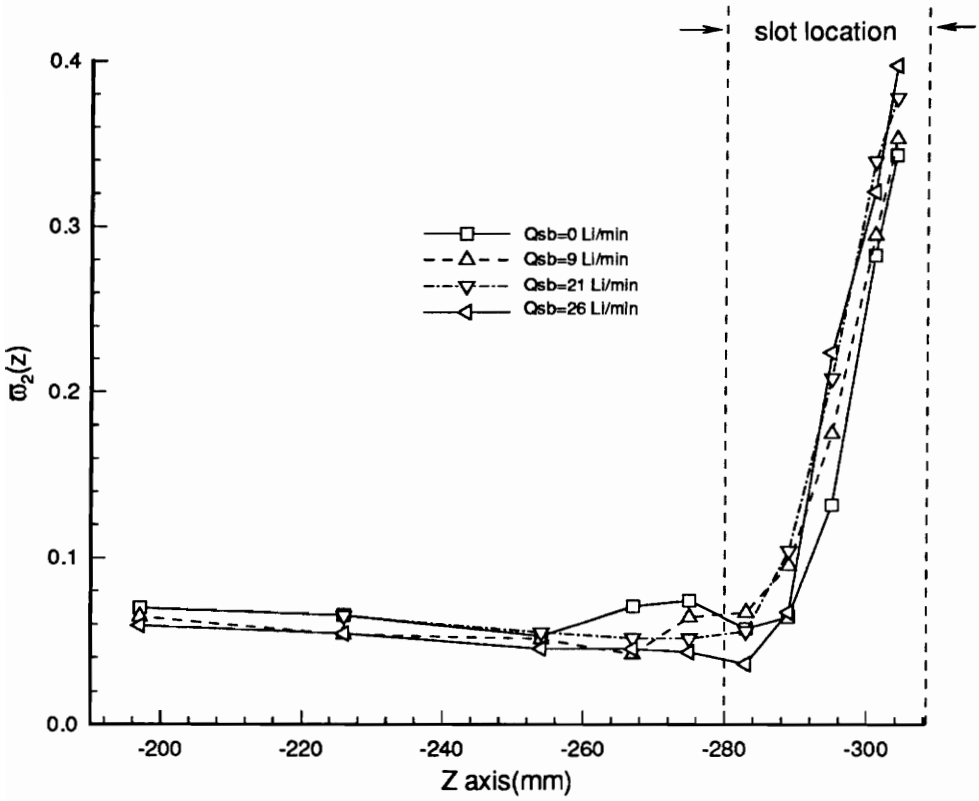

Figure 50. Pitchwise Mass - Averaged Loss Coefficient Results for Corner Boundary Layer Blowing with Blade Slot Number One (with external flap), $\alpha^* = 23°$

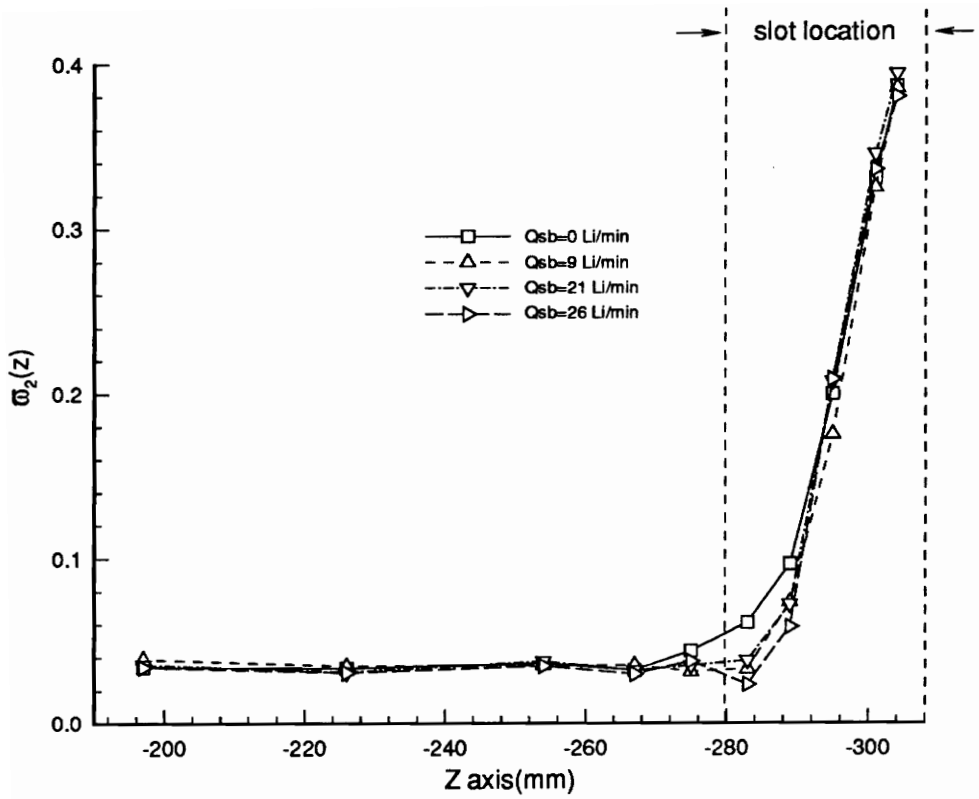

Figure 51. Pitchwise Mass - Averaged Loss Coefficient Results for Corner Boundary Layer Blowing with Blade Slot Number Two (with external flap), $\alpha^* = 19°$

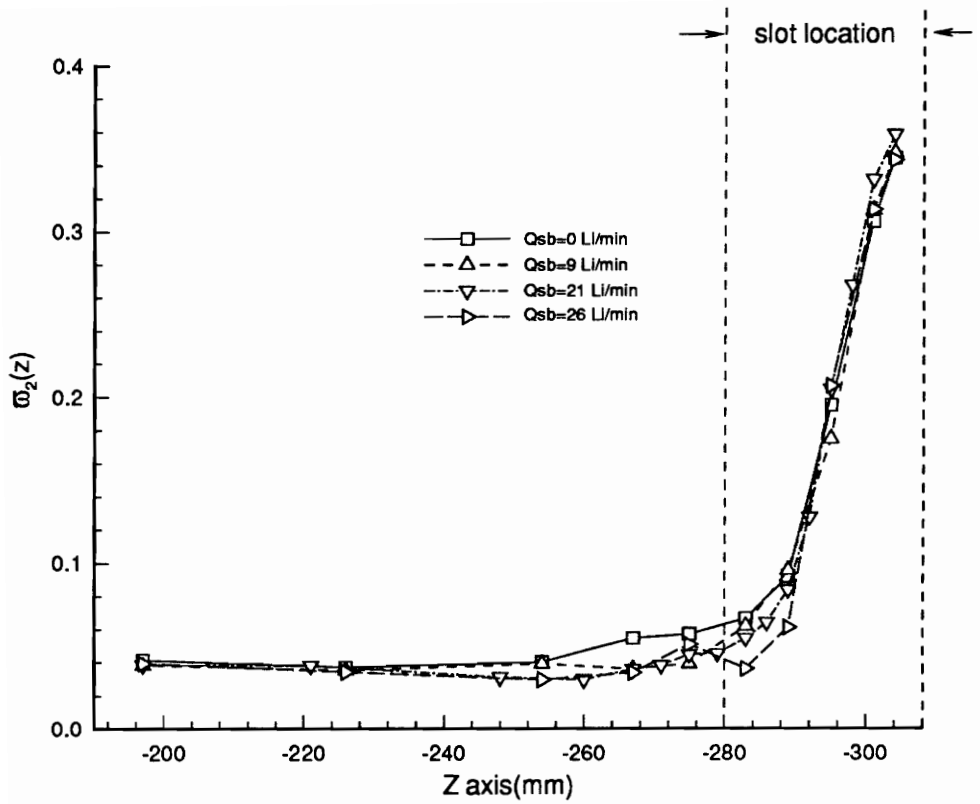

Figure 52. Pitchwise Mass - Averaged Loss Coefficient Results for Corner Boundary Layer Blowing with Blade Slot Number Two (with external flap), $\alpha^* = 21°$

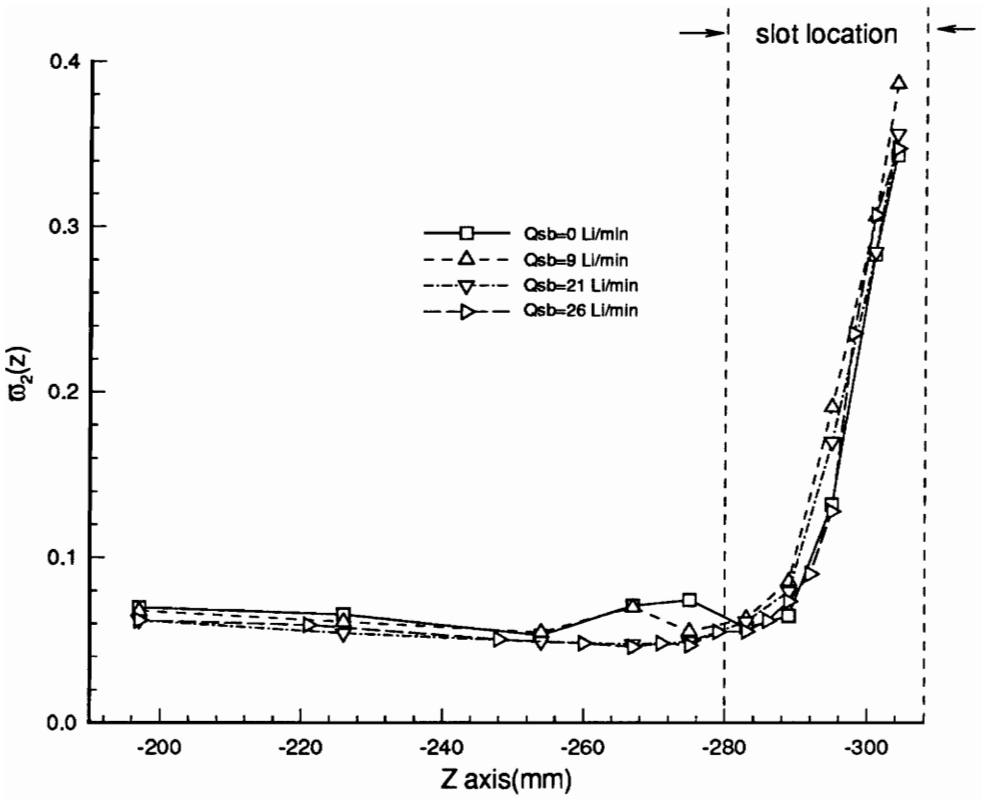

Figure 53. Pitchwise Mass - Averaged Loss Coefficient Results for Corner Boundary Layer Blowing with Blade Slot Number Two (with external flap), $\alpha^* = 23°$

results. At 23 degrees AoA, along with a decrease in the values of $\varpi_2(z)$ between z = -268mm and z = -284mm, the values of $\varpi_2(z)$ increased in the region where the blade slot is located (Fig. 50). Figures 51 through 53 show the effects of boundary layer blowing with blade slot two on the $\varpi_2(z)$ versus z profiles for 19, 21, and 23 degrees angle of attack. In comparison to the results for boundary layer blowing with blade slot one, no significant difference between the two sets of pitchwise mass - averaged loss coefficient profiles could be observed.

The reason for the smaller region of affected blade corner stall, in comparison to the results for corner boundary layer blowing without the external blade slot flap, is believed to be due to the jet air flow being confined to a smaller initial area of injection into the corner stall region over the blade suction surface. With the blade slot flap in place, the jet air flow is forced to follow the curvature of the blade more closely, confining its effects to a smaller percentage of the corner region, blade passage area.

3.3.2 Loss Contour Plot Results

A series of loss contour plots were created in order to evaluate the changes in the total pressure loss coefficient values due to corner boundary layer blowing in the cascade central blade passage area. Figures 54 through 61 correspond to boundary layer blowing at 19 and 21 degrees AoA, without the

use of blade slot flaps. Figures 62 through 69 are the loss contour plots for 21 and 23 degrees AoA, with the external blade slot flaps in place. The resulting figures support the conclusions reached in section 3.3.1 for the pitchwise mass - averaged loss coefficient plots.

In each of the two groups of figures there are two figures for each combination of angle of attack and blade slot volumetric flow rate; one which gives an overview of the losses for the full range of downstream measurements taken over the blade passage area, and one which shows a close - up view of the effects of boundary layer blowing in the corner region. Both groups of figures correspond to boundary layer blowing with blade slot number one at Qsb settings of 21 and 26 Li/min. All of the figures are presented with the same contour leveling so that the results can be compared visually. The results for corner boundary layer blowing with blade slot two were very similar to the loss contour plots presented in Figures 54 through 69 and will not be discussed.

3.3.2.1 Blade Slot One Without External Flap

The loss contours in Figures 54 through 61 indicate that the most significant decrease in the values of ω occur in the region immediately adjacent to the core of the high loss corner stall fluid. In this region (region A), a substantial decrease in total pressure loss values occurs as Qsb is increased from 21 to 26 Li/min. This is evident for both 19 and 21 degrees AoA. At 19

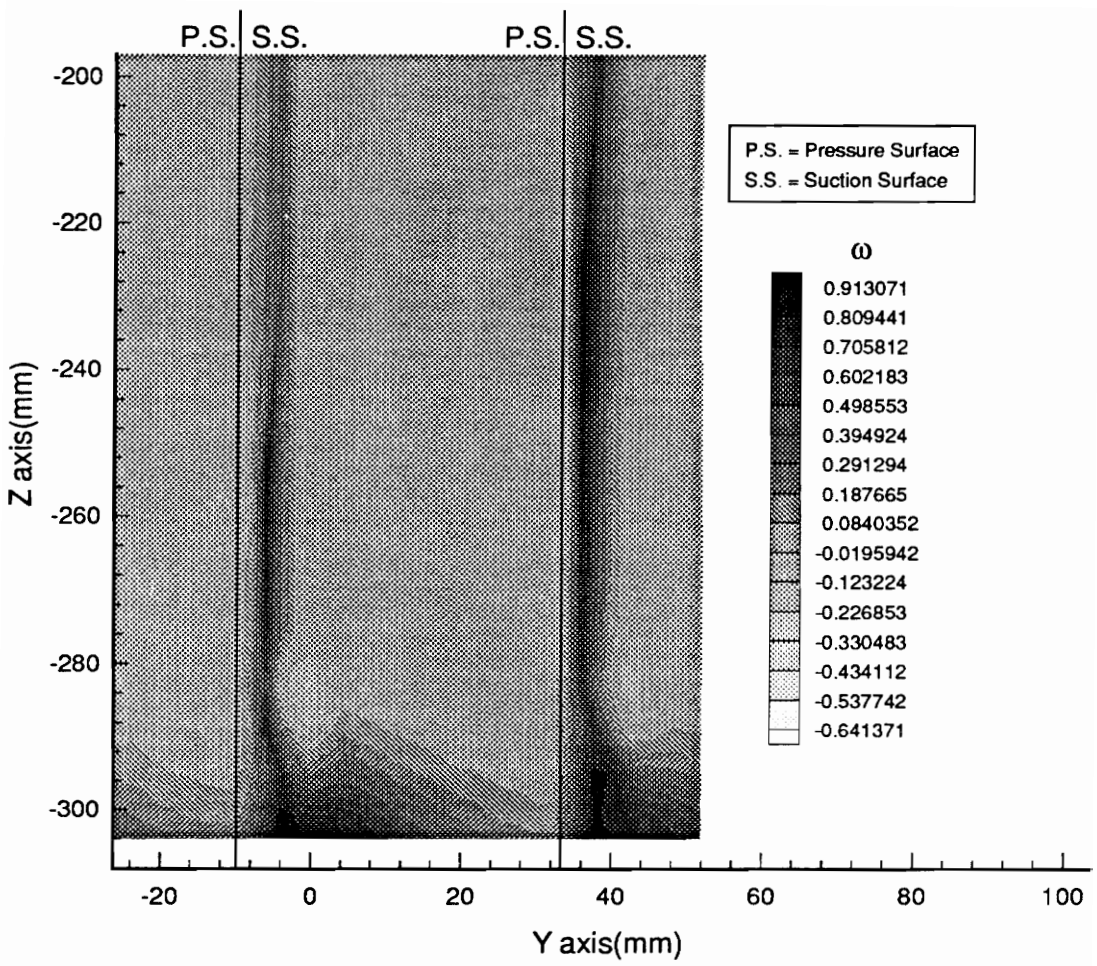

Figure 54. Downstream Loss Contours for Corner Boundary Layer Blowing with Blade Slot Number One (without external flap), $\alpha^* = 19$, Qsb = 21 Li/min, $V_1 = 47.38$ m/s, $Re_c = 170{,}837$

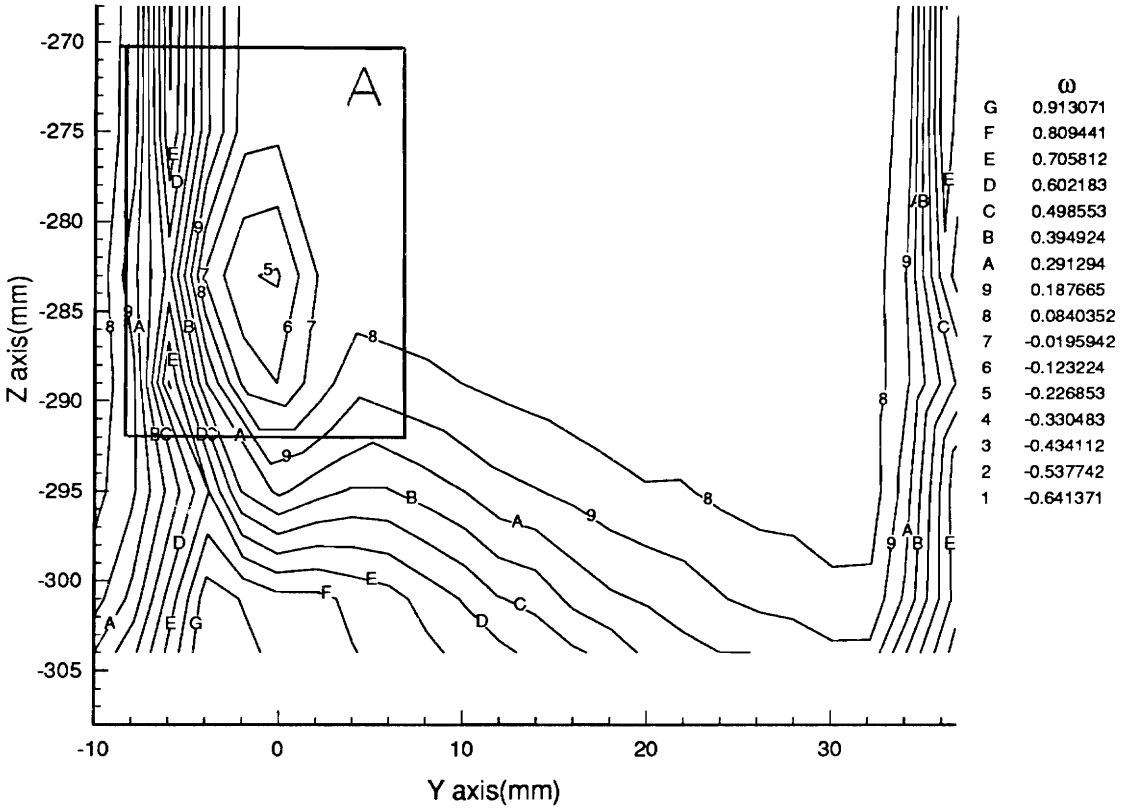

Figure 55. Close Up View of the Blade Passage, Corner Region Loss Contours of Fig. 54, $\alpha^* = 19$, Qsb = 21 Li/min, $V_1 = 47.38$ m/s, $Re_c = 170{,}837$

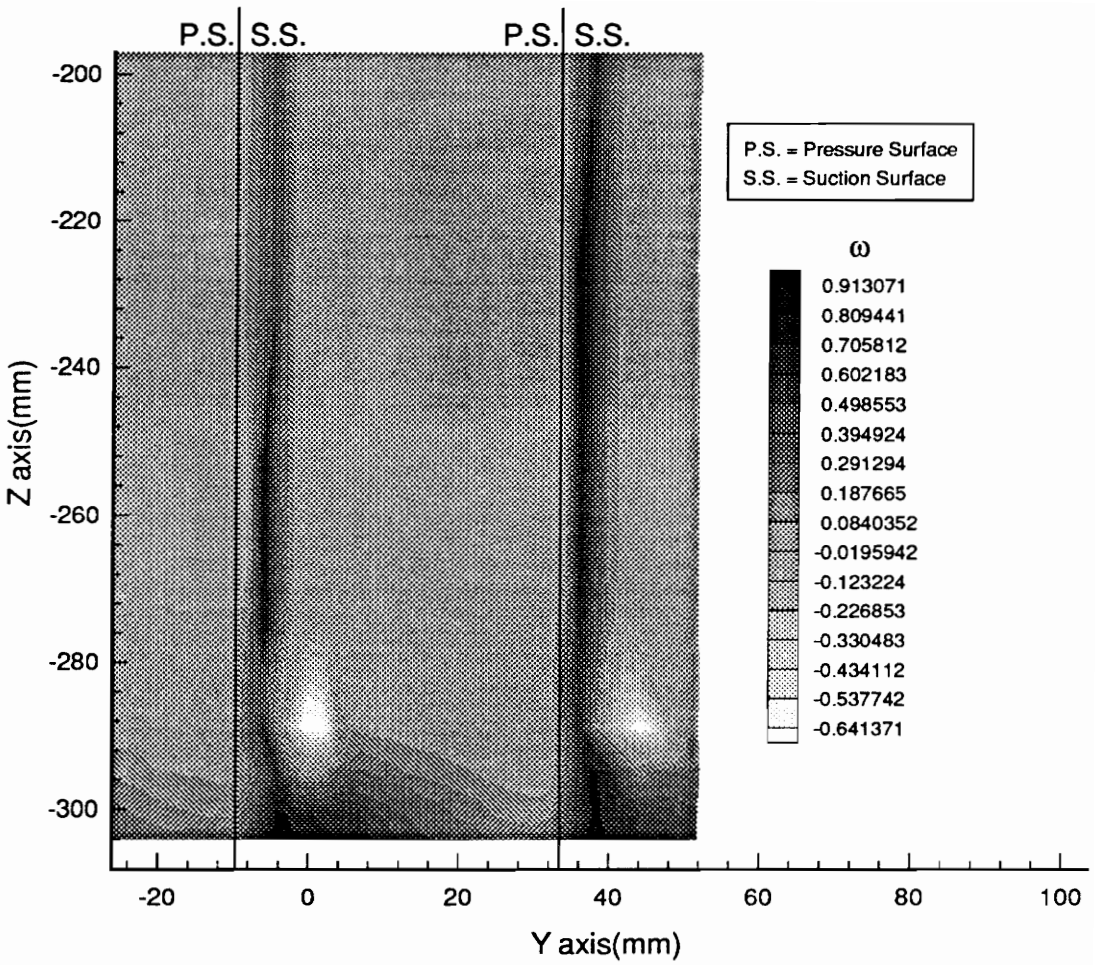

Figure 56. Downstream Loss Contours for Corner Boundary Layer Blowing with Blade Slot Number One (without external flap),
α^* = 19, Qsb = 26 Li/min, V_1 = 47.59 m/s, Re_c = 169,514

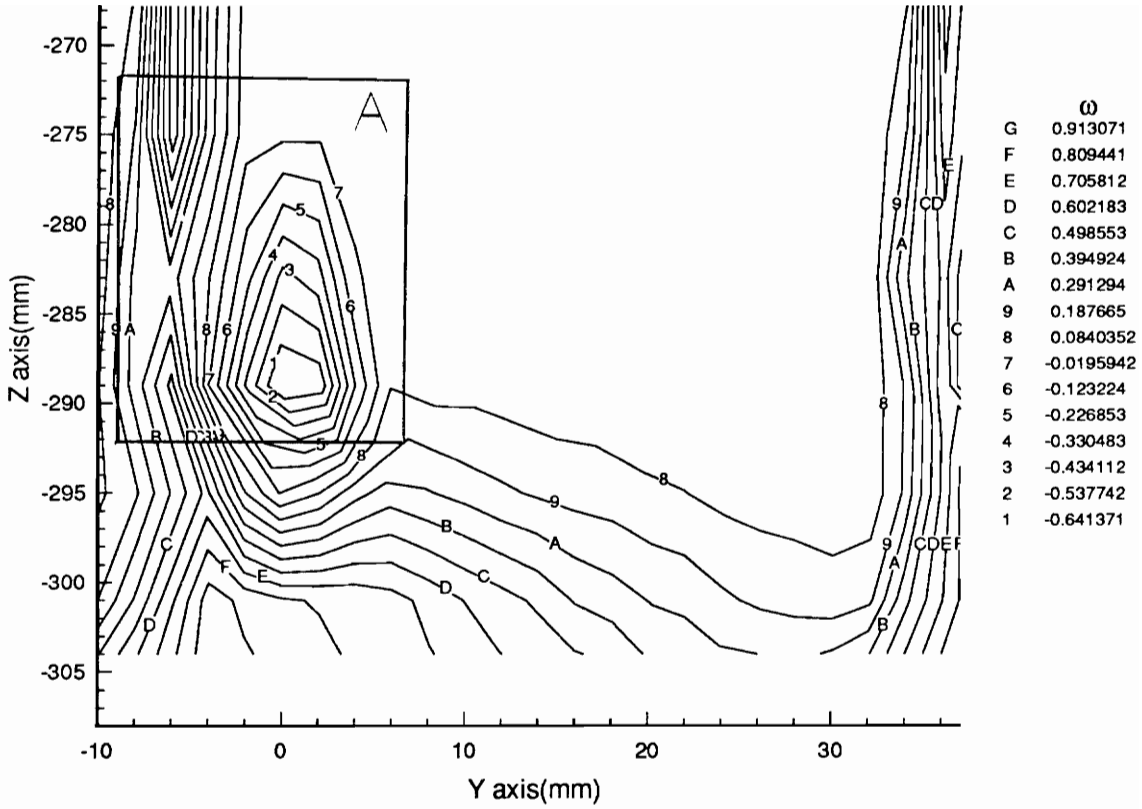

Figure 57. Close Up View of the Blade Passage, Corner Region Loss Contours of Fig. 56, $\alpha^* = 19$, Qsb = 26 Li/min, $V_t = 47.59$ m/s, $Re_c = 169{,}514$

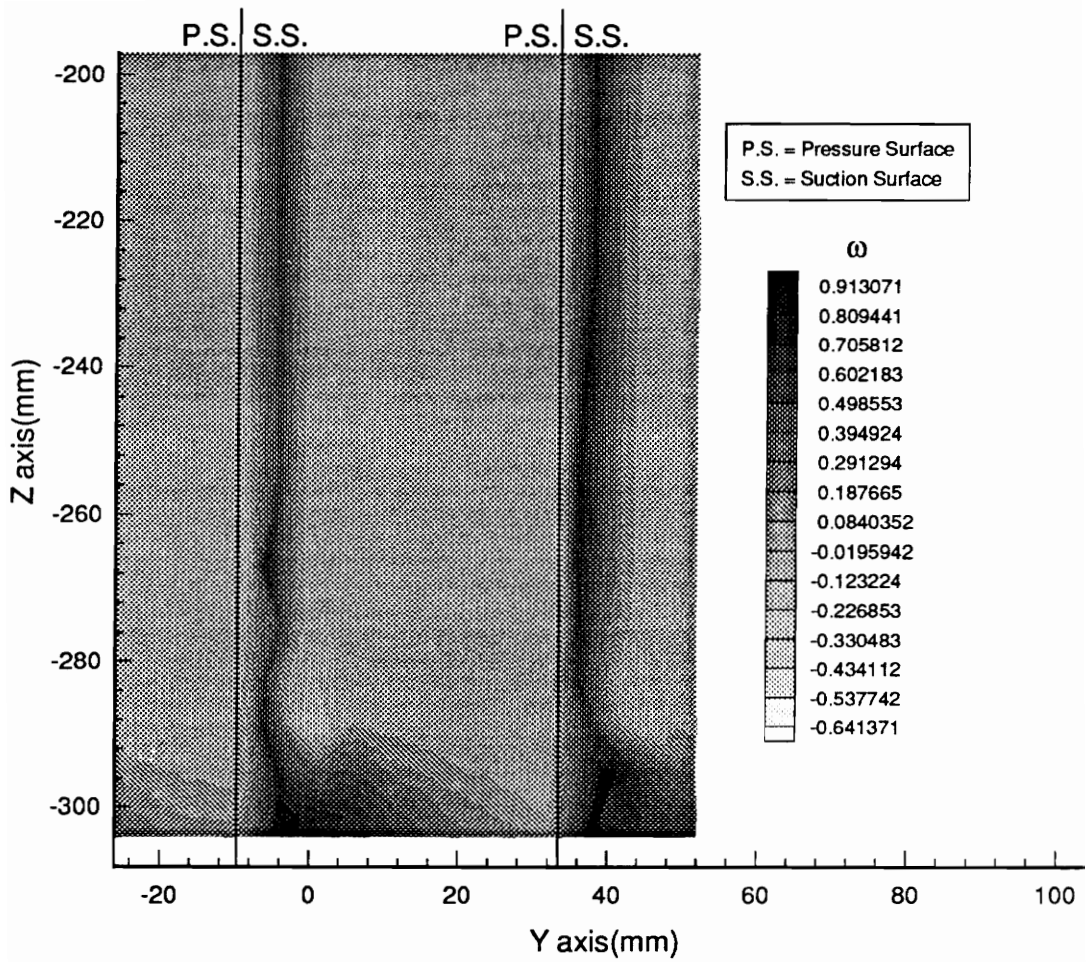

Figure 58. Downstream Loss Contours for Corner Boundary Layer Blowing with Blade Slot Number One (without external flap), $\alpha^* = 21$, Qsb = 21 Li/min, $V_1 = 47.11$ m/s, $Re_c = 170,146$

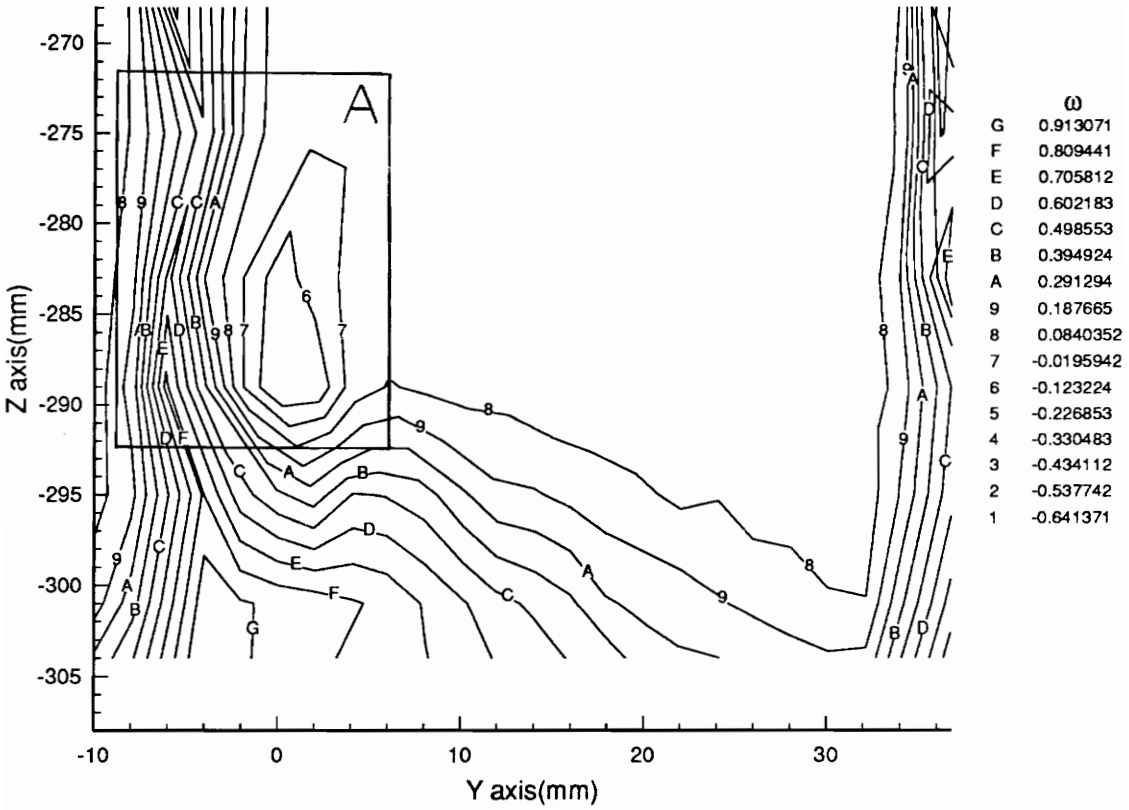

Figure 59. Close Up View of the Blade Passage, Corner Region Loss Contours of Fig. 58, $\alpha^* = 21$, Qsb = 21 Li/min, $V_1 = 47.11$ m/s, $Re_c = 170,146$

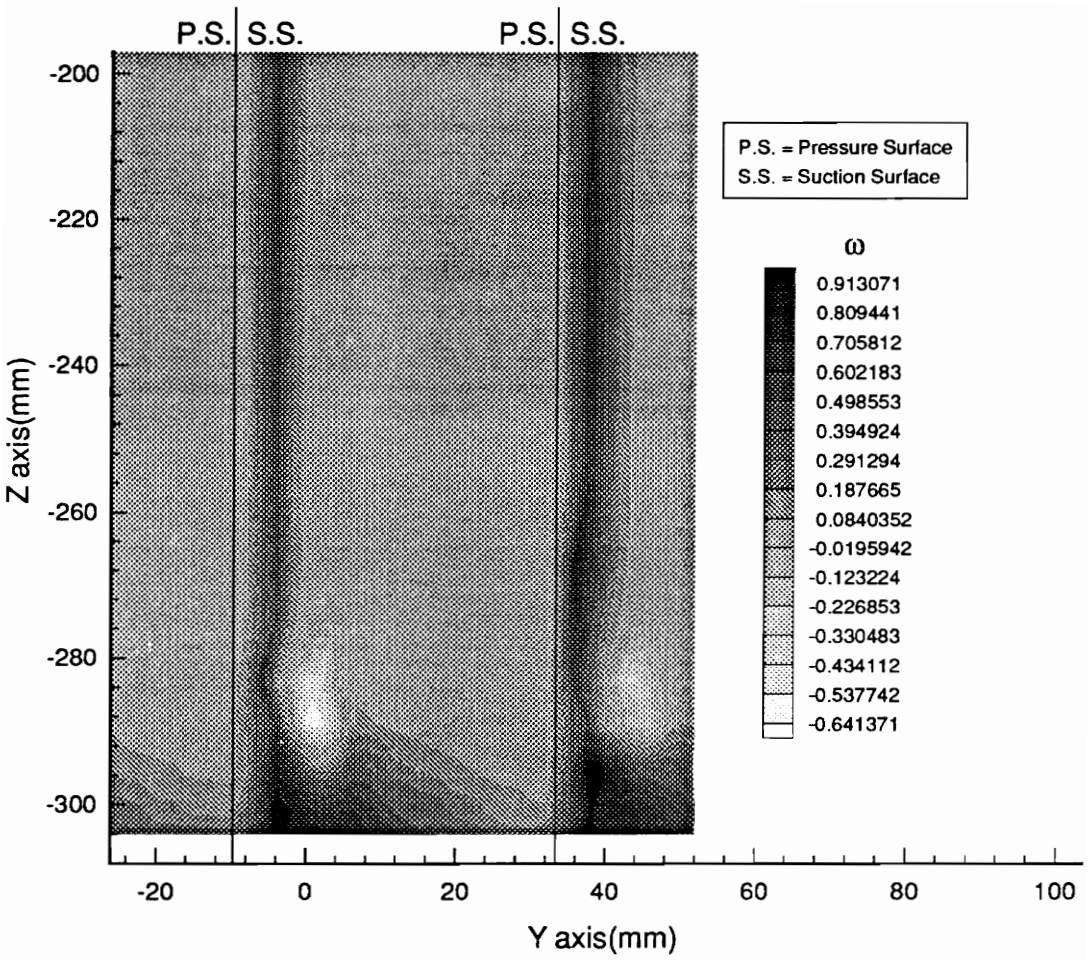

Figure 60. Downstream Loss Contours for Corner Boundary Layer Blowing with Blade Slot Number One (without external flap), $\alpha^* = 21$, Qsb = 26 Li/min, $V_1 = 47.53$ m/s, $Re_c = 172{,}223$

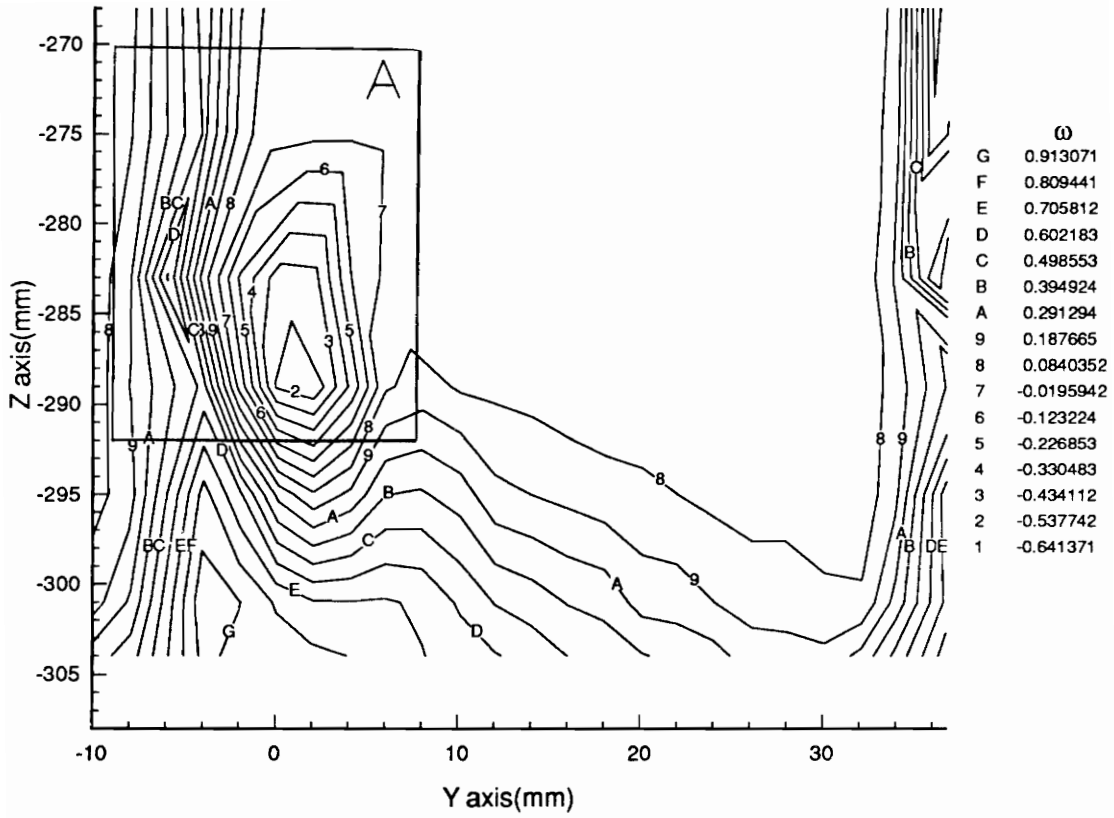

Figure 61. Close Up View of the Blade Passage, Corner Region Loss Contours of Fig. 60, $\alpha^* = 21$, Qsb = 26 Li/min, $V_t = 47.53$ m/s, $Re_c = 172{,}223$

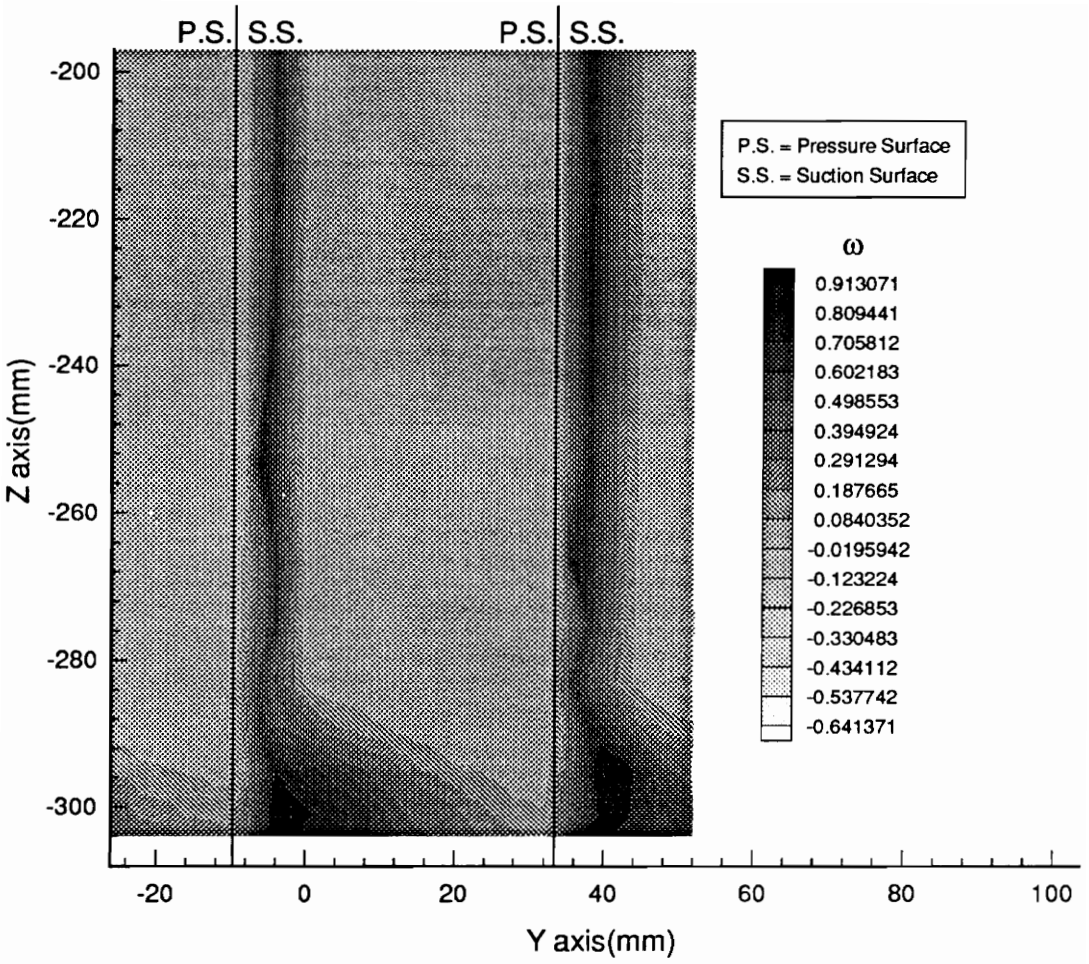

Figure 62. Downstream Loss Contours for Corner Boundary Layer Blowing with Blade Slot Number One (with external flap),
α^* = 21, Qsb = 21 Li/min, V_1 = 47.69 m/s, Re_c = 171,784

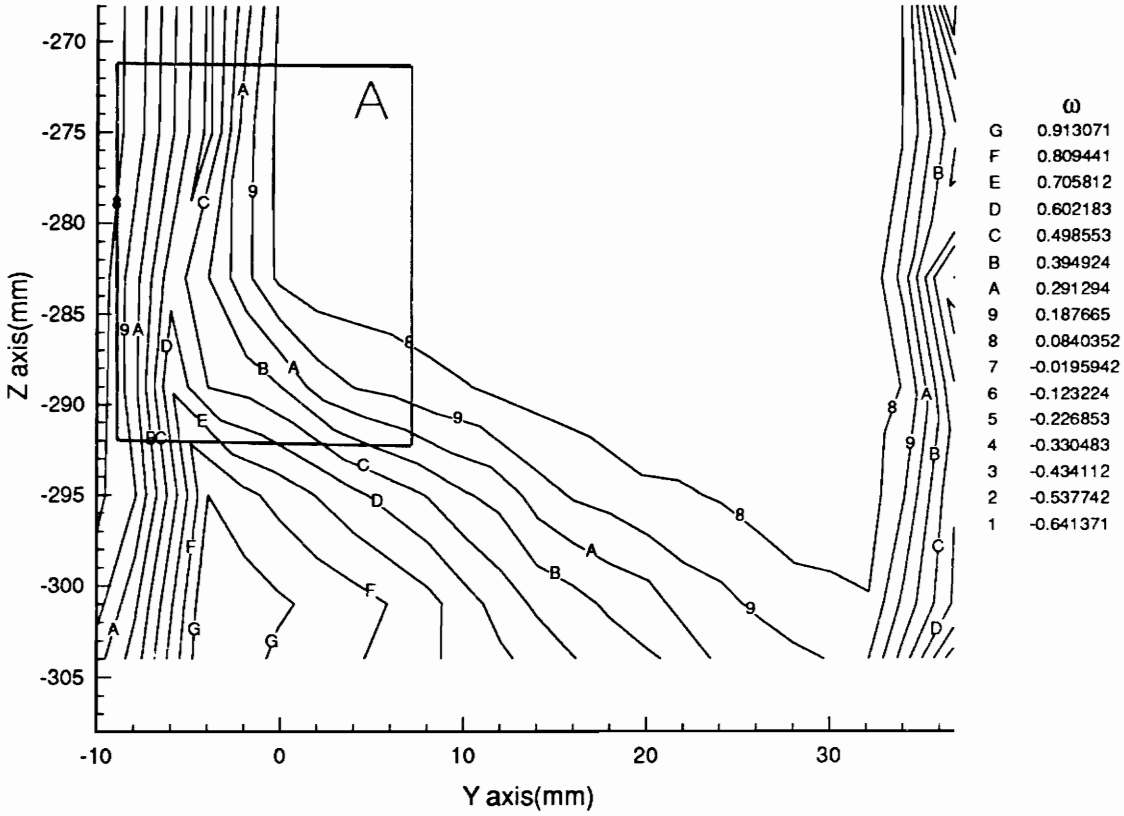

Figure 63. Close Up View of the Blade Passage, Corner Region Loss Contours of Fig. 62, $\alpha^* = 21$, Qsb = 21 Li/min, $V_1 = 47.69$ m/s, $Re_c = 171{,}784$

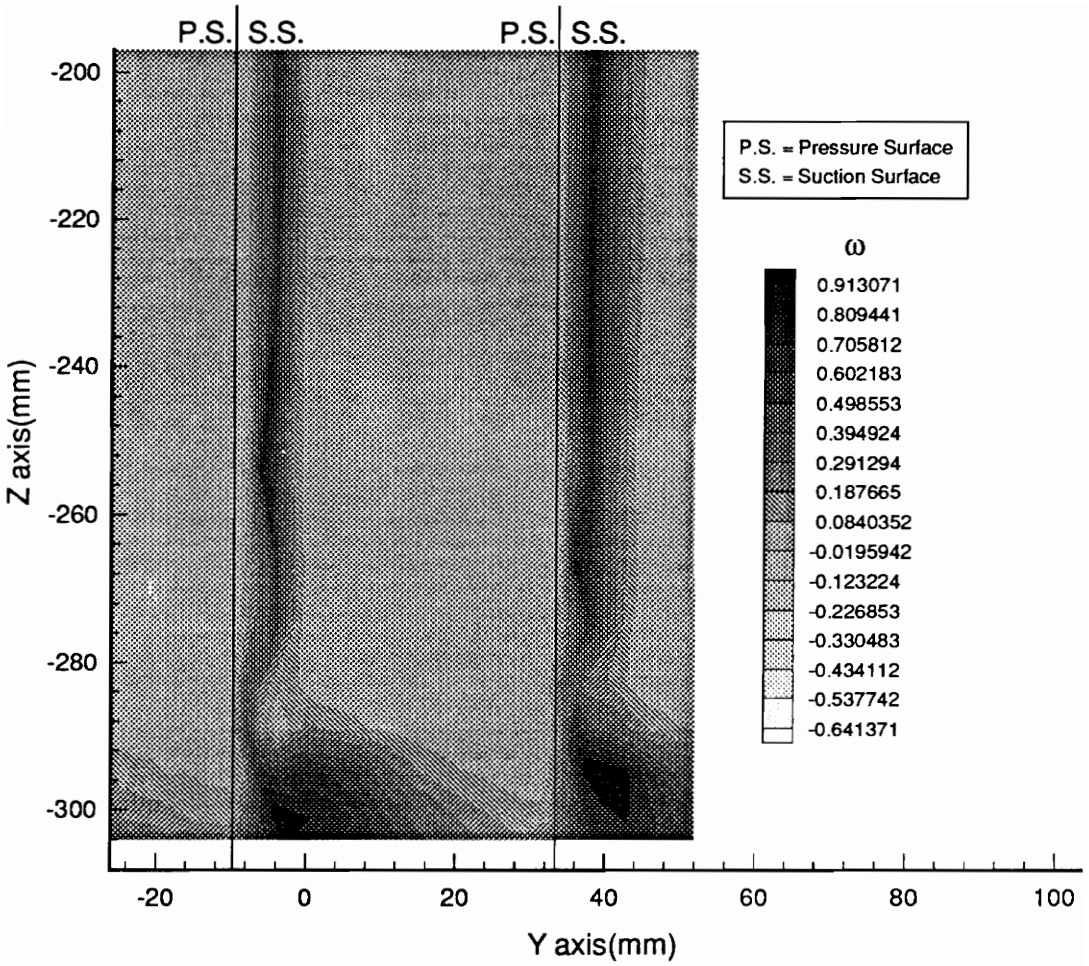

Figure 64. Downstream Loss Contours for Corner Boundary Layer Blowing with Blade Slot Number One (with external flap),
$\alpha^* = 21$, Qsb = 26 Li/min, $V_1 = 47.69$ m/s, $Re_c = 171{,}861$

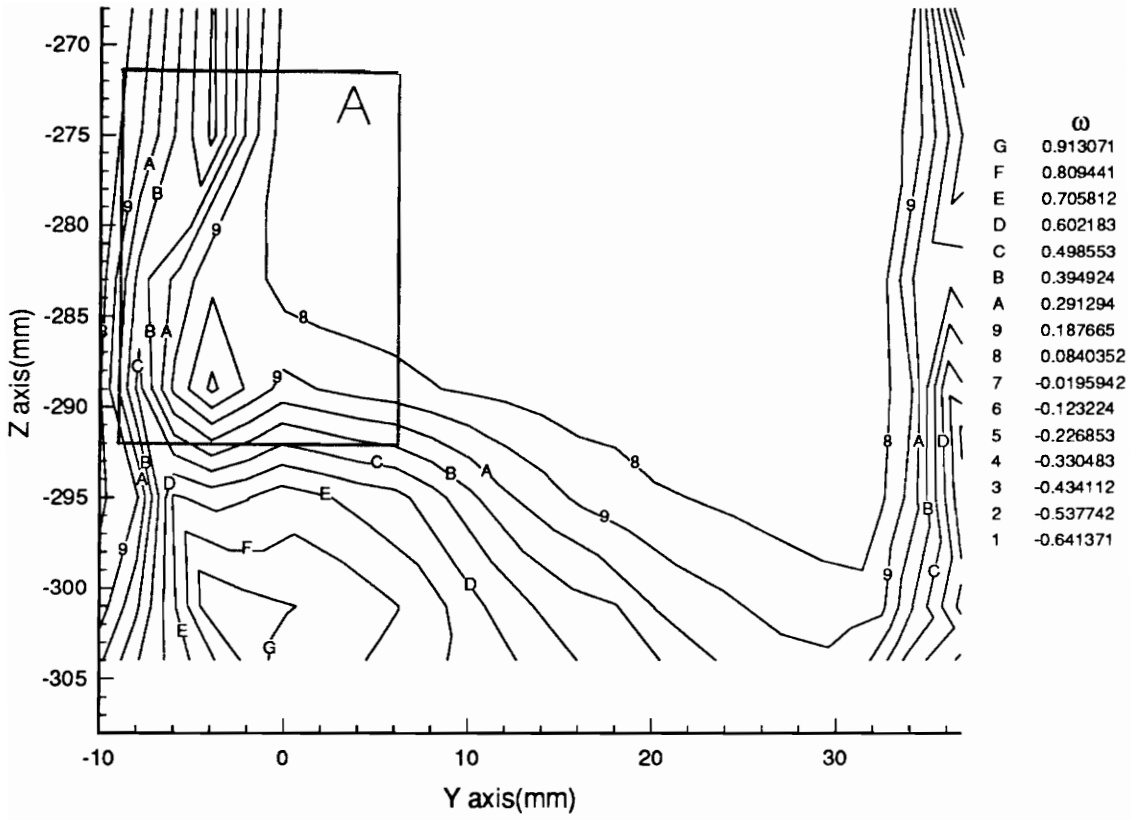

Figure 65. Close Up View of the Blade Passage, Corner Region Loss Contours of Fig. 64, $\alpha^* = 21$, Qsb = 26 Li/min, $V_1 = 47.69$ m/s, $Re_c = 171{,}861$

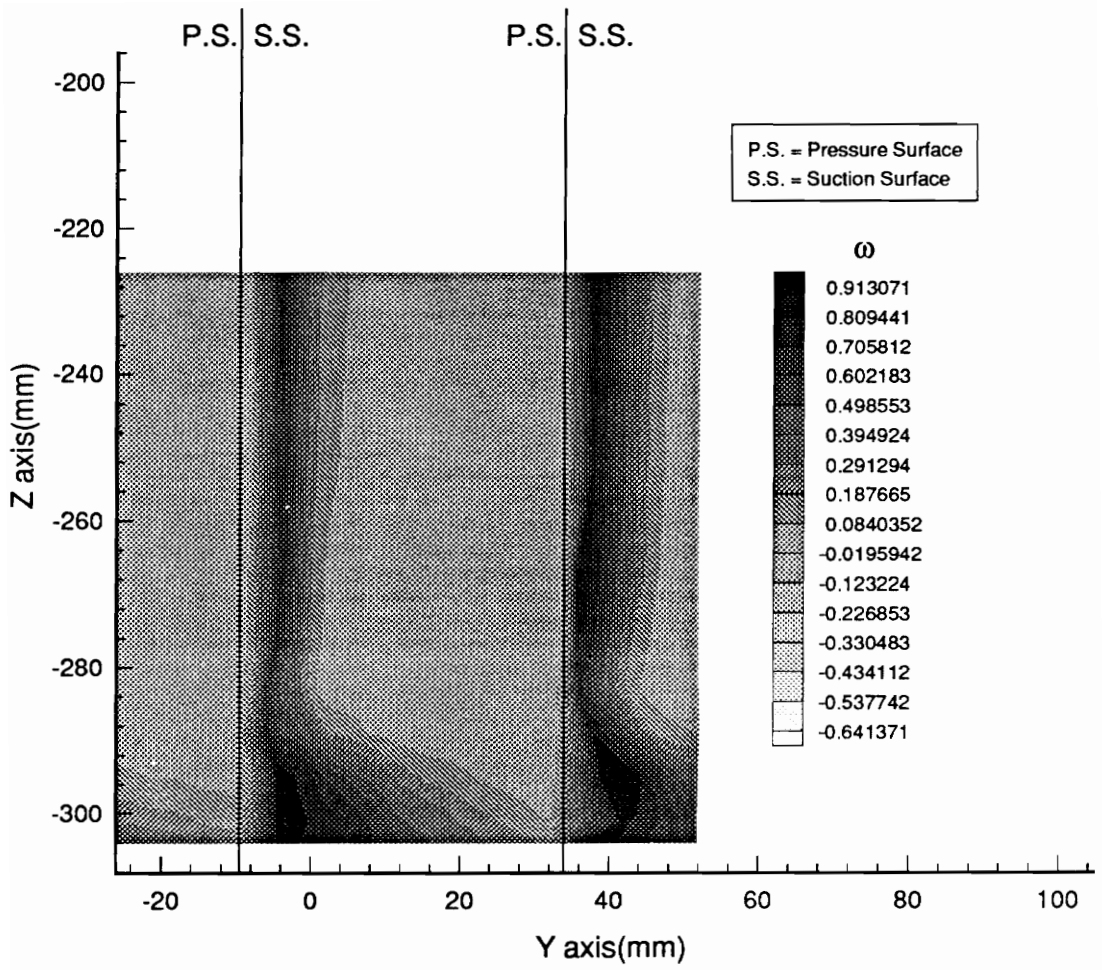

Figure 66. Downstream Loss Contours for Corner Boundary Layer Blowing with Blade Slot Number One (with external flap),
$\alpha^* = 23$, Qsb = 21 Li/min, $V_1 = 47.62$ m/s, $Re_c = 171{,}523$

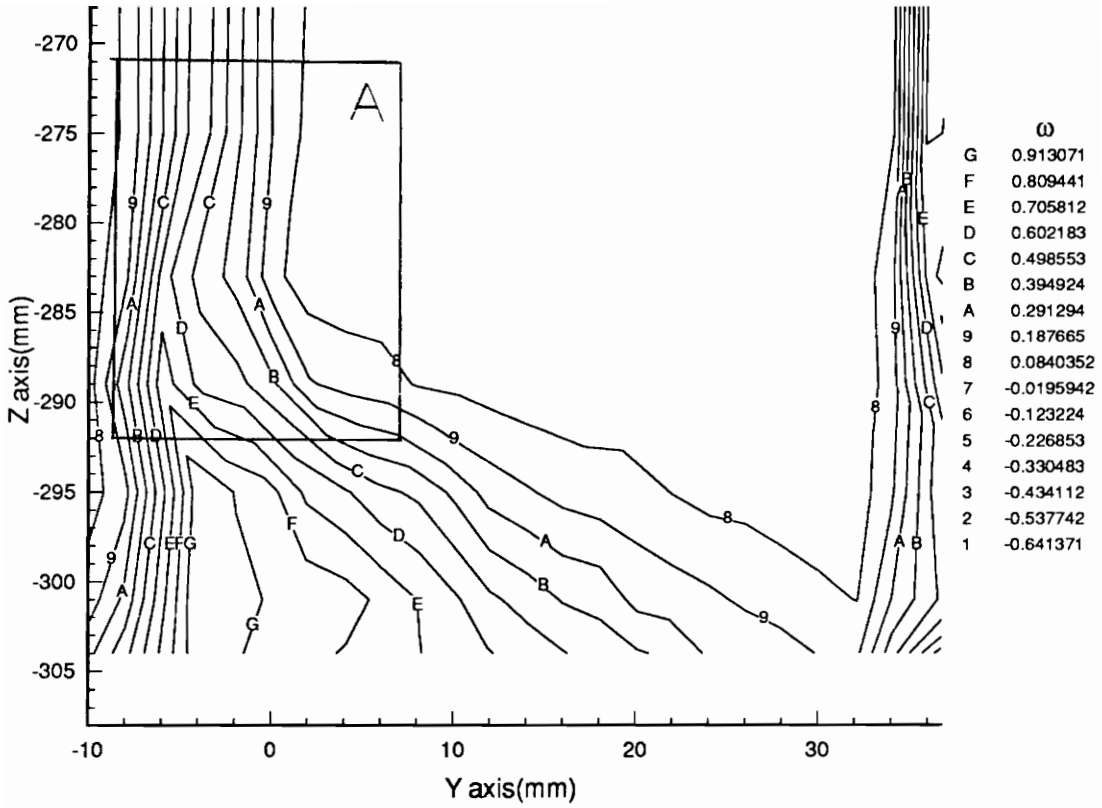

Figure 67. Close Up View of the Blade Passage, Corner Region Loss Contours of Fig. 66, $\alpha^* = 23$, Qsb = 21 Li/min, $V_t = 47.62$ m/s, $Re_c = 171{,}523$

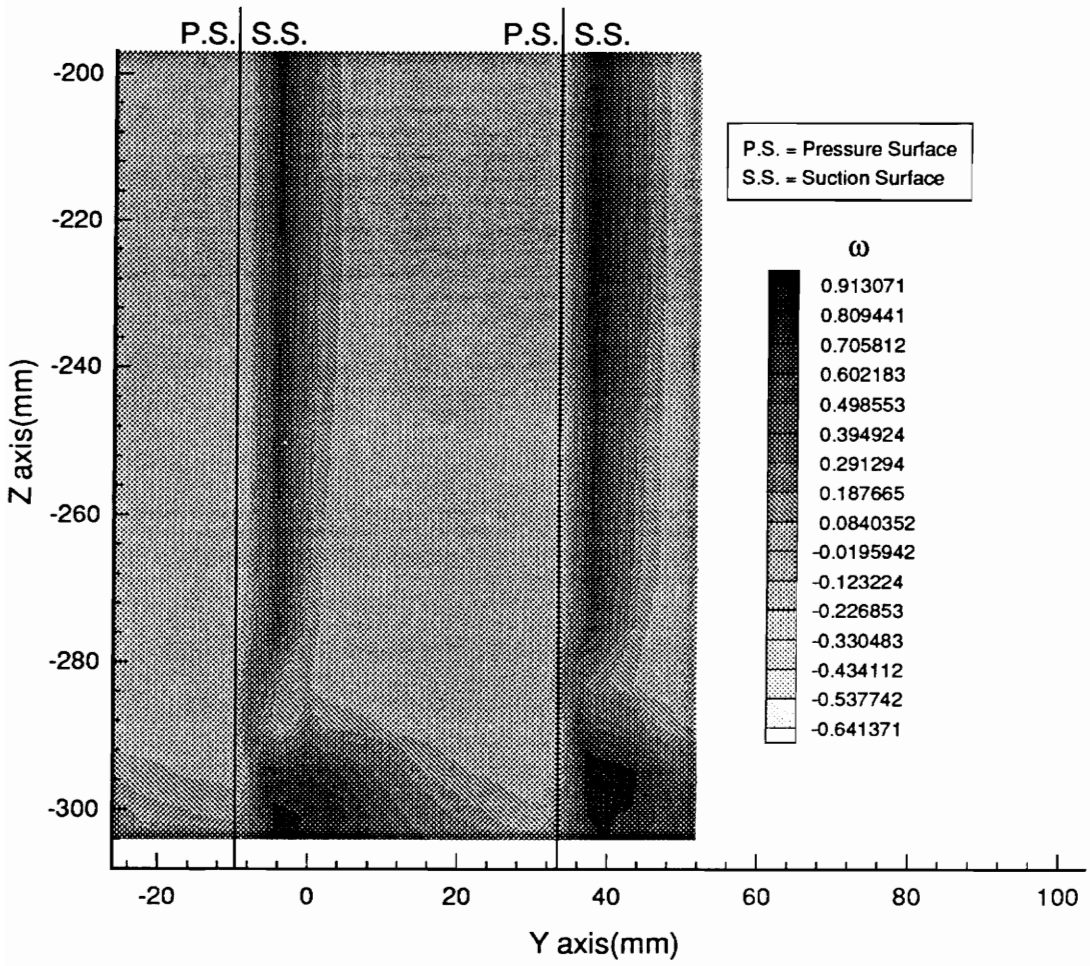

Figure 68. Downstream Loss Contours for Corner Boundary Layer Blowing with Blade Slot Number One (with external flap),
$\alpha^* = 23$, Qsb = 26 Li/min, $V_1 = 47.55$ m/s, $Re_c = 171{,}823$

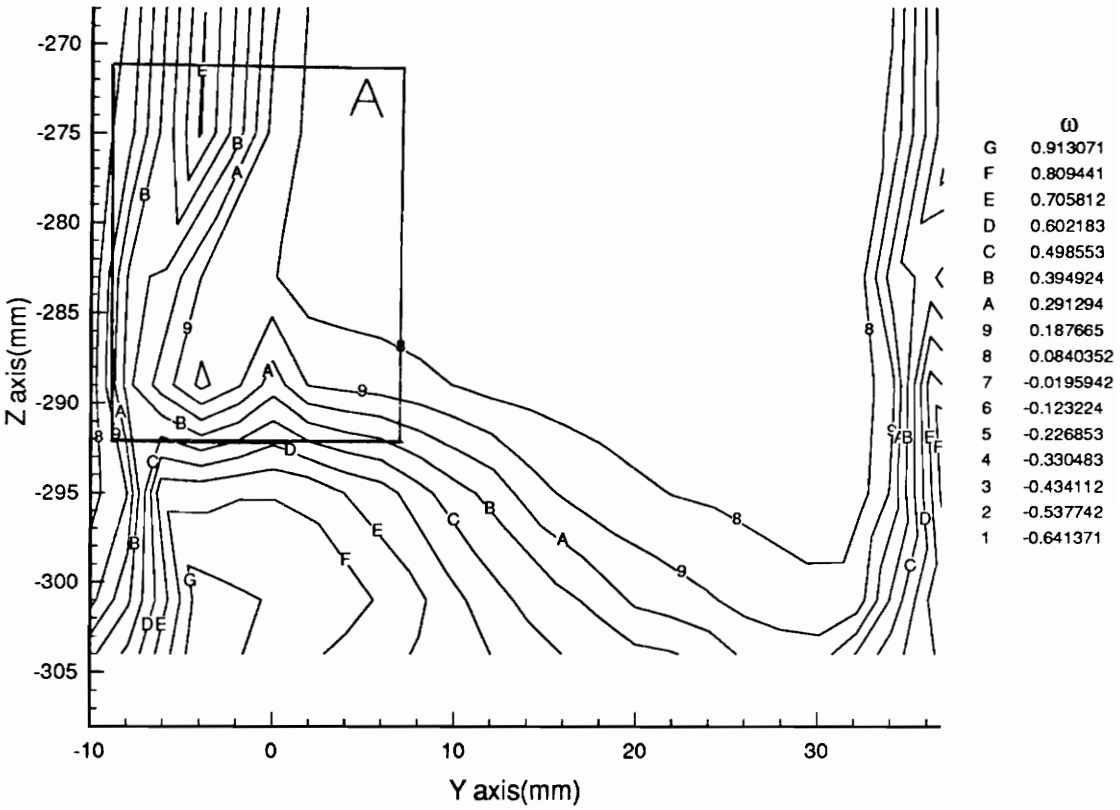

Figure 69. Close Up View of the Blade Passage, Corner Region Loss Contours of Fig. 68, $\alpha^* = 23$, Qsb = 26 Li/min, $V_1 = 47.55$ m/s, $Re_c = 171{,}823$

degrees AoA, at a Qsb setting of 21 Li/min the values of ω in region A reach a minimum of ω = -0.226, which corresponds to a contour level of 5 (Fig. 55). At the same AoA, when Qsb is increased to 26 Li/min, a minimum contour level of 2 was reached, with subsequent decreases in ω occurring in the areas adjacent to region A (Fig. 57). The higher momentum fluid in region A appears to decrease the losses for the portion of the corner flow which encloses the higher loss fluid located closest to the cascade sidewall (z = -308mm). As shown in Figures 59 and 61, at 21 degrees AoA, when Qsb was increased from 21 to 26 Li/min, the core of the low loss area in region A grew to encompass more of the area previously occupied by the corner stall.

3.3.2.2 Blade Slot One With External Flap

The loss contour plots in Figures 62 through 69 indicate that the most significant decrease in the value of ω occurs in a much smaller downstream area of the blade wake than for the results shown in section 3.3.2.1. In comparison to the loss contour plots for corner boundary layer blowing without the external blade slot flap, the corner stall area appears larger. Additionally, negative loss coefficient values do not appear in region A, and the area of significant loss reduction, in addition to being somewhat smaller, also appears to affect a region closer to the proximity of the blade trailing edge. As shown in Fig. 65, at 21 degrees AoA, for a Qsb setting of 26 Li/min, the core of the reduced losses in region A centers around y = -4mm. From looking at the loss contours

in Fig. 61, which corresponds to boundary layer blowing without the blade slot flap in place, the core of the low loss area in region A centers around y = 1mm, a position which is farther away from the blade trailing edge. The loss contours shown in Fig. 69, which correspond to a Qsb setting of 26 Li/min at 23 degrees AoA, also show the core of the decreased loss coefficient values in region A to center around y = -4mm.

3.3.3 Percent Change in Overall Mass - Averaged Loss Coefficient Values

A series of overall mass - averaged loss coefficient results for corner boundary layer blowing are presented in Table 4. The results are representative of corner boundary layer blowing experiments performed at 19 and 21 degrees AoA, utilizing blade slot one. The results show the relative changes in the value of ϖ_2 calculated for the two blade slot configurations. With the external blade slot flap in place, a 5.2% decrease in ϖ_2 was calculated for 19 degrees AoA, at a Qsb setting of 21.45 Li/min. From the calculations for boundary layer blowing without the external blade slot flap in place, at the same AoA and Qsb combination a 29.8% decrease in the value of ϖ_2 resulted. At 19 and 21 degrees AoA, at the larger Qsb setting, reductions of 33.0% and 31.9%, respectively, were calculated for corner boundary layer blowing without the external blade slot flap in place.

It should be noted that the reductions in the overall mass - averaged loss coefficient values presented in Table 4 were calculated without taking into

account the amount of energy required to generate the blade slot jet air flow. With the inclusion of this additional system loss, the net reduction in the value of ϖ_2 would be less.

Table 4. Slotted Blade Overall Mass - Averaged Loss Coefficient Results

α^*	Qsb (Li/min)	ϖ_2 (based on Table 2 experiments performed)	% change in ϖ_2
19	0	.06115	---
21	0	.06892	---

a) slotted blades with external flap

Slot #1			
19	9.33	.05996	-2.0%
19	21.45	.05800	-5.2%
21	26.63	.06568	-4.7%

b) slotted blades without external flap

Slot #1			
19	21.36	.04295	-29.8%
19	26.83	.04095	-33.0%
21	21.35	.05757	-16.5%
21	26.92	.04688	-31.9%

4.0 Conclusions

Corner region blade tap pressure measurements and five - hole pitot probe measurements were taken in the wake of the central passage of a linear compressor cascade wind tunnel in order to gain a better understanding of corner flow behavior. Using the results of these initial measurements, a set of slotted cascade blades were designed and corner region boundary layer blowing experiments were done for 19, 21, and 23 degrees angle of attack.

From the initial set of downstream measurements, the corner flow appears as an area of high loss fluid, composed of one or more vortex structures that appear to have a significant role in the migration of stalled fluid into adjacent blade passage areas. The results also indicated that the initiation of corner stall began at angles of attack beyond 15 degrees, with the corner flow remaining as a large area of high loss fluid for all subsequent angles of attack. Additionally, the corner region pressure tap measurements revealed that the corner flow was able to avoid fully separating from the blade suction surface at higher angles of attack than the flow over the rest of the blade span could withstand before the

onset of full blade stall. Corner region boundary layer blowing was able to produce significant reductions in cascade total pressure losses, as illustrated by the mass - averaged loss coefficient results and the loss contour plots for boundary layer blowing. The amount of energy required to generate the blade slot jet air flow was not taken into account as a loss in the presentation of these results. If it were, less of a reduction in the cascade total pressure losses would have been the result.

In the region closest to the cascade sidewall, the pitchwise mass - averaged loss coefficient results revealed that corner region boundary layer blowing was not able to reduce the major extent of the corner stall in this area. Instead, corner boundary layer blowing was shown to have its greatest effect in the region between the exterior portion of the cascade corner flow and the beginning portion of the blade profile boundary layer flow. In this transitional region, without the use of a blade slot flap to constrain the path of the jet air being injected into the main passage flow, a significant reduction in total pressure loss values occurred. With the blade slot flap in place, a smaller reduction in the cascade total pressure loss values occurred. However, the area of blade slot jet air effectiveness moved closer to the blade suction surface. The difference in the chordwise location of the blade slots appeared to have little effect on the measured results. Corner boundary layer blowing had no apparent effect outside of the transitional region of fluid flow which exists between the

corner region boundary layer flow and the essentially two - dimensional blade profile boundary layer flow, which exists over the rest of the blade suction surface outside of the corner region.

5.0 Recommendations

A number of suggestions for further study of the corner region are:

1) Sidewall boundary layer blowing or suction in the cascade corner region.

2) A complete surface pressure analysis of the corner region passage area using static pressure taps.

3) Numerical predictions of the corner boundary layer flow behavior in order to design a more effective corner boundary layer manipulation scheme.

References

1. Schlichting, H., *Boundary - Layer Theory*, McGraw - Hill, 7th ed., New York, 1979.

2. Maestrello, L., "Active Transition Fixing and Control of the Boundary Layer in Air," AIAA Paper No. 85 - 564, 1985.

3. Gallus, H. E., Hoenen, H., "Experimental Investigations of Airfoil - and Endwall Boundary Layers in a Subsonic Compressor Stage," ASME Paper No. 86-GT-143, 1986.

4. Mikolajczak, A. A., Weingold, H. D., Nikkanen, J. P., "Flow Through Cascades of Slotted Compressor Blades," ASME *Journal of Engineering for Power*, Vol. 92, Jan. 1970, pp. 57-64.

5. Erwin, J. R., Emery, J. C., "Effect of Tunnel Configuration and Testing Technique on Cascade Performance," NACA Report 1016, 1951.

6. Dirlik, S. P., Kimmel, K. R., Sekelsky, A., Slomski, J. F., "Experimental Evaluation of a 50 - Percent Thick Airfoil with Blowing and Suction Boundary Layer Control," AIAA Paper No. 92-4500-CP, 1992.

7. Tang, Y. P., Chen, F., Chen, M. Z., "Experimental Investigation of Vortex Structure in Corner Region of a Linear Compressor Cascade," ASME Paper No. 91-GT-158, 1991.

8. Russ, T. W., "A Surface Flow Visualization Study of Boundary Layer Behavior on the Blades of a Solid-Wall Compressor Cascade at High Angles of Attack," M. S. Thesis, Mechanical Engineering, VPI & SU, 1987.

9. Gostelow, J. P., *Cascade Aerodynamics*, Pergamon Press, 1st ed., New York, 1984, pp. 48-50.

10. Horlock, J. H., Louis, J. F., Percival, P. M. E., and Lakshminarayana, B., "Wall Stall in Compressor Cascades," ASME Journal of Basic Engineering, Vol. 88, Sept. 1966, pp. 637-648.

11. Yocum, A. M., "An Experimental and Numerical Investigation of the Performance of Compressor Cascades with Stalled Flow," Ph. D. Dissertation, Mechanical Engineering, VPI & SU, 1988.

12. Treaster, A. L., Yocum, A. M., "The Calibration and Application of Five - Hole Probes," ISA Transactions, 979, Vol. 18, No. 3, pp. 23-34

13. Drost, U., "An Experimental Investigation of the Corner Stall Behavior of a Linear Compressor Cascade at High Angles of Attack," Diploma Project, submitted to the Dept. of Mech. Eng. of the Swiss Federal Institute of Technology - Lausanne, 1994.

14. Kline, S. J., and McClintock, F. A., "Describing Uncertainties in Single - Sample Experiments, " *Mechanical Engineering*, p. 3, January, 1953.

15. Catalog, *The flow and Level Handbook*, Vol. 28, © Copyright 1992, Omega Engineering, INC.

Appendix A. Blade Slot Jet Air Velocity Calculation Procedure

The velocity of the air emerging from the blade slots was calculated by using the conservation of mass equation, the ideal gas equation, and the rotameter volumetric flow rate setting, Qsr. The relevant equations are as follows:

To find the actual rotameter volumetric flow rate, Qsa, at the cascade operating conditions, the following equation was used [15]:

$$Qsa = \frac{14.7 \cdot Qsr \cdot (Tamb + 460)}{530 \cdot Pamb}$$

where Qsr was the volumetric flow rate read directly from the rotameter. Thus, Qsa is the volumetric flow rate of air injected within the cascade passage, from the blade slots, *at the cascade flow conditions.*

From this the jet velocity, V_j, was calculated using the following relation:

$$V_j = \frac{\rho_a \cdot Qsa}{8 \cdot \rho_j \cdot A_j}$$

where A_j = 1.2 x10^{-6} m^2 and ρ_a was assumed equal to ρ_j (i.e. the jet exit pressure and temperature were assumed equal to the ambient pressure and temperature). Each jet, as defined by the dimensions of the blade slot turning vanes, was 1/4 of the volumetric flow rate of air supplied by each blade slot. V_j was uniform at all locations along the length of the blade slot.

Appendix B. Five - Hole Prism Probe Calibration and Data Evaluation Procedure

The five - hole prism probe was calibrated by mounting it in a uniform flow stream and recording a series of pressure measurements from the probe as it was moved through a series of yaw and pitch angle combinations. A rectangular duct was used as the calibration section, and it was attached to the wind tunnel to provide a uniform flow stream. The duct was equipped with a mechanism which allowed the probe yaw and pitch angle, relative to the incoming flow stream, to be varied. The upstream total pressure was obtained from the tunnel settling chamber, and the upstream static pressure of the inlet flow was measured by two pressure taps located on the top and bottom walls of the calibration section. From the upstream total pressure and the average of the two static pressure measurements, the velocity of the air flow in the calibration section was found using Bernoulli's equation.

The calibration procedure proposed by Treaster, et al. [12] was used to calibrate the five - hole prism probe. During the experiments, the probe was used in a non - nulling mode. This meant that the relationships between the measured five - hole pressures and the true local static pressures, total pressure, flow angles, and velocities, relative to the probe, had to be determined. The pressures from the five - hole probe were expressed as a set of dimensionless pressure coefficients. The pressure coefficients are functions of the flow angularity and are presented here:

$$Cp_{yaw} = \frac{(P_2 - P_3)}{(P_1 - \overline{P})}$$

$$Cp_{pitch} = \frac{(P_4 - P_5)}{(P_1 - \overline{P})}$$

$$Cp_{total} = \frac{(P_1 - P_{total})}{(P_1 - \overline{P})} \qquad \text{(B.1)}$$

$$Cp_{static} = \frac{(\overline{P} - P_{static})}{(P_1 - \overline{P})}$$

$$\overline{P} = \frac{(P_2 + P_3 + P_4 + P_5)}{4}$$

The probe pitch and yaw planes, which correspond to the cascade x - z and x - y planes, respectively, are shown in Fig. B.1. The calibration data is presented in Figures B.2a and B.2b. These figures consist of plots showing Cp_{yaw} versus Cp_{pitch}, Cp_{static} versus pitch angle at constant yaw angles, and Cp_{total} versus pitch angle at constant yaw angles.

For the measured values of Cp_{yaw} and Cp_{pitch}, a double interpolation procedure was done using the Cp_{yaw} versus Cp_{pitch} calibration grid to obtain the yaw and pitch angles of the flow relative to the probe head. The yaw and pitch angles were then used to interpolate values for Cp_{static} and Cp_{total} . This permitted the evaluation of the local total pressure and static pressures using the following equations:

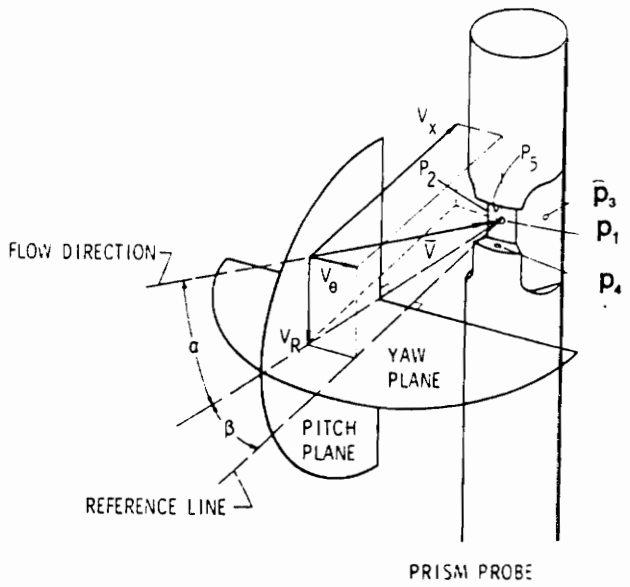

Figure B.1. Geometry of the Five - Hole Prism Probe [12]

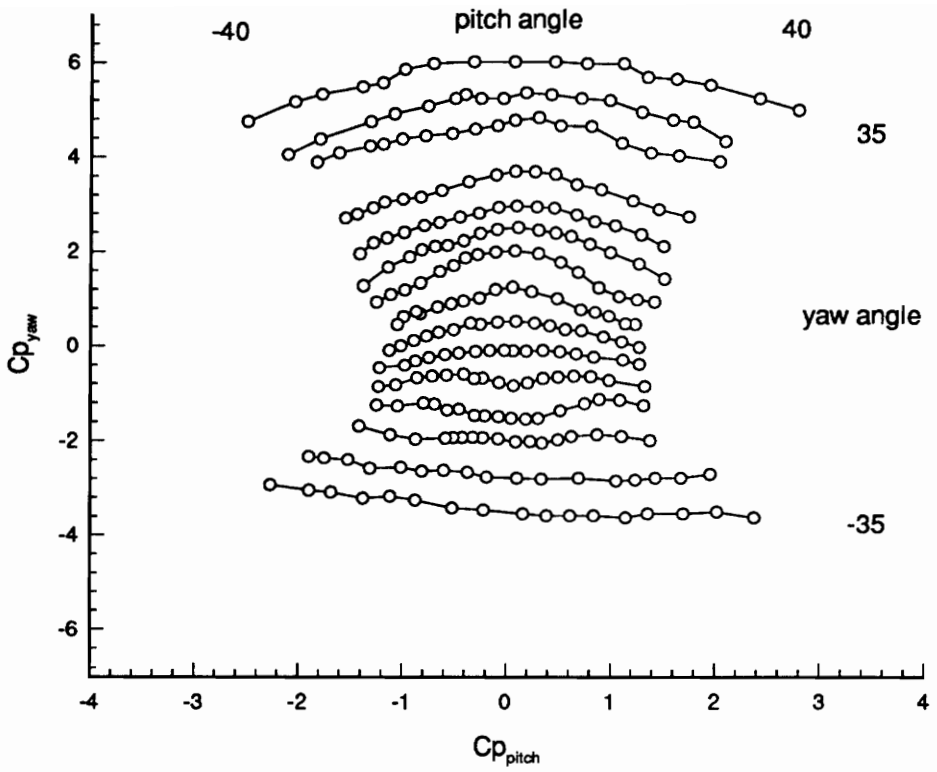

Figure B.2a. Five - Hole Prism Probe Calibration Data

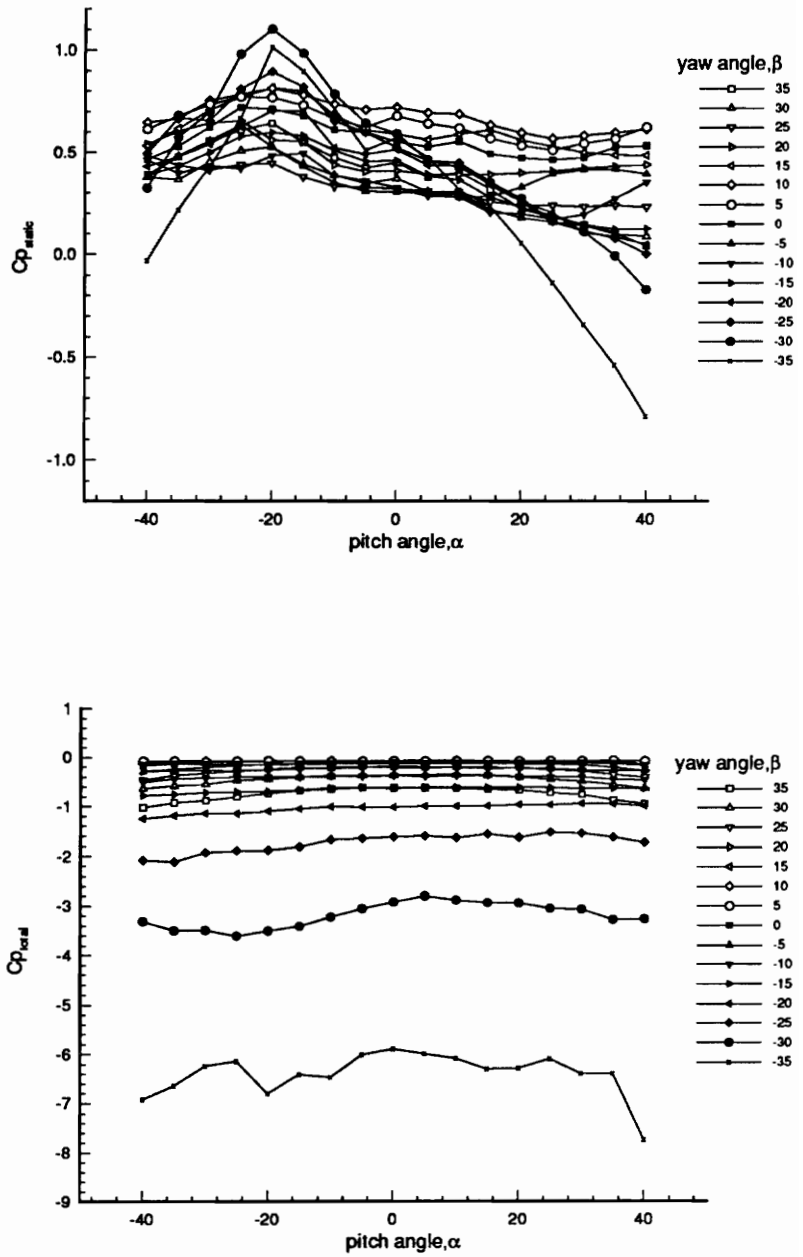

Figure B.2b. Five - Hole Prism Probe Calibration Data

$$P_{total} = P_{ref} + \Delta P_1 - Cp_{total}(\Delta P_1 - \Delta\overline{P})$$
$$P_{static} = P_{ref} + \Delta\overline{P} - Cp_{static}(\Delta P_1 - \Delta\overline{P}) \qquad \text{(B.2)}$$

The reference pressure is the ambient pressure, and the Δ symbol serves as an indication that all of the measured pressures were taken relative to the ambient pressure. From these results, the velocity of the flow, relative to the probe head, was calculated from Bernoulli's equation:

$$V = \sqrt{\tfrac{2}{\rho}(P_{total} - P_{static})} \qquad \text{(B.3)}$$

which, by using equations B.2, reduces to equation B.4:

$$V = \sqrt{\tfrac{2}{\rho}(P_1 - \overline{P})(1 + Cp_{static} - Cp_{total})} \qquad \text{(B.4)}$$

The velocity components were then calculated using the trigonometric relationships shown in Fig. B.1:

$$V_x = V(\cos\beta)(\cos\alpha)$$
$$V_y = V(\sin\beta) \qquad \text{(B.5)}$$
$$V_z = V(\cos\beta)(\sin\alpha)$$

All of the above steps were implemented with a series of BASIC computer programs developed by Drost [13]. A computer program (EX1CAL1.BAS) was used to obtain the five - hole pressures. The yaw angle range went from -35 degrees to 35 degrees, and the pitch angle range went from -40 degrees to 40 degrees. Each of the pressures were taken four times and averaged to obtain the final measurement. Following this, the program POST.BAS read the calibration data and generated values for $Cp_{yaw,}$ $Cp_{pitch,}$ $Cp_{static,}$ and C_{ptotal} at each of

the measured points. The number of different yaw and pitch angles (Noy and Nop) in the data set is determined, and the Cp values are arranged, along with the corresponding yaw and pitch angles, into a matrix of dimensions (Noy x Nop). The result is a grid containing rows of constant yaw angles and columns of constant pitch angles, which is stored to a file.

The program SPFIX.BAS is the program which places third order spline curves through the calibration grid's Cp values. It then deduces flow angles and velocities from the measured experimental data. The spline curves are fitted through Cp_{yaw} versus Cp_{pitch} for constant yaw angles, Cp_{pitch} versus Cp_{yaw} for constant pitch angles, and Cp_{total} and Cp_{static} versus pitch angle for constant yaw angles. After the calibration data is read, and the necessary Cp spline curves created, the values for Cp_{yaw}, Cp_{pitch}, and average pressure values are found from the experimental data. At each value of Cp_{pitch}, corresponding values of Cp_{yaw} are interpolated from the spline curves. This yields the variation of the yaw angle versus Cp_{yaw}. The resulting increasing function, when evaluated at Cp_{yaw}, is used to obtain the experimental local flow yaw angle. For this step, spline curve fitting for the yaw angle versus Cp_{yaw} is used. The same method is used to find the experimental pitch angle by interchanging the dependent and independent variables. The corresponding Cp_{static} values are found through interpolation of the spline curves of Cp_{static} versus pitch angle and the experimental pitch angle which has just been found. This gives the variation of Cp_{static} versus yaw angle. The

experimental Cp_{static} value is deduced by fitting a spline curve through the Cp_{static} versus yaw angle values and evaluating for the experimental yaw angle. The same procedure is applied for obtaining the experimental Cp_{total} value, by interchanging Cp_{static} in the aforementioned steps. Once the experimental Cp_{static} and Cp_{total} values are known, the magnitude of the velocity relative to the probe can be calculated.

From the work of Drost [13], who used the same type of probe employed for the current corner flow investigations, Reynolds number effects, based on the probe head diameter, where found to have a negligible influence on its measured pressure coefficient values. However, the probe proximity to a vertical wall had a somewhat more measurable effect on the pressure coefficient values derived from the probe pressure measurements. From his wall proximity analysis, he calculated an error of 3% for the measured total pressure and 7.2% for the measured static pressure, based on dynamic head. The percentage error calculated for the measured values was considered small enough that a method for taking into account the wall effects in the probe calibration procedure would not have been justified due to the added complexity it would have entailed.

Appendix C. Five - Hole Prism Probe Measurement Uncertainty Analysis

The uncertainty calculations of the probe measurements were done using the method of Kline, et al. [14]. In this method, the square root of the sum of the squares of the error contributions to the measured quantity are used in the determination of the uncertainty of the experimental value. The final results are then rounded to two significant figures and set off by parenthesis. Many significant figures are carried throughout the calculations in order to avoid roundoff errors. The following calculations follow the analysis procedure employed by Drost [13] in his measurement uncertainty analysis.

As shown in Appendix B, the magnitude of the velocity is given by the relation

$$V = \sqrt{\tfrac{2}{\rho}(P_1 - \overline{P})(1 + Cp_{static} - Cp_{total})} \qquad \text{(C.1)}$$

Thus, the uncertainty of this calculation is given by the relation:

$$W_V = \sqrt{\left(\frac{\partial V}{\partial \rho} W_\rho\right)^2 + \left(\frac{\partial V}{\partial P_1} W_{P1}\right)^2 + \left(\frac{\partial V}{\partial \overline{P}} W_{\overline{P}}\right)^2 + \left(\frac{\partial V}{\partial Cp_{static}} W_{Cpstatic}\right)^2 + \left(\frac{\partial V}{\partial Cp_{total}} W_{Cptotal}\right)^2} \qquad \text{(C.2)}$$

The partial derivatives are approximated by perturbing the data reduction program, and using the formula:

$$\frac{\partial V}{\partial x} = \frac{V(x + \Delta x) - V(x)}{\Delta x} \qquad \text{(C.3)}$$

where V represents the dependent variable and x represents the independent variable which will be perturbed in the data reduction program. The results of the perturbations are as follows:

$$\frac{\partial V}{\partial \rho} = -10.4755 \frac{m/s}{kg/m^3}$$

$$\frac{\partial V}{\partial P_1} = .0696 \frac{m/s}{Pa}$$

$$\frac{\partial V}{\partial \overline{P}} = -.0687 \frac{m/s}{Pa}$$

$$\frac{\partial V}{\partial Cp_{static}} = 11.0653 m/s$$

$$\frac{\partial V}{\partial Cp_{total}} = -11.0653 m/s$$

To solve equation C.2, the uncertainty in the measurements of the independent variables must be obtained.

From the ideal gas equation, the density of air is given by:

$$\rho = \frac{P_{amb}}{R \cdot T_{amb}} \qquad \text{(C.4)}$$

Thus, the uncertainty of the density is the following relation:

$$W_\rho = \sqrt{\left(\frac{\partial \rho}{\partial P_{amb}} W_{Pamb}\right)^2 + \left(\frac{\partial \rho}{\partial T_{amb}} T_{amb}\right)^2} \qquad \text{(C.5)}$$

and, by partial differentiation of equation C.4 and substituting typical values for ambient pressure and temperature:

$$\frac{\partial \rho}{\partial P_{amb}} = .0000115 \frac{kg/m^3}{Pa}$$

$$\frac{\partial \rho}{\partial T_{amb}} = -.0036029 \frac{kg/m^3}{K}$$

$$W_{Pamb} = \pm .33.763\ Pa(.01 in.Hg)\ (readability\ of\ mercury\ barometer)$$

$$W_{Tamb} = \pm .56K(\pm 1^\circ F)(thermometer\ readability)$$

the value of equation C.5 is: $W_\rho = .00205 \frac{kg}{m^3}$.

An estimate of the uncertainty in the measured pressures will be obtained assuming a normal distribution around the mean value. Thus, the uncertainty can be stated as follows:

$$W = 2\sigma \qquad \text{(C.6)}$$

where

$$\sigma = \left(\frac{\sum_{i=1}^{n}\left(x_i - \bar{x}\right)^2}{n-1}\right)^{\frac{1}{2}} \qquad \text{(C.7)}$$

and

x_i = measured value

$\bar{x}$ = mean value of the measured values

n = number of samples.

Using 100 pressure samples, the uncertainty of the pressure measurements equaled:

$$W_p = W_{\bar{P}} = W_{p1} = 4.248 Pa$$

Since Cp_{total} and Cp_{static} are functions of the probe yaw angle, β, and the probe pitch angle, α, their uncertainty is given by the following relations:

$$W_{Cpstatic} = \sqrt{\left(\frac{\partial Cp_{static}}{\partial \alpha} W_\alpha\right)^2 + \left(\frac{\partial Cp_{static}}{\partial \beta} W_\beta\right)^2}$$
$$W_{Cptotal} = \sqrt{\left(\frac{\partial Cp_{total}}{\partial \alpha} W_\alpha\right)^2 + \left(\frac{\partial Cp_{total}}{\partial \beta} W_\beta\right)^2} \qquad \text{(C.8)}$$

From inspecting the calibration data, the highest values of the partial derivatives were found:

$$\frac{\partial Cp_{static}}{\partial \alpha} = -.01248 \frac{1}{degree}$$
$$\frac{\partial Cp_{total}}{\partial \beta} = .06298 \frac{1}{degree}$$
$$\frac{\partial Cp_{static}}{\partial \beta} = .00908 \frac{1}{degree}$$
$$\frac{\partial Cp_{total}}{\partial \alpha} = -.01514 \frac{1}{degree}$$

Since the probe yaw and pitch angles were based upon the results of the five measured pressures expressed in terms of Cp_{yaw} and Cp_{pitch}, the angle uncertainties are given by the following relations:

$$W_\alpha = \sqrt{\left(\frac{\partial \alpha}{\partial Cp_{yaw}} W_{Cpyaw}\right)^2 + \left(\frac{\partial \alpha}{\partial Cp_{pitch}} W_{Cppitch}\right)^2}$$
$$W_\beta = \sqrt{\left(\frac{\partial \beta}{\partial Cp_{yaw}} W_{Cpyaw}\right)^2 + \left(\frac{\partial \beta}{\partial Cp_{pitch}} W_{Cppitch}\right)^2} \qquad \text{(C.9)}$$

The partial derivatives in equation C.9 were also found from an inspection of the calibration data:

$$\frac{\partial \alpha}{\partial Cp_{yaw}} = 2.2035 \, degree$$
$$\frac{\partial \alpha}{\partial Cp_{pitch}} = 32.5733 \, degree$$
$$\frac{\partial \beta}{\partial Cp_{yaw}} = 9.1642 \, degree$$
$$\frac{\partial \beta}{\partial Cp_{pitch}} = 3.4507 \, degree$$

The definition of the yaw and pitch pressure coefficients, based on the average of the five measured pressures, are:

$$Cp_{yaw} = \frac{(P_2 - P_3)}{(P_1 - \overline{P})}$$
$$Cp_{pitch} = \frac{(P_4 - P_5)}{(P_1 - \overline{P})} \qquad \text{(C.10)}$$
$$\overline{P} = \frac{(P_2 + P_3 + P_4 + P_5)}{4}$$

The uncertainty of the average pressures is the same as the uncertainty in each of the measured pressures, thus: $W_p = W_{P1,P2,P3,P4,P5} = W_{\overline{P}}$

and the uncertainty in the pressure coefficients is given by the following relations:

$$W_{Cpyaw} = \sqrt{\left(\frac{\partial Cp_{yaw}}{\partial P_2} W_p\right)^2 + \left(\frac{\partial Cp_{yaw}}{\partial P_3} W_P\right)^2 + \left(\frac{\partial Cp_{yaw}}{\partial P_1} W_P\right)^2 + \left(\frac{\partial Cp_{yaw}}{\partial \overline{P}} W_{\overline{P}}\right)^2}$$

$$W_{Cppitch} = \sqrt{\left(\frac{\partial Cp_{pitch}}{\partial P_4} W_P\right)^2 + \left(\frac{\partial Cp_{pitch}}{\partial P_5} W_P\right)^2 + \left(\frac{\partial Cp_{pitch}}{\partial P_1} W_P\right)^2 + \left(\frac{\partial Cp_{pitch}}{\partial \overline{P}} W_P\right)^2} \quad \text{(C.11)}$$

The partial derivatives in equations C.11 were found by perturbing the data reduction program and the results are as follows:

$$\frac{\partial Cp_{yaw}}{\partial P_2} = .0047 \frac{1}{Pa}$$

$$\frac{\partial Cp_{yaw}}{\partial P_3} = -.0091 \frac{1}{Pa}$$

$$\frac{\partial Cp_{yaw}}{\partial P_1} = .0184 \frac{1}{Pa}$$

$$\frac{\partial Cp_{yaw}}{\partial \overline{P}} = -.0200 \frac{1}{Pa}$$

$$\frac{\partial Cp_{pitch}}{\partial P_4} = .0041 \frac{1}{Pa}$$

$$\frac{\partial Cp_{pitch}}{\partial P_5} = -.0047 \frac{1}{Pa}$$

$$\frac{\partial Cp_{pitch}}{\partial P_1} = .0014 \frac{1}{Pa}$$

$$\frac{\partial Cp_{pitch}}{\partial \overline{P}} = -.0015 \frac{1}{Pa}$$

Using equations C.11, the uncertainty in the pressure coefficient calculations can be found:

$$W_{Cpyaw} = .04498$$

$$W_{Cppitch} = .02762$$

Using these results, the uncertainty of the yaw and pitch angle measurements can be found using equations C.9:

$W_{\alpha} = 1.4685\ \text{degrees} \quad (1.47\ \text{degrees})$
$W_{\beta} = .4171\ \text{degrees} \quad (.42\ \text{degrees})$

From equations C.8:

$W_{Cpstatic} = .0187$
$W_{Cptotal} = .0344$

which, using equation C.2, yields the uncertainty in the velocity measurement made with the probe:

$W_{V} = .6014\ (m/s) \quad (.60\ m/s)$

Appendix D. Blade Pressure Surface Pressure Tap Measurements

The following Cp profiles show the cascade blade pressure surface pressure tap measurements, corresponding to the suction surface pressure distributions shown in figures 12, 13, and 14 of section 3.1, respectively.

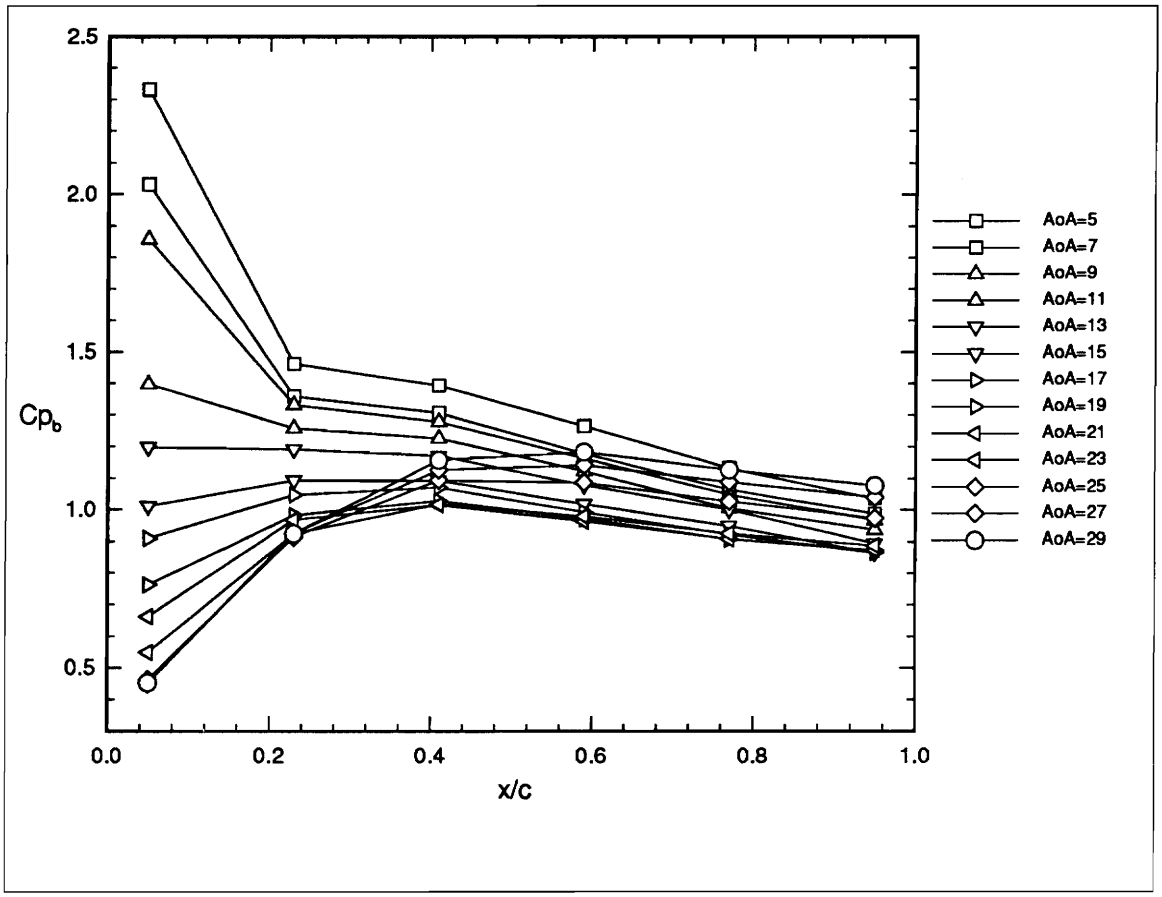

Figure D.1. Collection of Blade Pressure Surface Pressure Distributions at Midspan (z = -154mm)

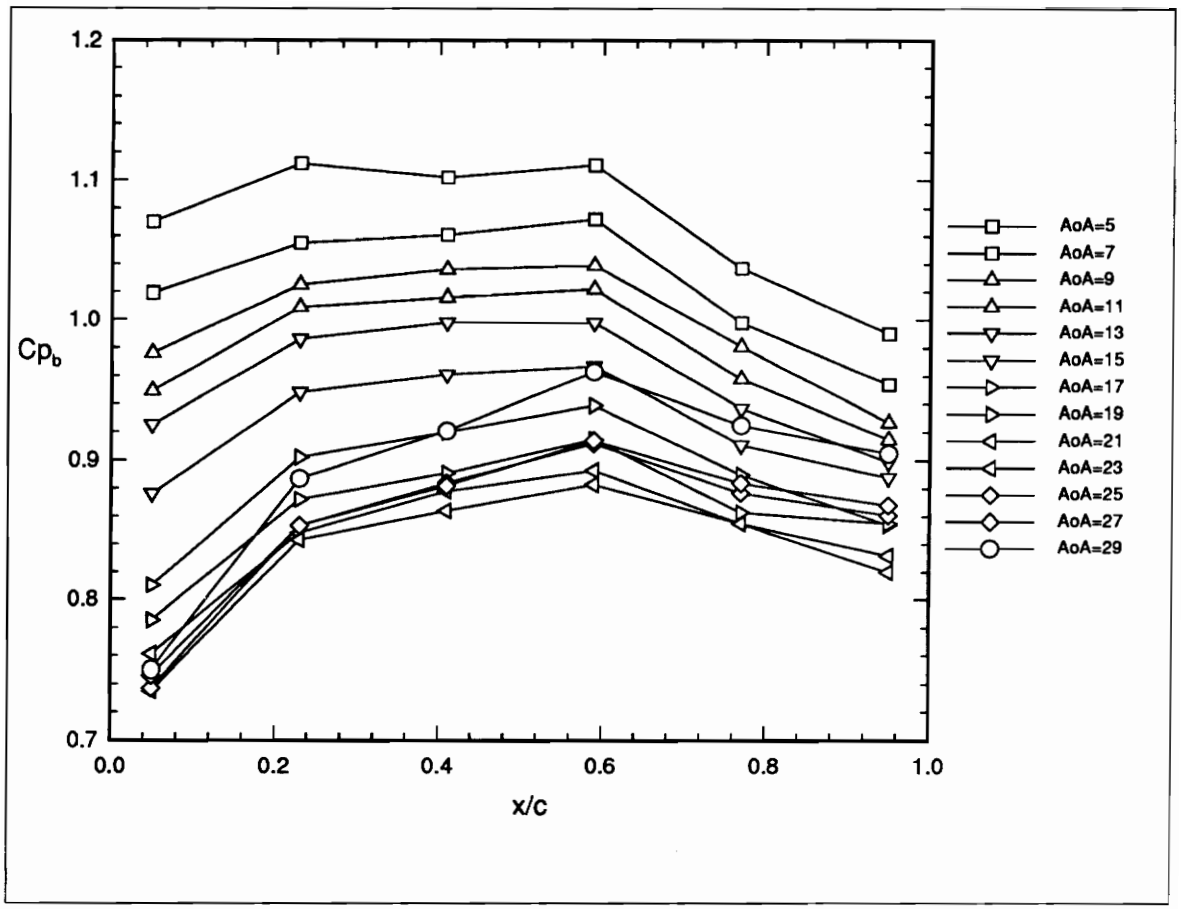

Figure D.2. Collection of Blade Pressure Surface,Corner Region Pressure Distributions (z = -302.8mm)

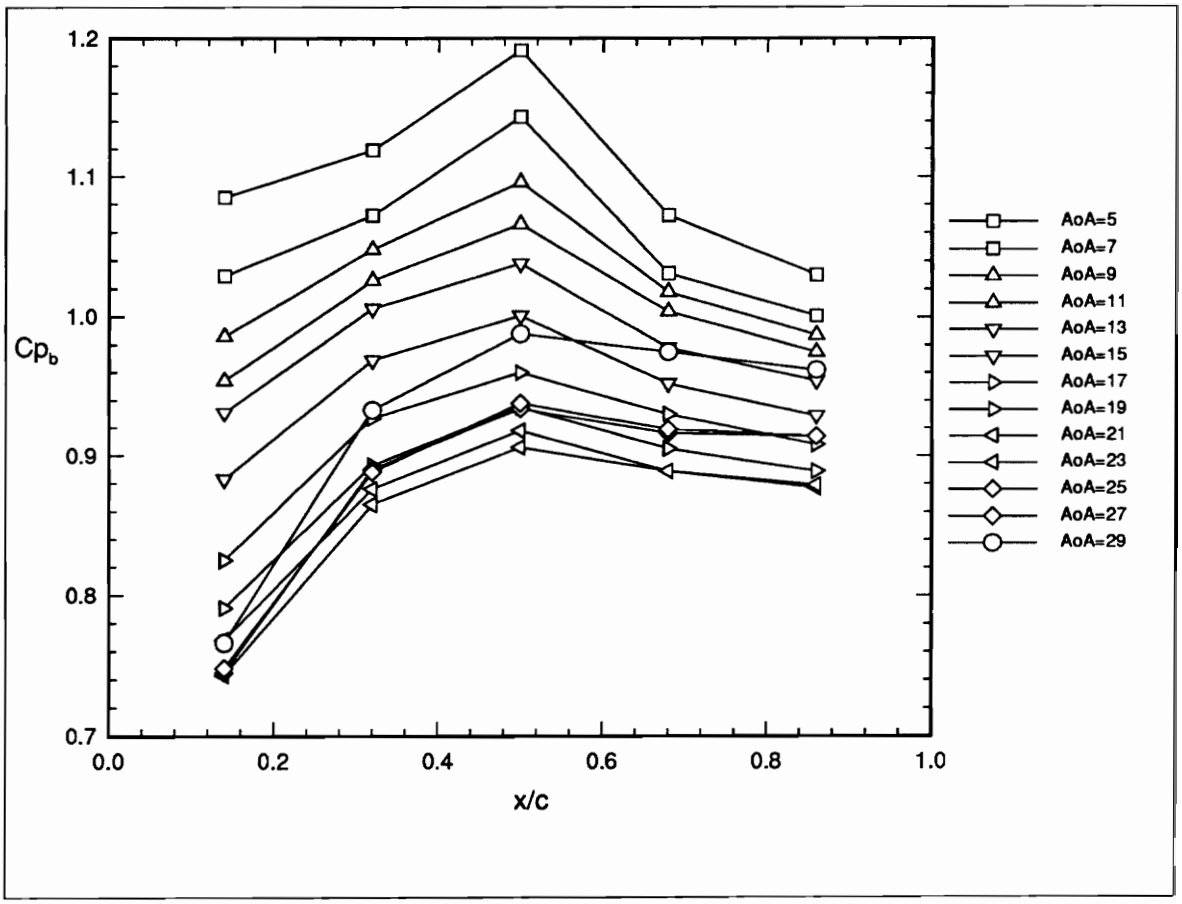

Figure D.3. Collection of Blade Pressure Surface, Corner Region Pressure Distributions (z = -292.8mm)

Vita

Ralph W. James, Jr. was born on October 6, 1970 in Miami, Florida. Throughout the early portion of his childhood, due to his father's military career as an Army officer, he lived for a time in Northern Virginia, Texas, and Japan before he and his parents settled down in Virginia Beach, Virginia. After graduating in 1989 from Green Run High School in Virginia Beach, he began his college career at Virginia Tech in the fall of that year. Upon his subsequent graduation in the spring of 1993 with a B. S. degree in Aerospace Engineering, he decided to remain at Virginia Tech in order to pursue a master's degree in Mechanical Engineering, which he finally obtained in June 1995.